



저작자표시-비영리-변경금지 2.0 대한민국

이용자는 아래의 조건을 따르는 경우에 한하여 자유롭게

- 이 저작물을 복제, 배포, 전송, 전시, 공연 및 방송할 수 있습니다.

다음과 같은 조건을 따라야 합니다:



저작자표시. 귀하는 원저작자를 표시하여야 합니다.



비영리. 귀하는 이 저작물을 영리 목적으로 이용할 수 없습니다.



변경금지. 귀하는 이 저작물을 개작, 변형 또는 가공할 수 없습니다.

- 귀하는, 이 저작물의 재이용이나 배포의 경우, 이 저작물에 적용된 이용허락조건을 명확하게 나타내어야 합니다.
- 저작권자로부터 별도의 허가를 받으면 이러한 조건들은 적용되지 않습니다.

저작권법에 따른 이용자의 권리는 위의 내용에 의하여 영향을 받지 않습니다.

이것은 [이용허락규약\(Legal Code\)](#)을 이해하기 쉽게 요약한 것입니다.

[Disclaimer](#)

공학박사 학위논문

**Mechanics-based Design and
Realization of Electrodes for
Electrochemical Energy Storages**

역학 기반 전지 전극 설계 및 실현

2017년 2월

서울대학교 대학원

기계항공공학부

임진명

역학 기반 전지 전극 설계 및 실현

Mechanics-based Design and Realization of Electrodes for Electrochemical Energy Storages

지도교수 조 맹 효

이 논문을 공학박사 학위논문으로 제출함

2016 년 10 월

서울대학교 대학원

기계항공공학부

임진명

임진명의 공학박사 학위논문을 인준함

2016 년 12 월

위원장 : 김윤영 

부위원장 : 조맹효 

위원 : 유병동 

위원 : 김호연 

위원 : 조영재 

**Mechanics-based Design and
Realization of Electrodes for
Electrochemical Energy Storages**

by

Jin-Myoung Lim

A Dissertation

Submitted to the Department of Mechanical and

Aerospace Engineering

in partial fulfillment of the requirements for the

degree of

Doctor of Philosophy

at the

SEOUL NATIONAL UNIVERSITY

February 2017

**Mechanics-based Design and Realization of
Electrodes for Electrochemical Energy Storages**

Jin-Myoung Lim

Submitted to the Department of Mechanical and Aerospace
Engineering
in partial fulfillment of the requirements for the degree of

Doctor of Philosophy

Author
Department of Mechanical and Aerospace Engineering
Seoul National University
Feb., 2017

Certified by.....
Prof. Maenghyo Cho
Professor of Mechanical and Aerospace Engineering,
Seoul National University
Thesis Supervisor

Accepted by.....
Prof. Yoon Young Kim
Professor of Mechanical and Aerospace Engineering
Seoul National University
Chairman

Accepted by.....
Prof. Byeng Dong Youn
Professor of Mechanical and Aerospace Engineering
Seoul National University

Accepted by.....
Prof. Do-Nyun Kim
Professor of Mechanical and Aerospace Engineering
Seoul National University

Accepted by.....
Prof. Kyeongjae Cho
Professor of Materials Science and Engineering, and Physics
The University of Texas at Dallas

Abstract

With the development of nano-sized electrode materials with complex physical and chemical phenomena from atomic scale to macroscale, multiscale mechanics analysis have occupied an indispensable manner for the design and development of energy-related materials. For electrochemical energy storages, the electrodes consist of nano-sized cathode and anode active materials, polymer binder, and conducting agent, which are operated by electrochemical reactions and by involving severe structural distortion, phase transformation, mechanical deformation, and crack generation due to relatively large size of charge carrier (i.e. Li^+ and Na^+). For these reasons, the migration of the charge carrier affects qualitative and quantitative changes of electrode materials in atomic scale, which inevitably has an effect on the electrochemical performance for the entire system. This is why mechanics-based multiscale investigation and design is indispensable for the development of electrodes in electrochemical energy storages.

We present the mechanics-based multiscale framework from first-principles calculations, statistical thermodynamics, surface dissolution, phase field model, finite element method to phase field crack model, which deals with the atomic physics and chemistry including electronic structures, nanoscale thermodynamics and kinetics, particle-level phase transformation, stress generation and mechanical deformation, and finally generation and propagation of cracks. Specifically, this methodology was developed to describe complex phase transformations, which is frequently observed from the electrodes during electrochemical operations, by defining the total free

energy functional for the combined-phase reactions. Most of electrodes involving ionic migrations during operations suffer from complicated phase transformations with the combined-phase reactions. By establishing governing equations for phase transformation, mechanical equilibrium, and fracture based on this combined-phase free energy functional, diversely derived formulations can appropriately reflect these combined-phase transformations.

Based on this mechanics-based multiscale framework, we investigated and designed major cathode materials for Li-ion battery. For high energy materials with large capacity and high operating voltage, Li-rich oxides were fundamentally investigated, and on the basis of this understanding, O-defected and Cu-doped Li-rich oxides were theoretically designed and investigated, and experimentally realized and validated. For high power materials, conventional spinel and high-voltage spinel oxides were fundamentally understood and modified through bulk and surface doping approaches using Al and Ti in the both calculation and experiments. To unfold the relationship between electrochemical characteristics, and phase transformation, we applied our multiscale method to olivine cathode, and figured out different electrochemical states with respect to degrees of phase separation. For high capacity cathodes, Ni-rich layered oxides were investigated in terms of anisotropic structural distortion, heterogeneous phase transformation, and intrinsic crack generation. Further, Ti doping was suggested to suppress the fracture.

Above theoretically designed and experimentally realized cathodes have a meaning of not only the effectiveness of as-developed methodology, but also

a foundation of experimental realizations from theoretical design without empirical approaches. The combined-phase free energy functional is determined by thermodynamic calculations from first-principles, and this free energy functional governing fundamental physics and chemistry of the multi-physics system has a various applicability to many levels of computational theories such as the phase field model, electrochemical kinetics, micro-mechanics models, and continuum models for the experimentally undescribed cases due to the complex phase behaviors. Further, the present model could be applied to various energy-related systems such as batteries, capacities, fuel cells, solar cells, and even catalyst for improving their performances and designing modified and new materials.

Keywords: Multiscale mechanics, Combined-phase reaction, First-principles calculation, Phase field model, Finite element analysis, Phase field crack model

Student Number: 2011-22894

Contents

Abstract	i
List of Figures and Tables	vii
Chapter 1 Introduction	1
1.1 Mechanics-based Multiscale Analysis and Design	1
1.2 Electrodes for Li-ion Batteries	3
1.3 Issues and Challenges	3
1.4 Combined-phase Transformation	4
1.5 Objectives and Contributions	5
Chapter 2 Atomistic Investigation	11
2.1 Density Functional Theory	11
2.2 Thermodynamics and Kinetics	12
2.3 Statistical Approach	14
2.4 Crystal Field Approach	14
Chapter 3 Combined-phase Transformation Model	17
3.1 Combined-phase Enthalpy of Formation	17
3.2 Combined-phase Free Energy Functional	19
3.3 Electrochemical Phase Transformation Model	20
Chapter 4 Mechanical Deformation and Fracture	24
4.1 Mechanical Equilibrium	24

4.2	Phase Field Crack Model	25
Chapter 5 Experimental Details		30
5.1	Synthesis of Materials	30
5.2	Materials Characterization	31
5.3	Electrochemical Measurements	31
Chapter 6 Mechanics-based Design and Realization		33
6.1	Phase Transformation of Monoclinic Li_2MnO_3	33
6.2	Effects of Defects in Monoclinic Li_2MnO_3	50
6.3	Effects of Crystal Field Stabilization in High-Mn, Li-rich Oxides	65
6.4	p-type Conductivity in High-Mn, Li-rich Oxides	83
6.5	Doping Effects on Phase Separation in Spinel LiMn_2O_4	96
6.6	Surface Doping for High-voltage Spinel $\text{LiNi}_{0.5}\text{Mn}_{1.5}\text{O}_4$	102
6.7	Elastic Softness and Power Characteristics in $\text{LiNi}_{0.5}\text{Mn}_{1.5}\text{O}_4$	116
6.8	Electrochemistry-coupled Phase Transformation in LiFePO_4	129
6.9	Heterogeneous Structural Distortions in Ni-rich Layered Oxides	137
6.10	Suppression of Fractures in Ni-rich Layered Oxides	152
Chapter 7 Conclusions and Recommendation		159
Bibliography		162
국문 초록 (Abstract in Korean)		172

List of Figures

- Figure 1.1** (a) Graphical descriptions of graphite anode with various scales and (b) various electrochemical reactions inside and outside of graphite anode, reproduced from Yan et al.7
- Figure 1.2** In-situ transmission electron microscopy (TEM) images of the first lithiation of Si nanoparticles with lithiation time of (a) 0 s, (b) 100 s, (c) 140 s, (d) 200 s, (e) 600 s and (f) 800 s, reproduced from Luo et al.8
- Figure 1.3** Cross-sectional scanning electron microscopy (SEM) images of electrodes at various cycles, from Song et al. The scale bar is 2 μm 9
- Figure 1.4** Schematic of a Li-ion battery with LiMO_2 layered cathode and graphite anode from Dunn et al.10
- Figure 2.4.1** Crystal field splitting diagrams of d-orbital for the octahedral (left) and tetrahedral (right) fields.16
- Figure 3.1.1** Combined-phase transformation behaviors of monoclinic Li_2MnO_3 cathode material with respect to the normalized Li content x in $\text{Li}_{2x}\text{MnO}_3$. (a) Enthalpy of formation H_{DFT} of all possible configurations for monoclinic (black diamonds), layered-like (blue triangles), and spinel-like (green inverse triangles) phases and the ground states (red circles). (b) Combined-phase enthalpy of formation H_{CP} (red line) with (blue circles). (c) Combined-phase free energy f_{CP} at 0 K (black solid line) and 300 K (red dashed line). (d) Predicted voltages based on the combined-phase transformation model at 0 K (blue squares and line) and 300 K (red dashed line) with experimental open-circuit voltage reproduced from Rana et al.*23
- Figure 4.2.1** (a) Sharp and (b) diffusive crack topology at $x = 0.0$. Diffusive crack modeled with the length scale $2l_0$ in terms of the crack phase field $c(r)$29
- Figure 6.1.1** Atomic model of (a) monoclinic Li_2MnO_3 structure and possible Mn migration paths. Path-i represents the migration of Mn in 4g site to 2b site

of Li, Path-ii describes the migration of Mn in 4g site to 4h site of Li, and Path-iii shows the migration of Mn in 4h site to 2b site of Li after the migration following Path-ii. Atomic models of (b) densified layered-like (LA-like) structure, where Mn is located in 2b Li site, and (c) defected spinel-like (SPI-like) structure, where Mn is located in 4h Li site.43

Figure 6.1.2 (a) Enthalpies of formation for three different structures with respect to the inverse Li content x in $\text{Li}_{2-x}\text{MnO}_3$. (b) Enthalpies of formation of ground states.44

Figure 6.1.3 (a) Atomic model of monoclinic Li_2MnO_3 structure and partial density of states (PDOS) for d-orbital of Mn ion in 4g site and p-orbital of surrounding O ions at $x = 1.25$. Atomic models of intermediate structures of (b) Path-i, (c) Path-ii, and (d) Path-iii at $x = 1.25$, and their PDOS for d-orbital of migrating Mn ion and p-orbital of surrounding O ions in intermediate structures of migration Path-i, Path-ii, and Path-iii. Fermi level is 0.0 eV (blue-dotted line). (e) Integration of occupied states of Mn ion of the monoclinic Li_2MnO_3 structure and three different intermediate structures. (f) Crystal field splitting diagram of Mn^{4+} ion located in octahedral and tetrahedral sites.45

Figure 6.1.4 (a) Powder X-ray diffraction (XRD) pattern of synthesized Li_2MnO_3 powder with a reference (JCPDS 84-1634). Field-emission scanning electron microscope (FESEM) images of the Li_2MnO_3 at (b) low magnification and (c) high magnification.46

Figure 6.1.5 (a, b) STEM images of the Li_2MnO_3 at (a) low magnification and at (b) high magnification, which is a magnified view of panel in (a). (c) FFT image of (b). (d) Atomic figure obtained by DFT calculation of relaxed monoclinic Li_2MnO_3 structure.47

Figure 6.1.6 *Ex-situ* XPS spectra after Ar ion sputtering time of 60 s on Mn 2p at different SOC states; $x = 0.0$ (OCV), 0.5, 1.0, and 1.5 of $\text{Li}_{2-x}\text{MnO}_3$48

Figure 6.1.7 (a) Galvanostatic charge-discharge profiles recorded by CC

charging mode with a constant current density of 23 mA g⁻¹ in the voltage range between 2.0 and 4.8 V vs. Li/Li⁺ at the 1st, 6th, 12th cycles and (b) Corresponding dQ/dV curves. (c) Residual Li content x in Li_{2-x}MnO₃ electrode and (d) Corresponding dQ/dV curves of the Li₂MnO₃ during the discharge at the 1st, 3rd, 5th, 7th, and 9th cycles.49

Figure 6.2.1 (a, b) FESEM images of (a) Li₂MnO₃ and (b) Li₂MnO_{3-δ}. As-synthesized Li₂MnO₃ (inset of a) and Li₂MnO_{3-δ} (inset of b) powders. (c, d) Atomic models for DFT calculations of monoclinic (c) Li₂MnO₃ and (d) Li₂MnO_{3-δ} structures (space group: C2/m).57

Figure 6.2.2 (a, b) Rietveld refinement of XRD patterns of (a) Li₂MnO₃ and (b) Li₂MnO_{3-δ} with agreement indices of the Rietveld refinement such as expected R factor (R_{exp}), R profile factor (R_p), and weighted R profile factor (R_{wp}).58

Figure 6.2.3 (a, b) STEM images of (a) Li₂MnO₃ and (b) Li₂MnO_{3-δ}. (c, d) Magnified STEM images of the panel in (a) and (b) of synthesized (c) Li₂MnO₃ and (d) Li₂MnO_{3-δ} with corresponding FFT images with zone axis (inset).59

Figure 6.2.4 XPS spectra of Mn 2p for Li₂MnO₃ and Li₂MnO_{3-δ} after an Ar ion sputtering time of 300 s.60

Figure 6.2.5 (a) Enthalpy of lithium extraction and enthalpy of formation (inset of a), enthalpy of (b) additional oxygen vacancy for Li_{2-x}MnO₃ (black circles) and Li_{2-x}MnO_{3-δ} (red squares) with respect to inverse Li content x in Li_{2-x}MnO_{3-δ}.61

Figure 6.2.6 (a) PDOS for Mn d- (black line) and O p-orbitals (red dotted line) of Li_{1.75}MnO₃ (top) and Li_{1.75}MnO_{3-δ} (bottom). (b) Average Mn- and O-ion net charges (b, inset) for Li_{2-x}MnO₃ (black circles) and Li_{2-x}MnO_{3-δ} (red squares) with respect to the inverse Li content x in Li_{2-x}MnO_{3-δ}. (c, d) Spin-resolved electronic band structures for spin-up (red line) and spin-down (blue line) for (c) Li₂MnO₃ and (d) Li₂MnO_{3-δ}. The Fermi level is 0 eV (blue dashed

line).62

Figure 6.2.7 (a) Galvanostatic charge-discharge profiles at 10 mA g⁻¹ for 1.5–4.8 V vs. Li/Li⁺ of Li₂MnO₃ (black) and Li₂MnO_{3-δ} (red) at 1st (dashed line) and 2nd (solid line) cycles, and (inset) calculated average Li₂MnO₃ (black circle) and Li₂MnO_{3-δ} (red circle) voltages. (b) Comparison of Li₂MnO₃ (black circles) and Li₂MnO_{3-δ} (red squares) cycling performances. (c) Mn migration barriers (4g to 4h site) with respect to inverse Li content *x* in Li_{2-x}MnO₃ (black line with black circles) and Li_{2-x}MnO_{3-δ} (red line with red squares). (d) Mn migration barriers (4g to 4h site) with respect to migration paths in Li_{1.75}MnO₃ (black line with black circles) and Li_{1.75}MnO_{3-δ} (red line with red squares), and their atomic structures at the migration center-point (insets).63

Figure 6.3.1 (a) Powder XRD patterns of m-HMLO (black solid line) and c-HMLO (red solid line). Enlarged insets represent superlattice peaks indexed to the (020) and (110) planes from 20° to 24°. (b, c) STEM images of as-prepared m-HMLO with EDS elemental mapping of Mn (green), O (cyan), Ni (purple), and Co (red) and corresponding SAED patterns for Li₂MnO₃ with a zone axis of [010] (inset of b) and LiNi_{1/3}Co_{1/3}Mn_{1/3}O₂ with a zone axis of [0001] (inset of c). (d, e) STEM images of as-prepared c-HMLO with EDS elemental mapping of Mn (green), O (red), Ni (yellow), and Co (cyan) at (d) low magnification, and STEM image of c-HMLO at (e) high magnification with corresponding FFT pattern and a zone axis of [010] (inset of e).77

Figure 6.3.2 (a, b) Galvanostatic charge-discharge profiles of as-prepared (a) m-HMLO and (b) c-HMLO recorded in CC mode with a constant specific current of 25 mA g⁻¹ in the voltage range between 2.0 and 4.8 V vs. Li/Li⁺ at the 1st, 2nd, and 20th cycles. (c) Corresponding *dQ/dV* curves of m-HMLO (black solid line) and c-HMLO (red dashed line) at the 1st (upper) and 20th (lower) cycles. (d) Comparison of the discharge cyclic performances of m-

HMLO (black circle) and c-HMLO (red circle).....	78
Figure 6.3.3 (a) Atomic model of $\text{Li}_{1.67}\text{Ni}_{0.11}\text{Co}_{0.11}\text{Mn}_{0.78}\text{O}_{2.67}$ (space group: $C2/m$). (b) Rietveld refinement of the XRD pattern of as-synthesized c-HMLO using the atomic model (a).	79
Figure 6.3.4 (a) Calculated voltage (blue solid line) with respect to the specific capacity predicted by the Li concentration and the 1st charge profile of the c-HMLO from Figure 6.3.2b. Average charge variations of Ni, Co, Mn, and O ions (inset of (a)) according to the calculated voltage. (b, c, d) PDOS for (b) Mn, (c) Co, and (d) Ni d-orbitals of $\text{Li}_{1.67}\text{Ni}_{0.11}\text{Co}_{0.11}\text{Mn}_{0.78}\text{O}_{2.67}$ (black solid line) and $\text{Li}_{1.34}\text{Ni}_{0.11}\text{Co}_{0.11}\text{Mn}_{0.78}\text{O}_{2.67}$ (red dashed line), where the Fermi level is 0.0 eV (blue dashed line).	80
Figure 6.3.5 (a) Migration barriers of Mn (black circle), Co (red square), and Ni (blue triangle) ions in terms of the inverse Li content x in $\text{Li}_{1.67-x}\text{Ni}_{0.11}\text{Co}_{0.11}\text{Mn}_{0.78}\text{O}_{2.67}$ from the initial TM layer to the final Li layer <i>via</i> the middle tetrahedral site (inset). (b) Net charges of Mn (black circle), Co (red square), and Ni (blue triangle) ions in the three different migration sites (inset of (a)). (c, e, g) PDOS for (c) Mn, (e) Co, and (g) Ni d-orbitals in the initial octahedral site (black solid line) and middle tetrahedral site (red dashed line) for $\text{Li}_{1.11}\text{Ni}_{0.11}\text{Co}_{0.11}\text{Mn}_{0.78}\text{O}_{2.67}$, where the Fermi level is 0.0 eV (blue dashed line). (d, f, h) Corresponding CFSDs of (d) Mn, (f) Co, and (h) Ni d-orbitals in the initial octahedral site (upper) and middle tetrahedral site (lower) for $\text{Li}_{1.11}\text{Ni}_{0.11}\text{Co}_{0.11}\text{Mn}_{0.78}\text{O}_{2.67}$	81
Figure 6.3.6 (a) Atomic model of $\text{Li}_{1.67}\text{Ni}_{0.11}\text{Co}_{0.11}\text{Mn}_{0.67}\text{Cu}_{0.11}\text{O}_{2.67}$ (space group: $C2/m$). (b) Migration barriers of Cu ion (green diamond) in terms of the inverse Li content x in $\text{Li}_{1.67-x}\text{Ni}_{0.11}\text{Co}_{0.11}\text{Mn}_{0.67}\text{Cu}_{0.11}\text{O}_{2.67}$ from the initial TM layer to the final Li layer <i>via</i> the middle tetrahedral site (inset). (c) Net charges of Cu ions (green diamond) at the three different migration sites (inset of (b)). (d) PDOS for Cu d-orbitals in the initial octahedral site (black solid line) and middle tetrahedral site (red dashed line) for	

$\text{Li}_{1.67}\text{Ni}_{0.11}\text{Co}_{0.11}\text{Mn}_{0.67}\text{Cu}_{0.11}\text{O}_{2.67}$, where the Fermi level is 0.0 eV (blue dashed line). (e) Corresponding CFSDs of Cu d-orbital in the initial octahedral site (upper) and middle tetrahedral site (lower) for $\text{Li}_{1.67}\text{Ni}_{0.11}\text{Co}_{0.11}\text{Mn}_{0.67}\text{Cu}_{0.11}\text{O}_{2.67}$82

Figure 6.4.1 (a) Powder XRD patterns of HMLO (black solid line) and CuHMLO (red solid line). (b) HRTEM image of CuHMLO with EDS elemental mapping of Ni (green), Co (blue), Mn (purple), Cu (yellow), and O (cyan).....90

Figure 6.4.2 High magnification STEM images of (a) HMLO and (d) CuHMLO with the corresponding FFT patterns of (b) HMLO with a zone axis of [010] and (e) CuHMLO with a zone axis of [0-10]. Ideal crystal structures along the same directions with the STEM images of (c) HMLO and (f) CuHMLO obtained by first-principles calculations.91

Figure 6.4.3 (a, b) Galvanostatic charge-discharge profiles of the prepared HMLO (black solid line) and CuHMLO (red solid line) between 2.0 and 4.8 V vs. Li/Li^+ with a constant specific current of 25 mA g^{-1} in the (a) 1st and (b) 10th cycles. (c, d) Charge (bold triangles) and discharge (hollow triangles) cycle performances of HMLO (black inverse triangles) and CuHMLO (red triangles) with constant specific currents of (c) 40 mA g^{-1} and (d) 100 mA g^{-1} between 2.0 and 4.8 V vs. Li/Li^+ . (e) Rate capability of the discharge specific capacity between 20 mA g^{-1} and 400 mA g^{-1} for HMLO (black inverse triangles) and CuHMLO (red triangles).92

Figure 6.4.4 (a, b) Atomic models of (a) HMLO and (b) CuHMLO (space group: $C2/m$). (c, d) Rietveld refinements of the XRD patterns of (c) HMLO and (d) CuHMLO using the atomic models in parts (a) and (b), and the agreement indices of the R profile and the weighted R profile factors.93

Figure 6.4.5 Total density of states (TDOS) of (a) HMLO and (b) CuHMLO.94

Figure 6.4.6 (a, b, c) Partial (projected) density of states (PDOS) for the (a)

Ni, (b) Co, and (c) Mn d-orbitals of HMLO (black solid lines) in their fully-lithiated states. (d, e, f, g) PDOS for the (d) Ni, (e) Co, (f) Mn, and (g) Cu d-orbitals of CuHMLO (red solid lines) in their fully-lithiated states. (h, i, j, k) Corresponding crystal field splitting diagrams (CFSDs) for the (h) Ni, (i) Co, (j) Mn, and (k) Cu d-orbitals in the octahedral sites for HMLO and CuHMLO. .95

Figure 6.5.1 Zero-temperature mixing enthalpy calculated from first-principles calculations in (a) $L_{1-x}MO$ (black circles) and (b) $L_{1-x}MAO$ (gray circles) from $x = 0$ to 1.99

Figure 6.5.2 Homogeneous bulk free energy f_h of (a) LMO and (b) LMAO, and the chemical potential $-\mu_h/e$ of (c) LMO and (d) LMAO at room temperature with respect to the inverse Li content x . The black dashed lines in (a) and (c) are the spinodal points of LMO and the blue dashed lines in (b) and (d) are the spinodal points of LMAO.100

Figure 6.5.3 Phase separation kinetics in (a) LMO (SOC = 82.8%) and (b) LMAO (SOC=64.4%) during relaxation from a solid solution at various dimensionless time \hat{t} 101

Figure 6.6.1 (a) Atomic model of $LiNi_{0.5}Mn_{1.5}O_4$. (b) Enthalpy of formation with respect to the inverse Li content x . Partial (projected) density of states of (c) Ni d-orbital and (d) Mn d-orbital, and (e) O p-orbital, in $Li_{1.0}Ni_{0.5}Mn_{1.5}O_4$ (red solid line) and $Li_{1.0}Ni_{0.5}Mn_{1.5}O_4$ (blue dotted line).109

Figure 6.6.2 Atomic models of (a) the (111) surface, and the corresponding PDOS of the Ni (gray lines) and Mn (purple lines) d-orbitals at (b) semi-bulk and (c) surface regions. Atomic models of (d) the (400) surface, and the corresponding PDOS of the Ni (gray lines) and Mn (purple lines) d-orbitals at (e) semi-bulk and (f) surface regions.110

Figure 6.6.3 Surface doping models with one doping atom on the (a) (111) and (b) (400) surfaces in LNMO. (c) Calculated dissolution energies of Ni and Mn ions at (111) and (400) surfaces. Average net charge of O ions around and

away from the Ti ions on the (d) (111) and (e) (400) surfaces of TSD-LNMO. PDOS of O p-orbitals of O ions around Ti (red solid line) and other O ions (green dashed line) on (f) (111) and (g) (400) surfaces of TSD-LNMO. The Fermi level is 0 eV (gray dotted line)..... **111**

Figure 6.6.4 (a) X-ray diffraction patterns of pristine LNMO (black), TSD-LNMO (red). EDS mapping data of ion-sliced HRTEM for (b) Ni, (c) Mn, (d) O, and (e) Ti in TSD-LNMO..... **112**

Figure 6.6.5 (a) X-ray photoelectron spectroscopy (XPS) spectra of Ti 2p of TSD-LNMO. Inset: (b) calculated PDOS of Ti d-orbital on the (111) and (400) surfaces (red solid and green dashed lines, respectively). The Fermi level is 0 eV (gray dotted line). (c) The O 1s peak for TSD-LNMO (purple open circles) and LNMO (green open circles). **113**

Figure 6.6.6 Concentrations of Ni (open squares) and Mn (filled squares) in the electrolyte with respect to the storage time (week) for LNMO (black) and TSD-LNMO (red). **114**

Figure 6.6.7 (a) Discharge cyclic performance and (b) initial charge-discharge profiles at 25 °C, of LNMO (black), and TSD-LNMO (red) at 1C. (c) Discharge cyclic performance and (d) initial charge-discharge profiles at 40 °C. **115**

Figure 6.7.1 (a, b) Rietveld refinement of the XRD patterns of as-synthesized (a) LNMO and (b) LNMTO. The atomic models are described in each inset in the figures: Li is green, Mn is purple, Ni is gray, O is red, and Ti is blue. (c, d) STEM images and the line profiles (lower graphs) with *d*-spacings along each yellow line for as-prepared (c) LNMO (black solid line) and (d) LNMTO (red solid line)..... **124**

Figure 6.7.2 (a, b) XPS spectra of (a) Ti2p for LNMTO and (b) O1s for LNMO (black circles) and LNMTO (red triangles) after Ar ion sputtering for 300 s. (c) Li⁺ diffusion coefficient (*D*_{Li}) calculated from the GITT curves for LNMO (black circles) and LNMTO (red triangles) as a function of cell

voltage during the discharge processes. (d) Migration barriers of the Li ion in LNMO (black circles) and LNMTO (red triangles).125

Figure 6.7.3 (a, b) First-principles mixing enthalpy per *f.u.* at 0 K of (a) L_{1-y} NMO (black circles) and (b) L_{1-y} NMTO (red triangles) as a function of the inverse Li content, *y*. (c) Homogeneous bulk free energy, f_h , per f.u. and (d) open-circuit voltage at 300 K of L_{1-y} NMO (black solid line) and L_{1-y} NMTO (red dashed line) as a function of the inverse Li content, *y*, with miscibility gaps of LNMO (black shaded area) and LNMTO (red shaded area), and the GITT curves (inset) of LNMO (black solid line) and LNMTO (red solid line) as a function of time between 3.5 and 4.9 V vs. Li/Li⁺.126

Figure 6.7.4 (a) Volumetric strain, ϵ_v , of LNMO (black circles and dashed line) and LNMTO (red triangles and dashed line) with respect to the inverse Li content, *y*. (b) Normalized DFT energy with a fitted line according to the Birch-Murnaghan equation of state (EOS) of LNMO (black circles and solid line) and LNMTO (red triangles and solid line) with respect to the volume ratio (V/V_0). (c, d) Distribution of elastic stress caused by the phase transformation from a solid solution of *y* = 0.5 in LNMO and LNMTO at the dimensionless time, $\hat{t} = 3.0$127

Figure 6.7.5 (a, b) Phase separation kinetics in (a) L_{1-y} NMO and (b) L_{1-y} NMTO from a solid solution of *y* = 0.5 at the dimensionless time, \hat{t} (0.0, 1.0, 2.0, and 3.0). (c) Rate capability at various rates and (d) charge-discharge profiles at specific currents of 800 mA g⁻¹ and 1000 mA g⁻¹ for LNMO (black circle and lines) and LNMTO (red circle and lines). (a, b) Phase separation kinetics in (a) L_{1-y} NMO and (b) L_{1-y} NMTO from a solid solution of *y* = 0.5 at the dimensionless time, \hat{t} (0.0, 1.0, 2.0, and 3.0). (c) Rate capability at various rates and (d) charge-discharge profiles at specific currents of 800 mA g⁻¹ and 1000 mA g⁻¹ for LNMO (black circle and lines) and LNMTO (red circle and lines).128

Figure 6.8.1 (a) H_{DFT} (black diamonds) and the ground states (red circles), (b) H_{CP} (red line) with $H_{DFT}^{i,f}$ (blue circles) and scheme of double-well function (inset), (c, d) f_{CP} (c) and $-\mu_{CP}/e$ (d) at 0 K (black solid line) and 300 K (red dashed line), and (e) experimental open circuit voltage (OCV, black circles) reproduced from Yamada et al.[19] and the predicted voltages of this model at 0 K (blue squares and line) and 300 K (red dashed line) as function of Li content x in Li_xFePO_4133

Figure 6.8.2 (a, b) Atomic model for olivine LiFePO_4 along (a) ab and (b) ac planes. (c-h) Phase transformations in the nanodomain with dimensions of 15.17×15.17 nm in Li_xFePO_4 during relaxation from a solid solution at dimensionless time $\hat{t} = 3.0$ and dimensionless current $\hat{I} = 0.0$. As illustrated in Figure 6.8.1d, the initial concentrations lie before, at the middle, and after the spinodal points ($x =$ (c) 0.19, (d) 0.25, (e) 0.5, (f) 0.69, and (g) 0.75), and (h) the middle of the one-phase reaction region at $x = 0.97$134

Figure 6.8.3 Elastic stresses (a) σ_a , (b) σ_b , and (c) σ_{ab} during phase transformation from $x = 0.5$ at dimensionless time $\hat{t} = 3.0$ and dimensionless current $\hat{I} = 0.0$135

Figure 6.8.4 (a) Overpotential η as a function of dimensionless time \hat{t} for dimensionless current $\hat{I} = 5.0$. Red dotted and blue solid lines indicate overpotential for $x = 0.69$ and 0.75, respectively. (b-i) Distributions of concentration during phase transformations at $x =$ (b-e) 0.69 (upper row) and (f-i) 0.75 (lower row) for $\hat{t} =$ (b, f) 0.0, (c, g) 1.0, (d, h) 2.0, and (e, i) 3.0. ...136

Figure 6.9.1 Atomic models of Ni-rich $\text{LiNi}_{0.8}\text{Co}_{0.1}\text{Mn}_{0.1}\text{O}_2$ (NCM811) layered oxide ($R-3m$) projected onto the (a) bc and (b) ab planes.145

Figure 6.9.2 (a, b, c, d) Partial density of states (PDOSs) of (a) Ni d - (gray solid line), (b) Co d - (blue solid line), (c) Mn d - (purple solid line), and (d) O p - (red solid line) orbitals in $\text{LiNi}_{0.8}\text{Co}_{0.1}\text{Mn}_{0.1}\text{O}_2$. (e, f, g, h) PDOSs of (e) Ni

d- (gray dashed line), (f) Co *d*- (blue dashed line), (g) Mn *d*- (purple dashed line), and (h) O *p*- (red dashed line) orbitals in $\text{Li}_{0.0}\text{Ni}_{0.8}\text{Co}_{0.1}\text{Mn}_{0.1}\text{O}_2$. The Fermi level is 0.0 eV (green dotted line).146

Figure 6.9.3 (a) Calculated *a* (blue inverse triangles and solid line, left axis) and *c* lattice parameters (red triangles and solid line, right axis), and (b) volume of cell (black circles and solid line) with respect to the inverse Li content *x* in $\text{Li}_{1-x}\text{Ni}_{0.8}\text{Co}_{0.1}\text{Mn}_{0.1}\text{O}_2$147

Figure 6.9.4 (a) Mixing enthalpies from density functional theory (DFT) calculations (black circles) with ground states (yellow diamonds and blue line). (b) Open-circuit voltage (OCV) calculated using first principles (blue solid line) and reproduced by experiment (black circles and line) from Ohzuku et al. versus inverse Li content *x* in $\text{Li}_{1-x}\text{Ni}_{0.8}\text{Co}_{0.1}\text{Mn}_{0.1}\text{O}_2$148

Figure 6.9.5 (a) Combined-phase (CP) free energy (blue solid line) and (b) CP chemical potential (red solid line) at room temperature (300 K) with spinodal regions (green shaded areas) with respect to inverse Li content *x* in $\text{Li}_{1-x}\text{Ni}_{0.8}\text{Co}_{0.1}\text{Mn}_{0.1}\text{O}_2$149

Figure 6.9.6 Meso-scale phase transformations in the nanodomain with dimensions of 31.36×31.36 nm in $\text{Li}_{1-x}\text{Ni}_{0.8}\text{Co}_{0.1}\text{Mn}_{0.1}\text{O}_2$ at room temperature (300 K) from a solid solution of inverse Li concentration *x* = 0.65 (a, b, c, d) and 0.85 (e, f, g, h) at dimensionless time $\hat{t} = 5$. (a, e), (b, f), (c, g), and (d, h) are the distributions on the *ac* plane of the inverse Li concentration *x*, strain in *a* direction ε_1 , strain in *c* direction ε_3 , and volumetric strain ε_V , respectively.150

Figure 6.9.7 Schematic illustration of micro-crack generations in secondary particles on the interfaces of the contracted primary particles during delithiation.151

Figure 6.10.1 Atomic models of (a) Ni-rich $\text{LiNi}_{0.833}\text{Co}_{0.083}\text{Mn}_{0.083}\text{O}_2$ (NCM811) and (b-d) Ti-doped NCM811 (Ti-NCM811) with three different Ti

positions; (b) Ni layer, (c) Ni-Mn layer, and (d) Ni-Co layer. (e) Relative total energy of the three different Ti-NCM811. Surface atomic models of (f) NCM811 and (g) Ti-NCM811.....155

Figure 6.10.2 Calculated (a) a and (b) c lattice parameters, and (c) volume of cell with respect to the inverse Li content x 156

Figure 6.10.3 Mixing enthalpies from density functional theory (DFT) calculations of (a) NCM811 and (b) Ti-NCM811, and (c) combined-phase (CP) free energy and (d) CP chemical potential at room temperature (300 K) with respect to inverse Li content x157

Figure 6.10.4 Distributions of (a, e) concentration of inverse Li content x , elastic stresses in (b, f) a and (c, g) c directions, and (d, h) crack phase field c for both (a, b, c, d) NCM811 and (e, f, g, h) Ti-NCM811 in the nanodomain at room temperature (300 K) from a solid solution of inverse Li concentration $x = 0.85$ at dimensionless time $\hat{t} = 3$158

List of Tables

Table 6.2.1 Comparison of oxygen deficiency δ , volume, and average bond length between Mn and O of Li_2MnO_3 and $\text{Li}_2\text{MnO}_{3-\delta}$, obtained by Rietveld refinement of XRD patterns and DFT calculations.	64
---	-----------

Chapter 1

Introduction

1.1 Mechanics-based Multiscale Analysis and Design

Multiscale analysis and design means an in-depth theoretical approach for complex systems generating various physical, chemical, electrical, and mechanical phenomena with respect to broad range of length and time scales, which is widely applied to aerospace materials, biomaterials, building materials, energy materials, and so on. To make this possible, diverse methodologies with scale bridging models are utilized from atomic scale to macroscale simulations, since the multiscale problem cannot be solved by single existing method.[1] First-principles calculations, molecular dynamics, and Monte Carlo simulations could be used for atomic scale, and various statistical approaches and phase field model would be adopted for mesoscale. Then, micromechanical models, continuum mechanics, electrochemistry, crack propagation, heat and mass transfer, thermal expansion, and fluid mechanics could be utilized for macroscale simulations.

Among various multiscale problems, multiscale approaches are indispensably necessary to energy-related materials for electrochemical

energy storages such as cathode, anode, electrolyte, and etc., because they represent electro-mechano-chemical coupled reactions occurred in the atomic structure, affecting electrochemical performances in macroscale. For example, Figure 1.1a shows the descriptions of graphite anode with various scales. In the electrode level (macroscale), graphite anode consists of aggregated graphite materials with various directions, and in the particle level (mesoscale), graphite anode is composed of graphene layers. Finally, the atomic structure of graphite anode has carbon hexagon layers with AB stacking. As reactions near the graphite anode, various electrochemical reactions such as intercalation, decomposition, solvent co-intercalation, deposition, diffusion, migration, electron transfer and etc. as shown in Figure 1.1b. Due to these diverse reactions with various scales of graphite anode, different kinds of methodologies and theories should be performed.

Especially, the electrodes for electrochemical energy storages have a critical issue related to mechanical deformation and crack propagation, since a charge carrier such as Li^+ or Na^+ is inserted and extracted into and out of the electrodes during electrochemical reactions, which causes volume expansion and contraction from 10% to 300%, and induces fractures of primary and secondary particles. For example, Figure 1.2 shows a large volume expansion of Si anode during insertion of Li ion, and Figure 1.3 represents crack generations and propagations of a transition metal (TM) layered oxide cathode during cycles, which indicates nano- and micro-scale damage mechanisms during electrochemical reactions such as mechanical deformation, internal particle voiding, exfoliation, flaking, and fracture. For these reason, beyond the existing multiscale theories, new class of multiscale approaches coupled with electrochemistry and mechanics at various scales are crucial for the design and analysis of electrodes for electrochemical energy storages.

1.2 Electrodes for Li-ion Batteries

Lithium ion batteries (LIBs) have been considered as the most promising power sources for several decades; they have been widely used in applications ranging from portable electronics to large-scale energy storage such as electric vehicles (EVs) and energy storage systems (ESSs).[2] As described in Figure 1.4, LIBs is electrochemically working by migration of a charge carrier (Li^+) across the electrolyte located between positive electrode (cathode) and negative electrode (anode).

Based on this working mechanism, high capacity means the capability of containing large amount of Li^+ in the cathode and anode, and high voltage indicates the high electrochemical potential when Li^+ is inserted and extracted from the cathode and anode in the theoretical manner, which high capacity and voltage means high energy. Furthermore, cyclic performance and voltage drop are determined by phase and structural stability of cathode and anode during electrochemical reactions. Finally, power characteristics is dependent upon the rate of migration of Li^+ , which is mostly determined by ionic and electronic conductivity. Therefore, the electrochemical performance of LIBs is affected these whole factors compositively.

1.3 Issues and Challenges

As explained before, there are critical issues and challenges to improve and design the electrodes for electrochemical energy storages such as the capability for containing Li^+ , potential of insertion and extraction, stabilities, conductivities, and additionally low cost and environmental friendliness. In the aspect of theoretical investigation and design, the amount of Li^+ in the electrodes is relevant to the formation energy with respect to the content of Li^+ , and electrochemical potential could be determined by phase stability *versus* the content of Li^+ . Cyclic performance are closely related to phase transformation and surface dissolution of electrodes, which is relevant to

thermodynamic and kinetic stability of structures during lithiation and delithiation. For the power characteristics, ionic conductivity is determined by migration of Li^+ inside the structure that means migration barrier, length, and space are important factor. Finally, electronic conductivity can be predicted and tuned by band gap of electronic structures for electrode systems.

These can be calculated by atomic-scale simulations such as first-principles calculations, molecular dynamics, and statistical thermodynamics, and for the particle-level phenomena, mesoscale simulation methodologies are necessary such as phase field model. Based on the atomic-scale physics, Gibbs free energy for entire system can be defined for constituting governing equation of phase field model. This phase field model using the bridged Gibbs free energy can describe phase transformation behaviors considering detail atomic properties. Further, electrochemical changes, mechanical deformations, and crack generations dependent on the phase transformation can be predicted in macroscale by bridging the phase field model to continuum scale methodologies. Therefore, generalized electrochemical performances with mechanical behaviors can be effectively investigated by the mechanics-based multiscale approaches.

1.4 Combined-phase Transformation

The complex phase transformations of the electrodes utilized for electrochemical energy storage are based on the combined one- and two-phase reactions. These combined-phase (CP) reactions result in the drawback of various voltage plateaus being formed in the electrochemical charge and discharge profiles. Moreover, these complex phase transformation have an influence on the electrochemical performances.[3]

In this context, computational studies have investigated the complex phase behaviors of electrodes. As regards the atomic scale, simulations based on first-principles calculations have been conducted for predicting the phase

stability,[4-6] phase diagram,[7-9] and transition metal diffusion kinetics.[10-12] However, for particle-level descriptions of the phase transformation, mesoscale simulations such as the phase field model are valid only for two-phase reactions with experimental parameters.[13-19] This is because, in the case of CP reactions, experimental signals measured for the phase transformations are likely to be superficial due to the complexity of CP behaviors, and therefore, the need for a computational model that describes these CP reaction mechanisms without requiring the extraction of parameters from experimental measurement becomes crucial.

Thus, a multiscale model connecting atomic-level calculations to mesoscale phase behaviors is indispensable in analyzing the CP reactions without extracting model parameters from experimental measurements. Further, the investigation of phase transformations and mechanical deformations at different electrochemical states becomes essential to better understand the performances of electrodes for electrochemical energy storage; thus, the development of a multiscale model that also considers electrochemical aspects and stress generation is crucial.

1.5 Objectives and Contributions

In this dissertation, we introduce a mechanics-based multiscale methodologies for the electrodes of electrochemical energy storages suffering from the combined one- and two-phase reactions by utilizing first-principles calculations, statistical thermodynamics, electronic structures, crystal field theory, definition of various free energy functional, phase field model, electrochemical model, continuum theory with finite element method, and phase field crack model.

From the atomistic part of this methodology, intrinsic phase and structural thermodynamic stability, qualitative and quantitative electronic characters, kinetic characteristics, and surface properties can be predicted.

Based on this atomistic properties, total free energy functional and governing equations can be defined, which can evaluate chemical potential, the miscibility gap, spinodal region, voltage profile, and phase transformation kinetics of the electrodes in the electrochemical reactions. Furthermore, this model describes the phase transformation behaviors of the complicated CP reactions in stress generations and crack propagations in conjunction with both electrochemical equilibrium and non-equilibrium states, which cannot be investigated only by experimental approaches.

Using these methodologies, we theoretically designed, experimentally realized, and reported various cathode materials for LIBs such as Li-rich oxides,[11] oxygen-defected Li-rich oxides,[20] TMs-doped Li-rich oxides,[21] p-type conducting Li-rich oxides,[22] Al-doped conventional spinel,[23] surface-doped high-voltage spinel,[24] Ti-doped high-voltage spinel,[25] olivine iron phosphate,[1] Ni-rich layered oxides,[26] and Ti-doped Ni-rich layered oxides in Chapter 6. These resulting phenomena describe distinct behaviors that cannot be reproduced by non-multiscale theories and experiments.

In conclusion, the present methodologies could be applied to various electrode systems with complex electrochemical reactions and mechanical failure in the absence of experimental model parameters, which can be utilized over a wide range of developed simulation methodologies. Further, the successful experimental realizations of the theoretical designs could be one of the most effective paradigm for the development of novel materials.

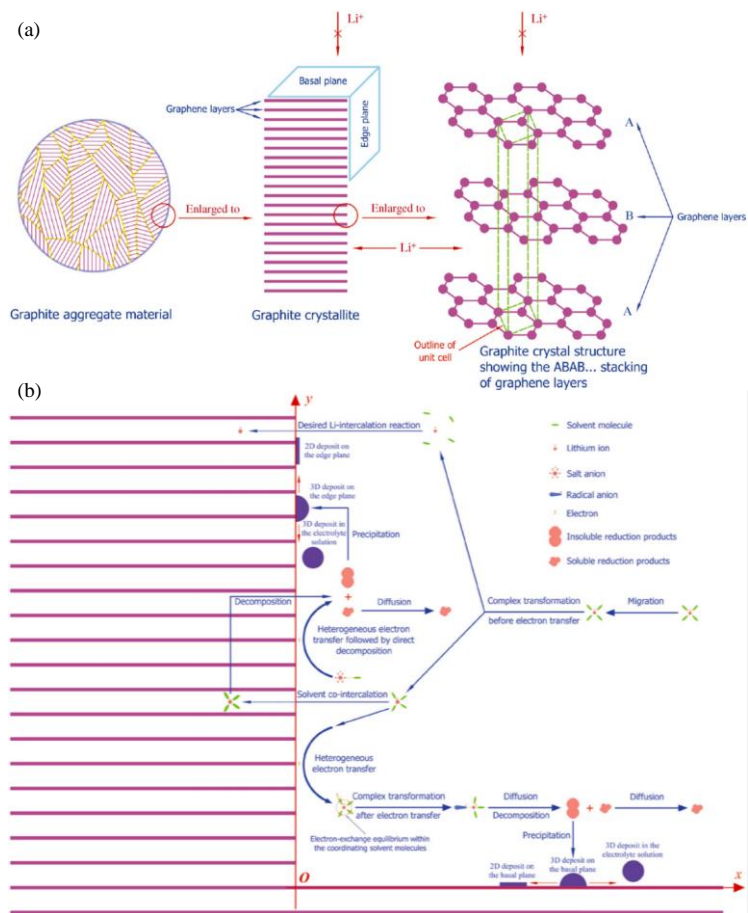


Figure 1.1 (a) Graphical descriptions of graphite anode with various scales and (b) various electrochemical reactions inside and outside of graphite anode, reproduced from Yan et al.[27]

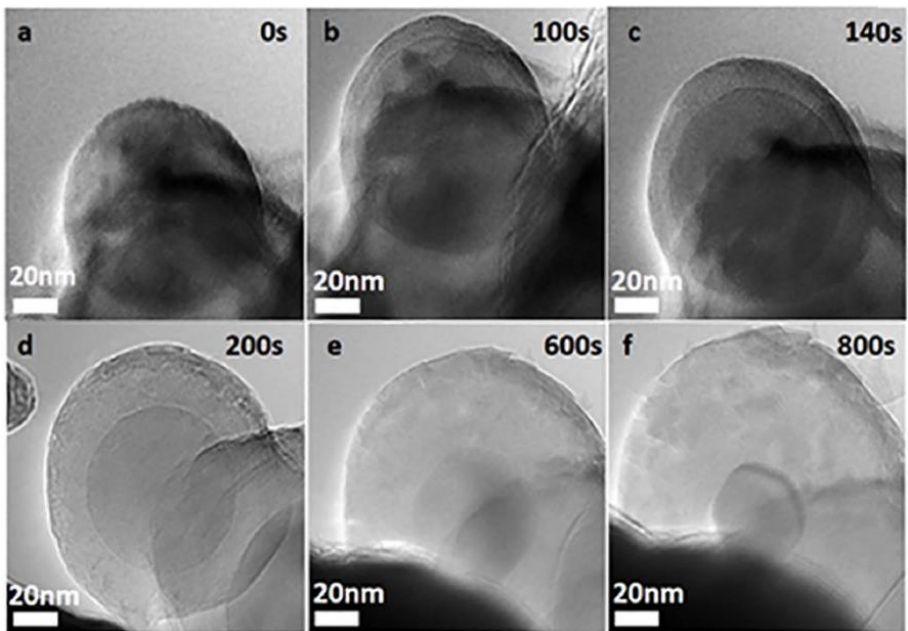


Figure 1.2 *In-situ* transmission electron microscopy (TEM) images of the first lithiation of Si nanoparticles with lithiation time of (a) 0 s, (b) 100 s, (c) 140 s, (d) 200 s, (e) 600 s and (f) 800 s, reproduced from Luo et al.[28]

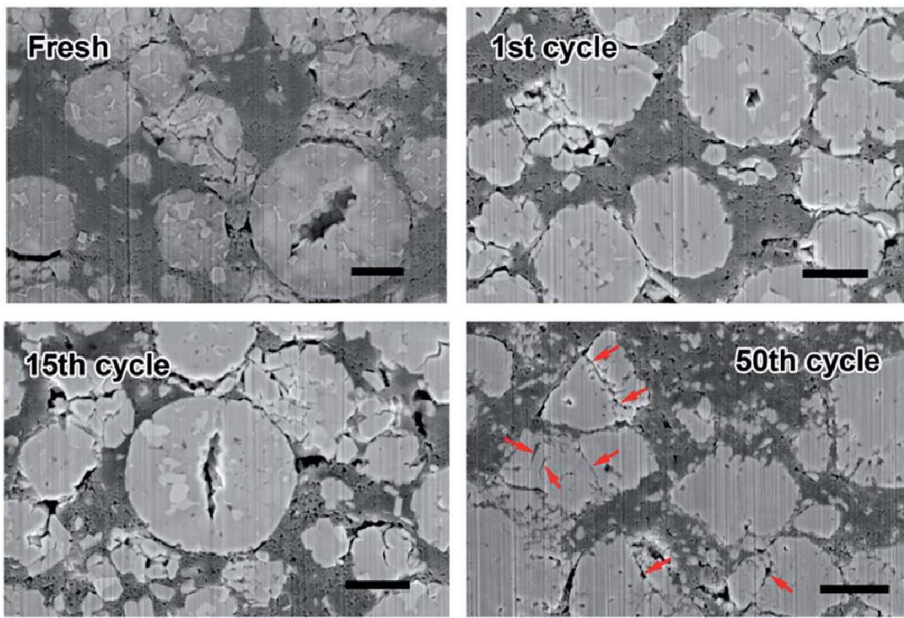


Figure 1.3 Cross-sectional scanning electron microscopy (SEM) images of electrodes at various cycles, from Song et al.[29] The scale bar is 2 μm.

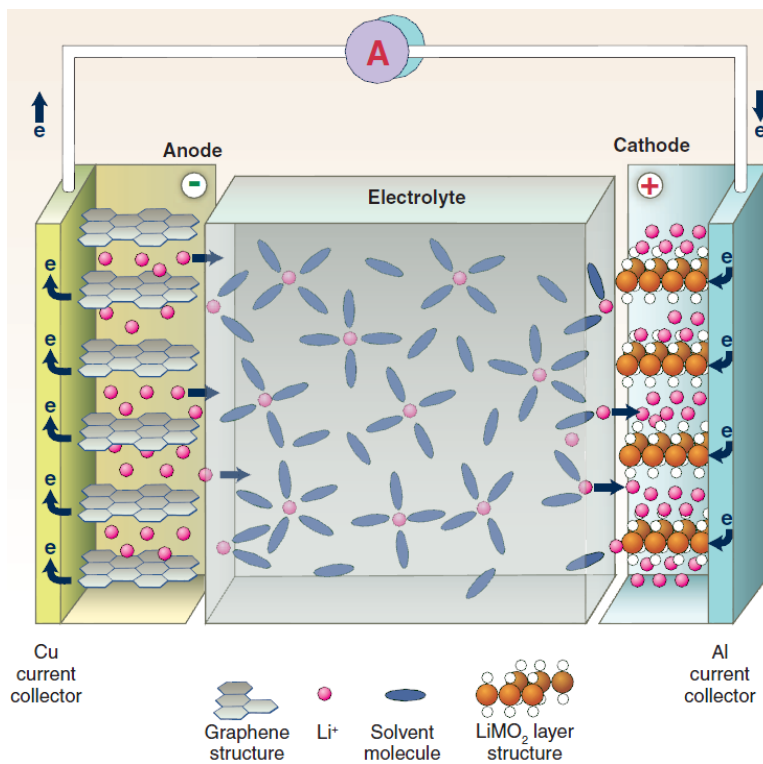


Figure 1.4 Schematic of a Li-ion batteries with LiMO_2 layered cathode and graphite anode from Dunn et al.[30]

Chapter 2

Atomistic Investigation

2.1 Density Functional Theory

As a first step of multiscale analysis, we have utilized first-principles calculations (or *ab initio* calculations), which requires only fundamental information such as nuclear charge, the number of electrons, and so on, distinguished from empirical calculations using fitting parameters. Basically, by solving the time-independent Schrödinger equation with exchange-correlation potential \hat{V}_{XC} , the whole information of the given system is calculated in the form of wave function Ψ using density functional theory (DFT) as follows:[31, 32]

$$\hat{H}\Psi = \left[\hat{T} + \hat{V} + \hat{U} + \hat{V}_{XC} \right] \Psi = E\Psi \quad (2.1),$$

where \hat{H} represents the Hamiltonian operator, \hat{T} the kinetic energy operator, \hat{V} the potential energy operator from the external field, \hat{U} the electron-electron interaction energy operator, and E the total energy.

In this work, a spin-polarized generalized gradient approximation (GGA) using the parameterized exchange correlation functional according to

Perdew-Wang 91[33] and Perdew-Burke-Ernzerhof (PBE).[34] We have used the projector-augmented wave (PAW) and a plane-wave basis set implemented in the Vienna *Ab Initio* Simulation Package (VASP).[35] We have determined the cut-off energy of a plane-wave basis and k -point meshes by a convergence test of total energies within 0.2 meV per formula unit (*f.u.*). The strong correlation effect among d-orbital electrons of transition metals was resolved with the Hubbard U correction,[36] where the U values were selected from previous works.[11, 20, 21, 23, 37-39] Both ions and cells were relaxed in this work. For the surface calculations, the surface model has carefully developed based on the Gibbs dividing surface model.[40] Further, the cell volume was fixed and internal relaxations of the ions were conducted by Hellman-Feynman forces.

2.2 Thermodynamics and Kinetics

It is important to compare thermodynamic stabilities and kinetic possibilities of various atomic structures for various modifications of electrodes such as Li extraction, oxygen defect and evolution, elemental doping, dissolutions, and so on. For this reason, we introduced several thermodynamic quantities for the general case of $\text{Li}_x\text{TM}_y\text{O}_z$ (Li denotes lithium as the charge carrier, TM the transition metals, and O the oxygen as the anion) as below.

For the configurational stability of Li-extracted structures, the enthalpy of formation H_{DFT} for the Li configurations is determined as follows:

$$\mathbf{H}_{DFT}(\mathbf{x}) = \mathbf{E}_{\text{Li}_x\text{TM}_y\text{O}_z}^{DFT} - x\mathbf{E}_{\text{Li}}^{DFT} - (1-x)\mathbf{E}_{\text{Li}_0\text{TM}_y\text{O}_z}^{DFT} \quad (2.2),$$

where x represents the normalized content of Li ($0 \leq x \leq 1$), and $\mathbf{E}_{\text{Li}_x\text{TM}_y\text{O}_z}^{DFT}$ the absolute energy of $\text{Li}_x\text{TM}_y\text{O}_z$ as calculated from DFT calculations. For the thermodynamic stability of oxygen defect in $\text{Li}_x\text{TM}_y\text{O}_z$ can be understood by calculating the formation enthalpy of oxygen defect H_O as following equation:

$$\mathbf{H}_O(\mathbf{x}, \delta) = \mathbf{E}_{\text{Li}_x\text{TM}_y\text{O}_{z-\delta}}^{\text{DFT}} - \mathbf{E}_{\text{Li}_x\text{TM}_y\text{O}_z}^{\text{DFT}} + \delta \frac{\mathbf{E}_{\text{O}_2}^{\text{DFT}}}{2} \quad (2.3),$$

where δ denotes the amount of oxygen defect.

For the redox potential of the electrochemical reactions, delithiation potential V can be described as follows:

$$V = -\frac{\Delta G_R}{(x_2 - x_1)F} \quad (2.4),$$

where F is the Faraday constant and ΔG_R the change of the Gibbs free energy for the delithiation reaction.

For the surface calculations, the surface energy γ^s can be evaluated by the DFT energy of the surface model E_S and bulk model E_B , and the surface area A of one side of the slab as follows:

$$\gamma^s = \frac{E_S - E_B}{2A} \quad (2.5).$$

Further, the dissolution energy H_{Dis} can be determined as follows:

$$\mathbf{H}_{Dis}(\mathbf{x}, \eta) = \mathbf{E}_{\text{Li}_x\text{TM}_{y-\eta}\text{O}_z}^{\text{DFT}} - \mathbf{E}_{\text{Li}_x\text{TM}_y\text{O}_z}^{\text{DFT}} + \eta \cdot \mu_{TM} \quad (2.6),$$

where η denotes the amount of dissolved TM, and μ_{TM} the chemical potential of the TM element. In this work, μ_{TM} is determined by TM^{2+} state in TMO compounds, because the HF generation from the electrolyte oxidation causes the dissolution of TM in the form of TM^{2+} , [38, 41] which can be defined as follows:

$$\mu_{TM} = \mathbf{E}_{TMO}^{\text{DFT}} - \frac{\mathbf{E}_{\text{O}_2}^{\text{DFT}}}{2} \quad (2.7).$$

For the kinetic investigations, elemental migrations were simulated with various pathways using the climbing-image nudged elastic band (ciNEB) method.[42]

2.3 Statistical Approach

Statistical methods for predict the thermodynamic quantities of larger atomic systems, because the first-principles calculations requires enormous computing resources and time. We adopted the cluster expansion method (CEM) based on the total energies calculated by DFT calculations.[43, 44] The energies estimated by CEM can be described with the effective cluster interaction (ECI) coefficients as follows:

$$E_{CEM}(\varphi) = \sum_{\sigma} m_{\sigma} J_{\sigma} \left\langle \prod_{i \in \sigma'} \varphi_i \right\rangle \quad (2.8),$$

where J_{σ} is an ECI coefficient corresponding to a cluster σ , and φ denotes a configuration with occupation variables of +1 for Li and -1 for vacancy at Li sites. σ' indicates a cluster that is equivalent to cluster σ in terms of crystal symmetry, and m_{σ} is multiplicities in the number of clusters equivalent in terms of their crystal symmetry. On the basis of CEM, above-mentioned various energies for larger atomic systems can be estimated.

2.4 Crystal Field Approach

In order to describe transition metal coordination complexes of electrodes, we introduced the crystal field theory (CFT), which is developed by H. Bethe[45] and subsequently modified toward ligand field theory (LFT) by J.H. Van Vleck.[46] CFT assumes the interactions between metal ions and corresponding ligands are electrostatic, and the ligands are considered as point charges.

In this present study, we have mainly discussed the crystal field theory for the octahedral and tetrahedral fields, since almost all cathode materials for LIB consist of the octahedrons and tetrahedrons between TM and O. Figure 2.4.1 shows the crystal field splitting diagrams (CFSDs) of d-orbital for the octahedral (left) and tetrahedral (right) fields. In the octahedral field, e_g level

has higher energy state than that of t_{2g} level due to the coordination of TM-O ligands. By contrast, e_g level has lower energy state than that of t_{2g} level in tetrahedral field. The redox mechanism of transition metals and oxygens is likely to be determined by the stabilization of the crystal field of coordination geometries. For investigating CFSD, occupied and unoccupied electrons at each state are determined by first-principles electronic structure analysis from partial (projected) density of states (PDOS) calculated by DFT.

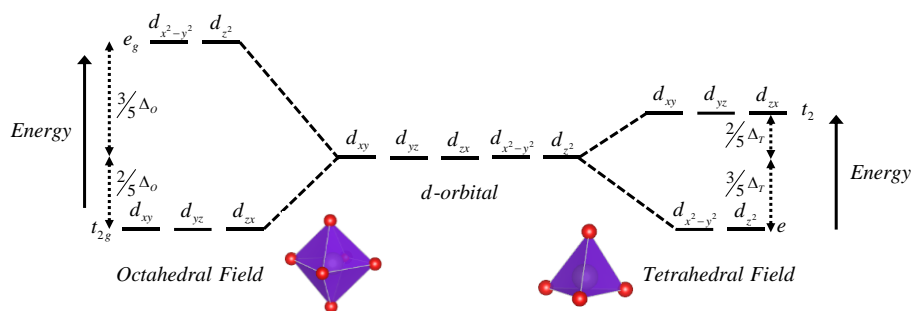


Figure 2.4.1 Crystal field splitting diagrams of d-orbital for the octahedral (left) and tetrahedral (right) fields.

Chapter 3

Combined-phase Transformation Model

As mentioned in **Chapter 1.4**, the electrodes suffering from the combined-phase transformation cannot be probed by conventional models using the mechanism of the one-phase and two-phase reactions. In this chapter, we introduced the development of the combined-phase transformation model, and the definition of the combined-phase enthalpy of formation and free energy functional. Further, we established combined-phase field model using Cahn-Hilliard equation considering various electrochemical states using Butler-Volmer equation. As a numerical example, we applied this model to monoclinic Li_2MnO_3 , which is promising high capacity cathode material for LIB as shown in Figure 3.1.1. It is known that Li_2MnO_3 suffers from severe phase transformation from monoclinic structure, rhombohedral layered structure, to spinel structure,[11] so the combined-phase transformation with three different phases ought to be considered.

3.1 Combined-phase Enthalpy of Formation

Based on the existing enthalpy of formation in Equation (2.2), the modified enthalpy of formation for Li_2MnO_3 with different phases can be

described as follows:[11]

$$\mathbf{H}_{DFT}^m(\mathbf{x}) = \mathbf{E}_{Li_{2x}MnO_3}^{DFT} - \mathbf{x}\mathbf{E}_{(Li_2MnO_3)^{monoclinic}}^{DFT} - (1-\mathbf{x})\mathbf{E}_{(Li_0MnO_3)^{spinel}}^{DFT} \quad (2.9),$$

where \mathbf{H}_{DFT}^m is evaluated in reference to the total energy of monoclinic Li_2MnO_3 for fully-lithiated state and spinel Li_0MnO_3 for fully-delithiated state. This is because the fully-lithiated Li_2MnO_3 is thermodynamically stable as a monoclinic structure, and fully-delithiated Li_0MnO_3 is thermodynamically stable as a spinel structure.[11] The calculated results are shown in Figure 3.1.1a that indicates the spinel $Li_{2x}MnO_3$ is stable from $x = 0.0$ to 0.25 , the layered $Li_{2x}MnO_3$ is stable from $x = 0.25$ to 0.5 , and the monoclinic $Li_{2x}MnO_3$ is stable from $x = 0.5$ to 1.0 . Moreover, 5 ground states can be found on the basis of the modified enthalpy of formation at $x = 0.0$ (spinel), 0.125 (spinel), 0.375 (layered), 0.5 (layered), and 1.0 (monoclinic).

Based on the evaluated ground states from the convex hull analysis of the enthalpy of formation, we predicted their one-phase reaction ($Li_xTM_yO_z$) and two-phase reaction ($xLi_iTM_yO_z + (1-x)Li_0TM_yO_z$) regions from x_i to x_f . As shown in Figure 3.1.1b, from the predicted ground states, the modified enthalpy of formation $\mathbf{H}_{DFT}^{i,f}$ at the corresponding reaction regions can be calculated as follows:[1, 26]

$$\mathbf{H}_{DFT}^{i,f}(\mathbf{x}) = \mathbf{E}_{Li_xTM_yO_z}^{DFT} - \frac{\mathbf{x} - \mathbf{x}_i}{\mathbf{x}_f - \mathbf{x}_i} \mathbf{E}_{Li_{x_f}TM_yO_z}^{DFT} - \frac{\mathbf{x}_f - \mathbf{x}}{\mathbf{x}_f - \mathbf{x}_i} \mathbf{E}_{Li_{x_i}TM_yO_z}^{DFT} \quad (2.10).$$

After parameterization of $\mathbf{H}_{DFT}^{i,f}$ by the double-well function with the enthalpy coefficient ε_i^f at the reaction regions (x_i-x_f), the combined-phase enthalpy of formation \mathbf{H}_{CP} can be determined as follows:[1, 26]

$$\mathbf{H}_{CP}(\mathbf{x}) = \sum_{(x_i-x_f)} \varepsilon_i^f (\mathbf{x} - \mathbf{x}_i)^2 (\mathbf{x}_f - \mathbf{x})^2 \quad (2.11).$$

The theoretical background of the double-well function arises from the Landau-type free energy models. The phase separation of the two-phase

reaction is generated between two stable ground states, which lie between the two potential wells. Therefore, double-well or multi-well functions can be adopted for \mathbf{H}_{CP} with respect to the characteristics of electrodes; however, we employed a simple double-well potential in this study. Furthermore, the particular choice of the double-well function mathematically ensures continuity and smoothness at each initial and final reaction point such that it provides better fits for experimental solubility limits to the electrochemical electrodes.

3.2 Combined-phase Free Energy Functional

To develop the combined-phase enthalpy of formation \mathbf{H}_{CP} to the combined-phase free energy \mathbf{f}_{CP} , we adopted the configurational entropy S_c based on Fermi distribution as follows:[8]

$$S_c(\mathbf{x}) = -k_B \left[\mathbf{x} \ln \mathbf{x} + (1 - \mathbf{x}) \ln (1 - \mathbf{x}) \right] \quad (2.12),$$

where k_B denotes the Boltzmann constant. Therefore, we determined the combined-phase free energy \mathbf{f}_{CP} as follows:[1, 26]

$$\mathbf{f}_{CP}(\mathbf{x}) = \sum_{(x_i - x_f)} \varepsilon_i^f (x - x_i)^2 (x_f - x)^2 + k_B T \left[\mathbf{x} \ln \mathbf{x} + (1 - \mathbf{x}) \ln (1 - \mathbf{x}) \right] \quad (2.13),$$

where T represents absolute temperature.

For constituting electrochemical phase transformation model with mechanical deformation for the combined-phase transformation behaviors, we determined the combined-phase free energy functional \mathbf{G}_{CP} using Cahn-Hilliard energy functional as follows:[1, 26]

$$\mathbf{G}_{CP}(\mathbf{x}) = \int_V \rho_n \left\{ \mathbf{f}_{CP} + \frac{\kappa_i^f}{2} |\nabla \mathbf{x}|^2 + e \Delta \phi \mathbf{x} \right\} + \frac{1}{2} C_{ijkl} \varepsilon_{ij} \varepsilon_{kl} - \bar{\sigma}_{ij} \bar{\varepsilon}_{ij} dV \quad (2.14),$$

where ρ_n represents the number of sites per volume V and κ_i^f the gradient energy coefficient at the reaction region from initial content \mathbf{x}_i to

final content \mathbf{x}_f . For the electrochemical phase transformations, $\Delta\phi$ and e represent the interfacial voltage at the surface and the elementary charge, respectively. As regards mechanical behaviors, C_{ijkl} and ε_{ij} represent the elastic stiffness tensor and elastic strain, respectively. In addition, $\bar{\sigma}_{ij}$ and $\bar{\varepsilon}_{ij}$ denote the homogeneous stress and strain, respectively.

In the diffuse-interface description, the gradient energy coefficient characterizes the energy penalty of the inhomogeneity at the interfaces, which means that κ_i^f is strongly affected by the shape of the double-well potential and the interfacial width. If we consider the interfacial width as the nearest-neighbor distance of the charge carrier in the electrode (characteristic length λ), [47] the interfacial energy γ^i exhibits general relations with the coefficient of the double-well function ε_i^f , characteristic length λ , and gradient energy coefficient κ_i^f as follows: [48]

$$\gamma^i \propto \sqrt{\kappa_i^f \varepsilon_i^f}, \quad \gamma \propto \lambda \varepsilon_i^f \quad (2.15)$$

From these relations and dimensional approaches, [47, 49] we can determine κ_i^f at each reaction interface, corresponding to the coefficient of double-well function ε_i^f as follows:

$$\kappa_i^f = \frac{\mathbf{n}_d}{3} \lambda^2 \varepsilon_i^f \quad (2.16)$$

where \mathbf{n}_d denotes the number of possible diffusion directions of the charge carrier.

3.3 Electrochemical Phase Transformation Model

In essence, we utilize the electrochemical phase transformation kinetics reported by Bai et al. [13] According to the transition state theory for

concentrated solutions, the Butler–Volmer equation can be described as follows:

$$\mathbf{J} = \mathbf{J}_0 \left[e^{-\alpha \frac{e\eta}{k_B T}} - e^{(1-\alpha) \frac{e\eta}{k_B T}} \right] \quad (2.17),$$

where α represents the electron-transfer symmetry factor and η the overpotential ($\eta = \Delta\phi - \Delta\phi_{eq}$). We next define $\Delta\phi_{eq}$ as the Nernst equilibrium voltage and the exchange current density \mathbf{J}_0 as

$$\mathbf{J}_0 = \frac{e a_+^{1-\alpha} a^- \alpha}{A_S \tau_0} (1 - x) \quad (2.18),$$

where a_+ denotes the local activity of Li^+ in the electrolyte, A_S the reacting area, and τ_0 the mean time for a reaction step. The local activity of Li a is related to the chemical potential μ as follows:

$$\mu = \mu_{CP} - \kappa_i^f \nabla^2 x = k_B T \ln a \quad (2.19),$$

where μ_{CP} denotes the combined-phase chemical potential obtained from the combined-phase free energy f_{CP} as follows:

$$\mu_{CP} = \frac{\partial f_{CP}}{\partial x} \quad (2.20).$$

To reformulate dimensionless forms, we scale the voltage to the thermal voltage $k_B T/e$, length to the characteristic length λ , time to the mean time of diffusion Dt/λ^2 by means of the diffusion coefficient D , and the exchange current density to $\mathbf{J}_0 A_S \tau_0/e$. Based on these parameters, the dimensionless Butler–Volmer equation can be represented in terms of concentration x as follows:

$$\hat{\mathbf{J}} = \frac{\partial x}{\partial \hat{t}} = \hat{\mathbf{J}}_0 \left[e^{-\alpha \hat{\eta}} - e^{(1-\alpha) \hat{\eta}} \right] \quad (2.21),$$

and the dimensionless total current $\hat{\mathbf{I}}$ can be defined as an integral over the dimensionless area \hat{A} of the active facet as follows:

$$\hat{\mathbf{I}} = \int \frac{\partial \mathbf{x}}{\partial \hat{t}} d\hat{A} \quad (2.22).$$

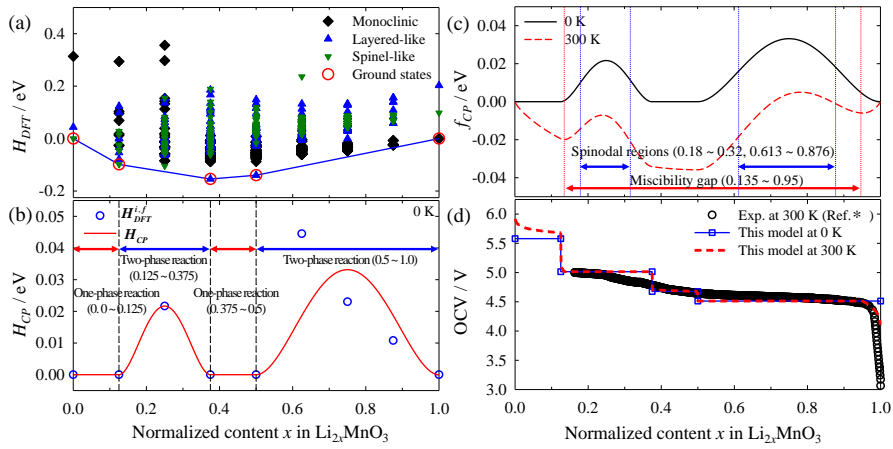


Figure 3.1.1 Combined-phase transformation behaviors of monoclinic Li_2MnO_3 cathode material with respect to the normalized Li content x in $\text{Li}_{2x}\text{MnO}_3$. (a) Enthalpy of formation H_{DFT} of all possible configurations for monoclinic (black diamonds), layered-like (blue triangles), and spinel-like (green inverse triangles) phases and the ground states (red circles). (b) Combined-phase enthalpy of formation H_{CP} (red line) with $H_{DFT}^{i,f}$ (blue circles). (c) Combined-phase free energy f_{CP} at 0 K (black solid line) and 300 K (red dashed line). (d) Predicted voltages based on the combined-phase transformation model at 0 K (blue squares and line) and 300 K (red dashed line) with experimental open-circuit voltage reproduced from Rana et al.*[50]

Chapter 4

Mechanical Deformation and Crack Generation

The above electrochemical phase transformation affects the mechanical behavior such as stress generation and volume expansion, and vice versa. In order to solve mechano-electrochemical phase transformation and mechanical deformation from the electrochemical phase transformation, the mechanical equilibrium was investigated.

4.1 Mechanical Equilibrium

For the combined-phase free energy functional represented in Equation (2.14), $\bar{\sigma}_{ij}$ and $\bar{\varepsilon}_{ij}$ result from the external pressure in the electrolyte, which can be generally neglected at atmospheric pressure for solids.[15, 51] In particular, the elastic strain ε_{ij} can be described by the total strain ε_{ij}^t generated by compositional inhomogeneity, and inelastic strain arising from lattice misfit ε_{ij}^m as follows:

$$\varepsilon_{ij} = \bar{\varepsilon}_{ij} + \varepsilon_{ij}^t - \varepsilon_{ij}^m (1 - \mathbf{x}) \quad (2.23).$$

The inelastic strain is assumed to vary with the composition (Vegard's law)

between the undeformed state and the deformed state. Finally, the mechanical deformation is determined by the stress equilibrium as:

$$\sigma_{ij,j} = 0 \quad (2.24).$$

From Equation (2.23) and the negligible external pressure, the stress equilibrium in Equation (2.24) further formulates as follows:

$$\left(C_{ijkl} \left(\varepsilon_{ij}^t - \varepsilon_{ij}^m (1 - \mathbf{x}) \right) \right)_{,j} = 0 \quad (2.25).$$

4.2 Phase Field Crack Model

Based on the above-mentioned electrochemical combined-phase transformation model with mechanical deformations, we developed the phase field crack model considering the combined-phase transformation by introducing the phase field crack model for brittle fracture developed by Miehe et al.[52] and Borden et al.[53]

In order to describe the crack topology, we introduced the crack phase field $c(\mathbf{r})$ as shown in Figure 4.2.1. The unbroken and broken states are denoted by $c(\mathbf{r}) = 1.0$ and 0.0 , respectively. Figure 4.2.1a visualizes the sharp crack topology with discontinuity. Figure 4.2.1b represents the diffusive crack topology that can be numerically tracked, which can be approximate by the exponential function as follows:

$$c(\mathbf{r}) = 1 - \exp\left(-\frac{|\mathbf{r}|}{2l_0}\right) \quad (2.26),$$

where l_0 represents the length scale parameter and the crack phase field $c(\mathbf{r})$ smears out the crack. Equation (2.26) is derived from the homogeneous differential equation

$$\left(c(\mathbf{r}) - 1 \right) - 4l_0^2 c''(\mathbf{r}) = 0 \quad (2.27).$$

The above differential equation is the Euler equation of the variational principle, which can be described by the functional $\mathbf{I}(c(\mathbf{r}))$ as follows:

$$\mathbf{I}(\mathbf{c}(\mathbf{r})) = \frac{1}{2} \int_B \left\{ (\mathbf{c}(\mathbf{r}) - 1)^2 + 4l_0^2 \mathbf{c}'(\mathbf{r})^2 \right\} dV \quad (2.28),$$

where B is the domain of the crack phase field and V the volume. Based on the solution of the functional $\mathbf{I}(\mathbf{c}(\mathbf{r}))$ in Equation (2.26), the functional $\mathbf{I}(\mathbf{c}(\mathbf{r}))$ can be represented by the crack surface functional $\Gamma(\mathbf{c}(\mathbf{r}))$ and the length scale parameter l_0 as follows:

$$\mathbf{I}(\mathbf{c}(\mathbf{r})) = 2l_0 \Gamma(\mathbf{c}(\mathbf{r})) \quad (2.29).$$

Consequently, the crack surface functional $\Gamma(\mathbf{c}(\mathbf{r}))$ can be described as follows:

$$\Gamma(\mathbf{c}(\mathbf{r})) = \frac{1}{2l_0} \mathbf{I}(\mathbf{c}(\mathbf{r})) = \frac{1}{4l_0} \int_B \left\{ (\mathbf{c}(\mathbf{r}) - 1)^2 + 4l_0^2 \mathbf{c}'(\mathbf{r})^2 \right\} dV \quad (2.30),$$

and by extending the one-dimensional description to multi-dimensional manner, the crack surface density function $\gamma(\mathbf{c}, \nabla \mathbf{c})$ can be defined by the crack phase field and its spatial gradient as follows:

$$\gamma(\mathbf{c}, \nabla \mathbf{c}) = \frac{1}{4l_0} (\mathbf{c} - 1)^2 + l_0 |\nabla \mathbf{c}|^2 \quad (2.31).$$

Using the diffusive crack topology, we determined the combined-phase free energy functional with the crack phase field \mathbf{G}_{CP}^C by including the phase field crack formulation to the combined-phase free energy functional \mathbf{G}_{CP} as follows:

$$\mathbf{G}_{CP}^C = \int_V \rho_n \left\{ f_{CP} + \frac{\kappa_i^f}{2} |\nabla \mathbf{x}|^2 + e \Delta \phi \mathbf{x} \right\} + \psi_e - \bar{\sigma}_{ij} \bar{\epsilon}_{ij} + \mathbf{g}_c \gamma dV \quad (2.32),$$

where ψ_e denotes the elastic energy with the crack phase field and \mathbf{g}_c represents the critical fracture energy density. In accordance with Griffith's fracture theory, \mathbf{g}_c is the energy required to generate a unit area of fracture surface, which is generally referred to as the critical energy release rate or the

fracture toughness. To model the energy dissipation in the failure zone, we utilized the elastic energy introduced by Miehe et al.[52] as follows:

$$\psi_e = \left[(1-k)\mathbf{c}^2 + k \right] \psi_e^+ + \psi_e^- \quad (2.33),$$

where the model parameter k is to avoid ill-posedness by taking an infinitesimal value, and ψ_e^+ and ψ_e^- represent the positive and negative components of the elastic energy ψ_e , respectively. These are defined as

$$\begin{cases} \psi_e^+ = \langle \psi_e \rangle \\ \psi_e^- = \psi_e - \langle \psi_e \rangle \end{cases} \quad (2.34),$$

where

$$\langle \psi_e \rangle = \begin{cases} \psi_e & \psi_e > 0, \\ 0 & \psi_e \leq 0. \end{cases} \quad (2.35).$$

As a consequence, the evolution of the crack phase field \mathbf{c} can be determined by the variational principle of \mathbf{G}_{CP}^C as follows:

$$\frac{\delta \mathbf{G}_{CP}^C}{\delta \mathbf{c}} = 0 \quad (2.36),$$

Using the free energy functional of Equation (2.32) for the variational principle in Equation (2.36), the evolution equation can be described by

$$4l_0(1-k)\mathbf{c}\psi_e^+ + \mathbf{g}_c(\mathbf{c}-1) - 4\mathbf{g}_c l_0^2 \nabla^2 \mathbf{c} = 0 \quad (2.37),$$

From the rearrangement of Equation (2.37), the governing equation can be derived by

$$\left(\frac{4l_0(1-k)\psi_e^+}{\mathbf{g}_c} + 1 \right) \mathbf{c} - 4l_0^2 \nabla^2 \mathbf{c} = 1 \quad (2.38).$$

As a fundamental physical quantity, the above-determined multiscale-based model has a strong advantage in that it considers CP reactions with multiple phases *via* calculation of \mathbf{f}_{CP} , \mathbf{G}_{CP} , \mathbf{G}_{CP}^C , and \mathbf{g}_c through

defining ε_i^f and κ_i^f at different phase transformations, respectively; this means that each mesoscale phase behavior including mechanical deformation and crack generation can be described differently based on atomic-scale first-principles calculations.

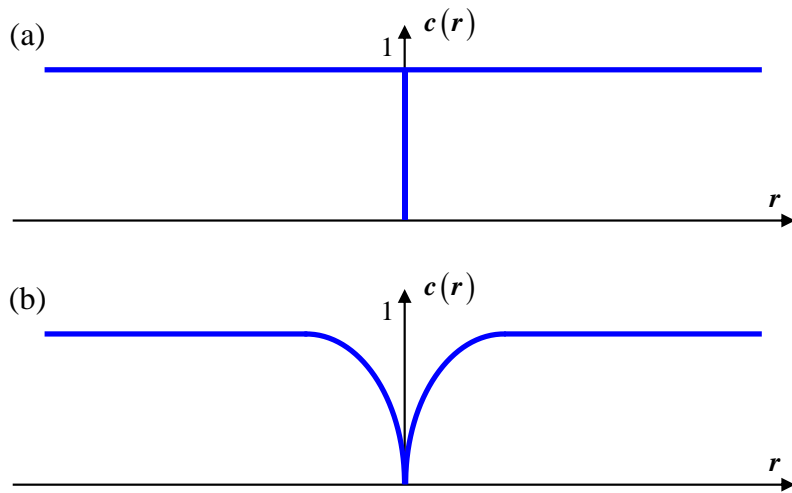


Figure 4.2.1 (a) Sharp and (b) diffusive crack topology at $x = 0.0$. Diffusive crack modeled with the length scale $2l_0$ in terms of the crack phase field $c(r)$.

Chapter 5

Experimental Details

In this study, we performed the electrochemical experiments including the synthesis of inorganic materials, the identification of the crystal structure, the characterization of the chemical and structural changes in order to validate and realize the theoretical investigations and designs. In this dissertation, we described the general procedure of our experiments, so we recommend seeing our published works.[11, 20-25, 37-39]

5.1 Synthesis of Materials

Battery electrodes used in this work was synthesized through solid-state methods and sol-gel methods. Stoichiometric amounts of precursors were dissolved in deionized water under continuous stirring for several hours at room temperature. In case of the sol-gel methods, additionally a colloidal solution was added in the dissolved solution. After drying, the collected powder was sintered.

5.2 Materials Characterization

The as-synthesized powder was characterized using an X-ray diffractometer (XRD, Empyrean PANalytical) equipped with Cu-K α radiation ($\lambda = 1.5418 \text{ \AA}$) in the 2θ range of $10\text{--}80^\circ$. Rietveld refinements of the collected XRD patterns were carried out using HighScore Plus software (PANalytical). The morphology, particle size, and elemental distribution were examined using a field-emission scanning electron microscopy (FESEM, JEOL JSM-7000F) coupled with energy-dispersive X-ray spectroscopy (EDS). A scanning transmission electron microscopy (STEM, JEOL ARM-200F) was employed to confirm the microstructure and atomic arrangement. Furthermore, high-resolution transmission electron microscopy (HRTEM, JEOL ARM-200F) coupled with EDS were used to examine the distribution of elements and the corresponding elemental ratios of the prepared powders. The chemical states of the powder were characterized by X-ray photoelectron spectroscopy (XPS) using a sigma probe spectrometer (Thermo Scientific). The chemical composition of the elements was confirmed by inductively coupled plasma mass spectroscopy (ICP-MS, Bruker Aurora M90). Thermogravimetric analysis (TGA) was performed using PerkinElmer instrument under a gas flow. Particle size analysis (PSA) was conducted by a particle size analyzer (PSA, Microtrac S3500).

5.3 Electrochemical Measurements

For electrochemical experiments, the electrode was prepared using a slurry containing as-prepared powder, a conducting agent, and a polyvinylidene fluoride (PVDF) binder dispersed in an *N*-methyl-2-pyrrolidone (NMP) solution. After the slurry was coated on a piece of Al foil as a current collector, the electrode was dried to evaporate NMP, followed by further drying overnight under vacuum. CR2032 coin-type half cells were

assembled in a glove box or a dry room, using Li metal as the counter and reference electrode. A porous polyethylene (PE) membrane was utilized as a separator; 1.3 M or 1.15 M LiPF_6 ethylene carbonate (EC)/ethylmethyl carbonate (EMC) in a 3:7 volume ratio was applied as the electrolyte (PANAX ETEC Co. Ltd.) The loading amount of active materials and electrode density were maintained. The test cells were galvanostatically charged and discharged using a MACCOR 4300K galvanostat.

Chapter 6

Mechanics-based Design and Realization

In this chapter, we introduced the cathodes materials designed by the mechanics-based multiscale methodology described in Chapter 2-5, and further we realized the designed materials by electrochemical experiments. Before entering this chapter, we would like to clarify that the materials introduced at each section of this chapter are based on our published papers.[1, 11, 20-26]

6.1 Phase Transformation of Monoclinic Li_2MnO_3 [11]

As an end member of Li-rich oxides for high-energy cathode materials in Li-ion batteries (LIBs), Li_2MnO_3 cathode occupies an important territory in the field of LIB cathodes, but it has critical drawbacks of cyclic degradation and voltage drop related to severe phase transformation. To resolve these problems, it is necessary to identify the origins and mechanism of phase transformation in Li_2MnO_3 . In this section, the phase transformation of bulk Li_2MnO_3 is investigated by thermodynamic and kinetic approaches based on first-principles calculations and validated by experiments. Using the

calculated thermodynamic energies, the most stable structure is determined as a function of Li extraction for $\text{Li}_{2-x}\text{MnO}_3$: monoclinic ($x = 0.0 - 0.75$), layered-like ($x = 1.0 - 1.25$), and spinel-like ($x = 1.5 - 2.0$) structures. The phase transformation becomes kinetically possible for $\text{Li}_{2-x}\text{MnO}_3$ ($x > 1.0$). Atomic scale origins and mechanism of phase transformation are elucidated by the thermodynamically stable and kinetically movable tetrahedral coordination of Mn^{4+} in transition state. These theoretical observations are validated by *ex-situ* X-ray photoelectron spectroscopy combined with electrochemical experiments for $\text{Li}_{2-x}\text{MnO}_3$ with various Li content upon cycling. The mechanistic understanding from theoretical calculations and experimental observations is expected to provide a fundamental solution and guidelines for improving the electrochemical performance of Li-rich oxides and, by extension, the battery performance.

For the theoretical studies, we modelled monoclinic Li_2MnO_3 (space group: $C2/m$) for the atomic scale calculation as described in Figure 6.1.1a. The lattice parameters of this atomic model were calculated to be $a = 5.0091$, $b = 8.6623$, $c = 5.0956 \text{ \AA}$, and $\beta = 109.46^\circ$. As shown in Figure 6.1.1a, the $C2/m$ structure consists of LiMn_2 layers containing Li and Mn at 2b and 4g sites, respectively, and Li layers in which Li is located at 2c and 4h sites in terms of the Wyckoff position.

To investigate the kinetics of the phase transformation of monoclinic Li_2MnO_3 , we proposed three possible migration paths for Mn in the given structure (Figure 6.1.1a): Path-i (4g site \rightarrow 2b site), Path-ii (4g site \rightarrow 4h site), and Path-iii (4h site \rightarrow 2b site). By following these three different paths, the proposed Mn migration would lead to the phase transformation of Li_2MnO_3 . First, Path-i represents a direct densification of Mn within the LiMn_2 layer, which is characteristic of the phase transformation to the densified layered-like structure (denoted as LA-like structure hereafter) in

Figure 6.1.1b. Second, Path-ii indicates the Mn migration from the LiMn_2 layer to the Li layer, which leads to the phase transformation to the defected spinel-like structure (denoted as SPI-like structure hereafter) in Figure 6.1.1c. Finally, a detoured densification of Mn in the LiMn_2 layer could also take place by way of a sequential Mn migration through Path-ii and then Path-iii.

The thermodynamic stability of these three different structures was investigated by obtaining the enthalpy of formation with inverse Li content x in $\text{Li}_{2-x}\text{MnO}_3$ according to Equation 2.2. The enthalpy of formation was calculated based on the relative structural stabilities of monoclinic structure ($x = 0$) and a SPI-like structure ($x = 2$). Figure 6.1.2a shows the enthalpies of formation for all possible configurations of $\text{Li}_{2-x}\text{MnO}_3$ with varying Li content. It should be noted that the comparison shows the structural stability of $\text{Li}_{2-x}\text{MnO}_3$ is strongly affected by the Li content. The monoclinic structure (black circles) has lower enthalpies of formation than those of the other structures from $x = 0$ to 0.75, while the enthalpies of formation of the LA-like structure (red inverse triangles) are lowest in the range from $x = 1.0$ to 1.25. From $x = 1.5$ to 2.0, the SPI-like structure (blue triangles) shows the lowest enthalpies of formation. From a thermodynamic viewpoint, it can be inferred from these ranges of enthalpies that the monoclinic structure of initial Li_2MnO_3 is stably maintained in the range of $x = 0$ to 0.75. When more Li^+ is extracted, the LA-like structure ($x = 1.0$ to 1.25) and SPI-like structure ($x = 1.5$ to 2.0) become more thermodynamically stable.

We will now turn our attention to another key factor of phase transformation, the kinetic energy barrier which can determine how fast it can proceed under the given temperature condition. Figure 6.1.2b shows the summary of the migration barriers of the three proposed Mn migration paths and detailed description of Mn migration barriers for each path. As shown in Figure 6.1.2b, Path-i has much higher maximum migration barriers than those of Path-ii and Path-iii. The calculated migration barriers are about 5 eV at $x =$

0.25 to 0.5, and they decrease to 2.5 eV with further Li^+ extraction ($x = 1.25$). However, the reduced barrier is still higher than that of Li^+ (0.6 – 1.0 eV) in the Li_2MnO_3 structure,[54] which means that Mn migration would not be possible through Path-i. On the other hand, the migration barriers of Path-ii and Path-iii were higher than 1.0 eV ($x < 1.0$), but the barriers gradually decreased to around 1.0 eV ($x = 1.0$) and 0.5 eV ($x = 1.25$), respectively. Therefore, Mn migrations through Path-ii and Path-iii are likely once a certain amount of Li has been extracted from the structure ($x > 1.0$). We note that the most favorable Mn migration path for the formation of the SPI-like structure is Path-ii, and the transformation to the LA-like structure possibly occurs along Path-ii and then Path-iii, but not along Path-i. Our finding is consistent with *ex-situ* TEM results reported by Wang et al.[55] Thus, we believe that our simulation approaches considering both thermodynamic and kinetic manners can describe more realistic phase transformation mechanism.

The electronic structures of intermediate states on Mn migration paths identified in Figure 6.1.2 were examined by analyzing behaviors of electronic states through crystal field theory to understand origins and mechanism of phase transformation. Figure 6.1.3 shows the atomic models of the initial state ($\text{Li}_{2-x}\text{MnO}_3$, $x = 1.25$) before Mn migration and an intermediate state ($\text{Li}_{2-x}\text{MnO}_3$, $x = 1.25$) on each migration path as well as the calculated partial density of states (PDOS) for each model. Figure 6.1.3a illustrates the Mn ion located at the octahedral site of monoclinic Li_2MnO_3 at the initial state and the corresponding PDOS. We observe two interesting features: there exists a large density of the O p-orbital states around 0 to 1.0 eV from Fermi level (E_F), while the Mn d-orbital is not significant. This PDOS at E_F suggests that an electron could be extracted from the O ion rather than Mn ion, when Li is extracted from the host structure. The oxygen environment would become more unstable as a result of the loss of electrons (i.e., oxidation) from the O ion.[56] Inspired by this finding, we examined the oxidation behaviors of Mn

and O ions of all of the proposed structures with various Li content. The O ion is more likely to be oxidized as more Li is extracted. The LA-like and SPI-like structures show oxidation behavior similar to that of the monoclinic structure because the Mn ion finally occupies the octahedral sites in both structures.

Figure 6.1.3b describes an atomic model of the intermediate state of $\text{Li}_{2-x}\text{MnO}_3$ on Path-i, in which Mn is located at the octahedral site because the confined space surrounded by close-packed O does not allow the Mn migration to the tetrahedral site. As evidenced by the calculated PDOS (Figure 6.1.3b), a large amount of electron transfer from O ions was observed without a noticeable oxidation of Mn ions, which is not much different from the initial state shown in Figure 6.1.3a. On the other hand, Figure 6.1.3c and 6.1.3d represents atomic models for Mn occupying the tetrahedral site in intermediate states of $\text{Li}_{2-x}\text{MnO}_3$ on Path-ii and Path-iii. More importantly, the migrating Mn ions could form a tetrahedral site between LiMn_2 layers because relatively wider space could be attained by Li extraction. According to the PDOS in these cases, relatively less oxidation of the O ion and more oxidation of the Mn ion were found. For a quantitative comparison of the PDOS results, the integration of occupied states of the Mn d-orbital for each case is plotted in Figure 6.1.3e. The initial and intermediate states on Path-i show electrons of occupied states that are about 0.35 e higher than those of the intermediate states on Path-ii and Path-iii, which clearly explains that the Mn ion is more oxidized when located in the tetrahedral site, leading to less oxidation of the O ion. By reducing the electron transfer from O ions, the oxygen environment could be more stable with a decrease in the migration barrier, which facilitates the phase transformation.

The observed oxidation behavior of Mn and O ions can be clearly explained by crystal field theory as illustrated in Figure 6.1.3f. In crystal field theory, five d-orbital states of an Mn atom split according to its

coordination geometry. The charge state of Mn^{4+} has three electrons in the d-orbital and three spin-up electrons occupy t_{2g} state according to the electronic configuration of Mn^{4+} in the octahedral site, as shown in Figure 6.1.3f (left). In principle, extraction of an electron stably occupying the t_{2g} state of Mn would be difficult, resulting in electron transfer from the O ion for Mn at the octahedral site during Li extraction. In contrast, the electronic configuration of Mn^{4+} is different at the tetrahedral site, in which two spin-up electrons are occupied in the e state and one spin-up electron is occupied in the t_2 state, as shown in Figure 6.1.3f (right). For this reason, one electron occupying the t_2 state can be easily withdrawn, allowing the temporary formation of Mn^{5+} -like state. Accordingly, the Mn^{4+} ion at the tetrahedral site can be further oxidized by suppressing and compensating the electron transfer from surrounding O ions, which makes the oxygen environment more stable, resulting in a decrease in the migration barrier. In summary, electron transfer from the O inevitably occurs in the Li_2MnO_3 structure upon delithiation, and it can facilitate the Mn migration *via* the tetrahedral site rather than the octahedral site. This electron transfer from O ions is thus responsible for the phase transformation from monoclinic Li_2MnO_3 to LA-like and SPI-like structures through Path-ii and Path-iii rather than Path-i.

For experimental validation of the theoretical findings, single-phase Li_2MnO_3 was synthesized by conventional solid-state reaction and characterized using various structural analysis techniques. Figure 6.1.4a shows a powder XRD pattern of as-synthesized Li_2MnO_3 at 450 °C. All reflections are in good agreement with the reference and have been indexed to the monoclinic Li_2MnO_3 structure of $C2/m$ space group (JCPDS 84-1634). A broad peak was detected at low Bragg angles between 20 ° and 22.5 °, which is a general characteristic of Li_2MnO_3 synthesized at low-temperature. The morphology and particle size of Li_2MnO_3 were also characterized with a FESEM at different magnifications. As shown in Figure 6.1.4b, spherical

Li_2MnO_3 nano-particles agglomerated to form secondary particles with a size of around 7 – 8 μm . A magnified FESEM image (Figure 6.1.4c) indicates that the size of the primary particles was around 100 – 150 nm.

For further inspection of the microstructure of Li_2MnO_3 , STEM analysis with DFT calculation was carried out, as shown in Figure 6.1.5. The STEM image clearly shows well-arranged dots representing atoms in the Li_2MnO_3 crystal lattice (Figure 6.1.5a), which indicates that Li_2MnO_3 synthesized in this work has a fine microstructure without any defect or dislocation. From the magnified STEM image (Figure 6.1.5b) and the corresponding FFT result with a zone axis of [010] (Figure 6.1.5c), we confirmed the directions of the (001), (200), and (20-2) planes and angles between the planes. In addition, the d -spacing in the atomic lattice was measured to be 4.9 \AA between the (001) planes, and 2.4 \AA between the (200) planes. Our observations on the structure of as-synthesized Li_2MnO_3 are in good agreement with the atomic model used for the DFT calculation shown in Figure 6.1.5d. Therefore, we have confirmed that the synthesized Li_2MnO_3 is suitable for experimental validation of our theoretical observations.

Further, we investigate chemical states of Li_2MnO_3 during Li^+ extraction using XPS as described in Figure 6.1.6. We focused on the change in the valence state of Mn in Li_2MnO_3 during Li^+ extraction. The Mn $2p_{3/2}$ and Mn $2p_{1/2}$ spectra were carefully fitted to the C 1s spectra at 284.8 eV as shown in Figure 6.1.6. Several peaks corresponding to Mn^{4+} ($2p_{3/2}$: ~642.7 eV, $2p_{1/2}$: ~654.1 eV), Mn^{3+} ($2p_{3/2}$: ~641.4 eV, $2p_{1/2}$: ~652.7 eV), and Mn^{2+} ($2p_{3/2}$: ~640.4 eV, $2p_{1/2}$: ~651.3 eV) were obvious in the spectra collected from different state of charge (SOC) states. Before charging ($x = 0$), a dominant peak was found at ~642.7 eV corresponding to Mn^{4+} , but the Mn^{4+} peak gradually decreased and the Mn^{3+} peak remarkably increased as more Li^+ was extracted (x is increased). The meaning of increasing Mn^{3+} is a structural evolution of Li_2MnO_3 toward LA- and SPI-like structures mainly configured

with Mn^{3+} . In other words, *ex-situ* XPS results represent the phase formation of Li_2MnO_3 into LA- and SPI-like structures.

Figure 6.1.7a shows the galvanostatic charge-discharge profiles of Li_2MnO_3 at selected cycles. It is well recognized that the charge profile of Li_2MnO_3 was changed after the first cycle due to undesirable phase transformation. The corresponding dQ/dV profiles are presented in Figure 6.1.7b. The first charge capacity was estimated to be about 225 mAh g^{-1} (Figure 6.1.7a), indicating that around 49 % ($x = 1.0$) of Li was extracted from the $\text{Li}_{2-x}\text{MnO}_3$ structure. The corresponding dQ/dV curves for the first and sixth cycles show a clear peak between 3.0 – 4.0 V vs. Li/Li^+ , which is mainly attributed to the layered Li_xMnO_2 (Figure 6.1.7b).[57-59] However, the peak disappeared at the twelfth cycle, which might have been caused by a gradual decrease in residual Li content in the structure associated with irreversible reactions. Based on our theoretical results, we estimated that around 50 – 75 % ($x = 1.0 - 1.5$) of Li was extracted from Li_2MnO_3 in the first and sixth cycles and over 75 % ($x = 1.5$) of Li was extracted in the twelfth cycle. For a convincing electrochemical validation, the residual Li content in Li_2MnO_3 in the i -th cycle under the CC charging mode was calculated according to Lim et al.[11] As shown in Figure 6.1.7c, the residual Li content was calculated to be slightly above 50 % ($x = 1.0$) in the first cycle and it gradually decreased because of irreversible capacity induced by the phase transformation, Mn dissolution, O evolution, and so forth. From the first to seventh cycle, the residual Li content was estimated to decrease from approximately 50 % to 25 % ($x = 1.0$ to 1.5) of the total capacity, which is equivalent to the Li content that permits the formation of a densified layered (LA-like) structure in our theoretical calculation. After the eighth cycle, the residual Li content was calculated to be below 25 % ($x = 1.5$), at which the formation of a densified layered (LA-like) structure is not allowed according to the theoretical calculation. Figure 6.1.7d shows the peaks related to the electrochemical

reaction of the layered Li_xMnO_2 between 3.0 – 4.0 V vs. Li/Li^+ until the seventh cycle, where the residual Li content is around 25 % ($x = 1.5$) from the first cycle while the peak was not visible in the ninth cycle owing to a decrease in residual Li content of the structure. These observations are in good agreement with our theoretical results for the structural evolution of Li_2MnO_3 with increasing Li extraction as shown in Figure 6.1.2. Therefore, our theoretical findings that the phase transformation of Li_2MnO_3 is closely related to Li content are validated by our experimental observations on electrochemical reactions associated with the layered Li_xMnO_2 during cycles.

On the basis of this study, in conclusion, it is expected that the phase transformation could be suppressed by modifying Li_2MnO_3 such that Mn could not easily migrate from transition metal layer to Li layer. Such modification could be accomplished by making Mn-migrated structure thermodynamically unstable or by increasing kinetic barriers of migration *via* tetrahedral site. There are three possible approaches on bulk modification as follows:

(1) Replacing O ions with anions that remove fewer electrons from Mn such as F. This could make Mn obtain more electrons and electron transfer from O ions could be avoided, which makes the kinetic barriers increase.

(2) Doping other transition metals which could be oxidized more than 5^+ . Such doping could increase redox reactions of the transitional metals (including Mn) and decrease the amount of electrons transferred from O ions in charging process, which makes the kinetic barriers increase.

(3) Substituting Li in Li layer with other (transition) metals, which means building pillars with the metals. Since oxidation states of most metals are larger than Li, less oxidized Mn around the pillar metal atoms could be more oxidized and oxidation of O ions could be avoided. Additionally, Mn could not easily migrate to Li layer due to strong coulomb repulsion by the

substituted metal cations. This interaction would make final structure after Mn migration thermodynamically unstable, and kinetic barriers of migration would also increase.

Finally, not only these three possible approaches to suppress phase transformation of Li_2MnO_3 for mitigating cyclic degradation would be promising suggestions for further studies, but also it is expected that improved Li-rich oxides based on Li_2MnO_3 could be designed with a material data map made up by the understandings of the phase transformation studied in this work.

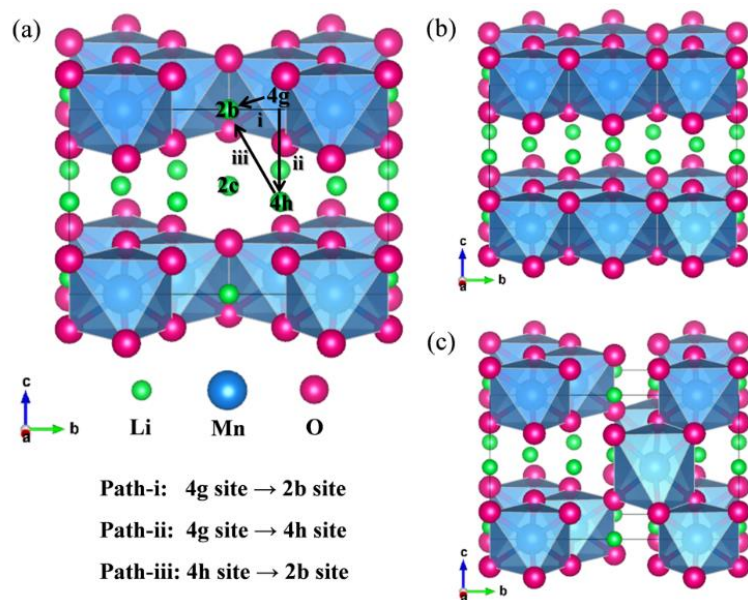


Figure 6.1.1 Atomic model of (a) monoclinic Li_2MnO_3 structure and possible Mn migration paths. Path-i represents the migration of Mn in 4g site to 2b site of Li, Path-ii describes the migration of Mn in 4g site to 4h site of Li, and Path-iii shows the migration of Mn in 4h site to 2b site of Li after the migration following Path-ii. Atomic models of (b) densified layered-like (LA-like) structure, where Mn is located in 2b Li site, and (c) defected spinel-like (SPI-like) structure, where Mn is located in 4h Li site.

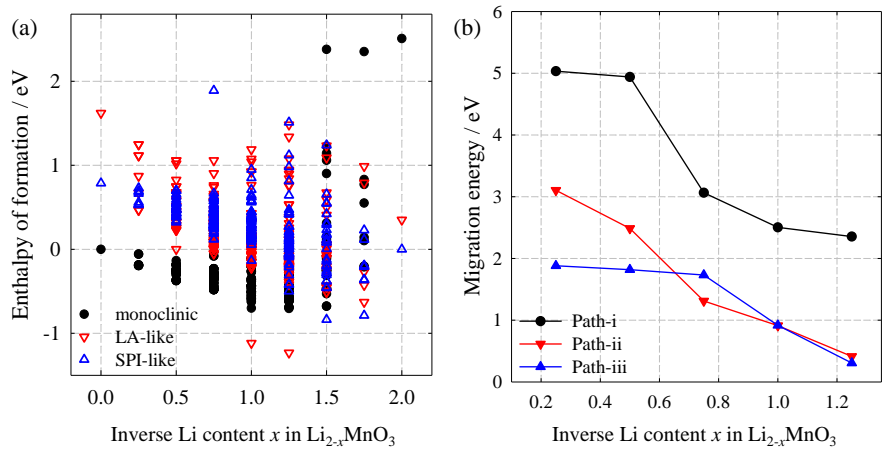


Figure 6.1.2 (a) Enthalpies of formation for three different structures with respect to the inverse Li content x in $\text{Li}_{2-x}\text{MnO}_3$. (b) Enthalpies of formation of ground states.

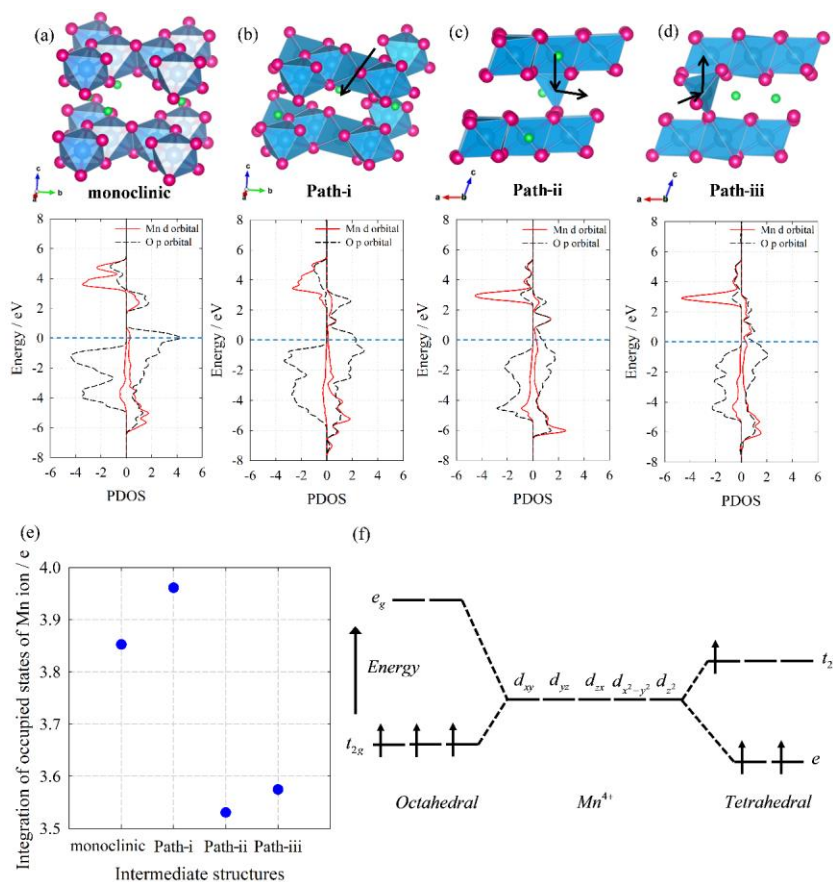


Figure 6.1.3 (a) Atomic model of monoclinic Li_2MnO_3 structure and partial density of states (PDOS) for d-orbital of Mn ion in 4g site and p-orbital of surrounding O ions at $x = 1.25$. Atomic models of intermediate structures of (b) Path-i, (c) Path-ii, and (d) Path-iii at $x = 1.25$, and their PDOS for d-orbital of migrating Mn ion and p-orbital of surrounding O ions in intermediate structures of migration Path-i, Path-ii, and Path-iii. Fermi level is 0.0 eV (blue-dotted line). (e) Integration of occupied states of Mn ion of the monoclinic Li_2MnO_3 structure and three different intermediate structures. (f) Crystal field splitting diagram of Mn^{4+} ion located in octahedral and tetrahedral sites.

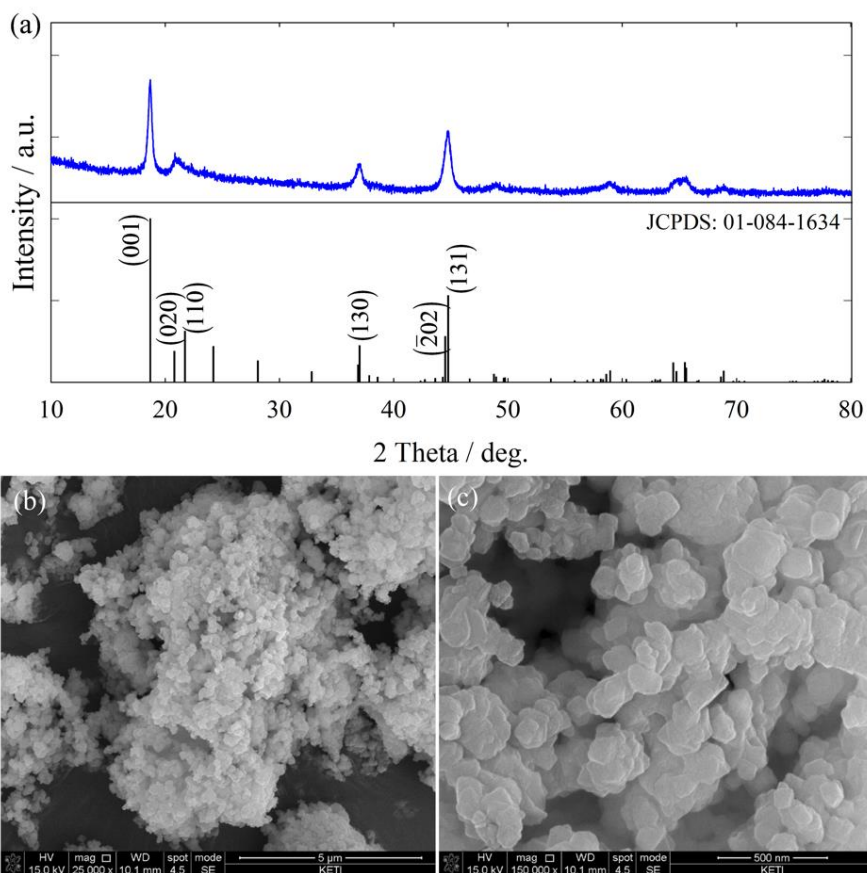


Figure 6.1.4 (a) Powder X-ray diffraction (XRD) pattern of synthesized Li_2MnO_3 powder with a reference (JCPDS 84-1634). Field-emission scanning electron microscope (FESEM) images of the Li_2MnO_3 at (b) low magnification and (c) high magnification.

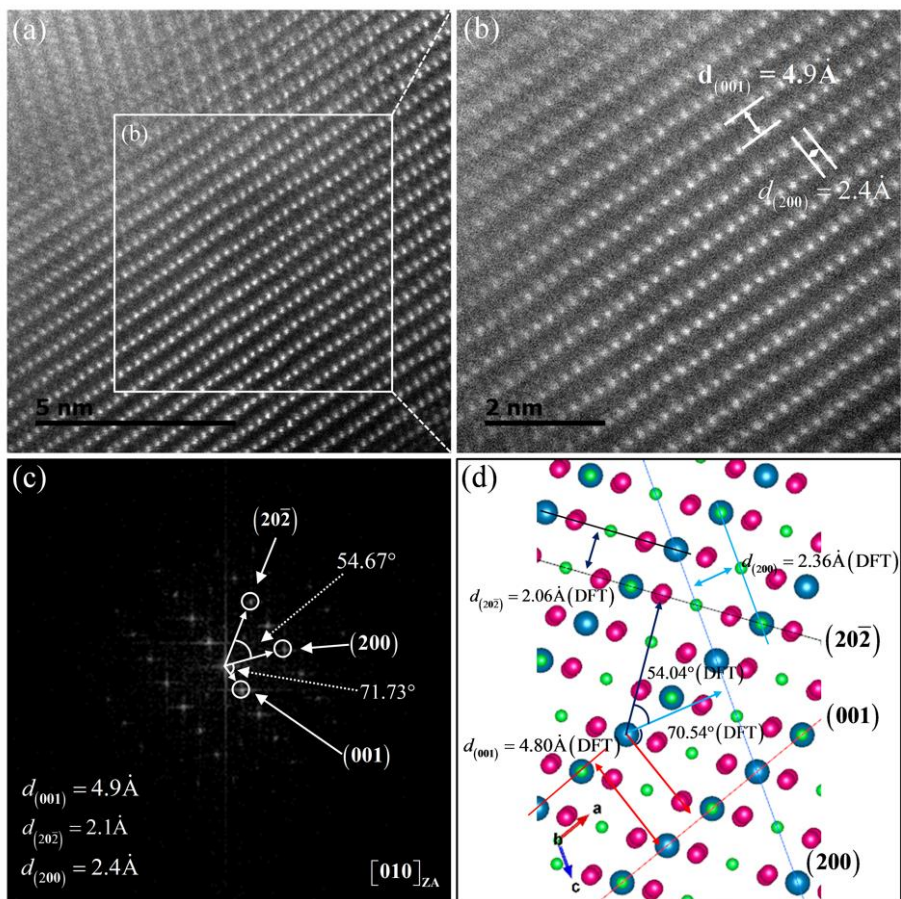


Figure 6.1.5 (a, b) STEM images of the Li_2MnO_3 at (a) low magnification and at (b) high magnification, which is a magnified view of panel in (a). (c) FFT image of (b). (d) Atomic figure obtained by DFT calculation of relaxed monoclinic Li_2MnO_3 structure.

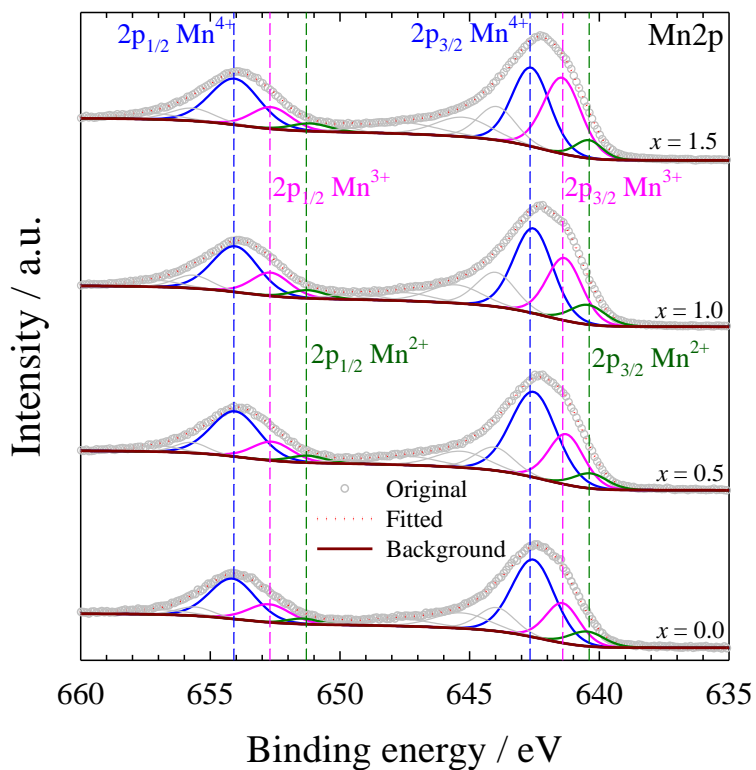


Figure 6.1.6 *Ex-situ* XPS spectra after Ar ion sputtering time of 60 s on Mn 2p at different SOC states; $x = 0.0$ (OCV), 0.5, 1.0, and 1.5 of $\text{Li}_{2-x}\text{MnO}_3$.

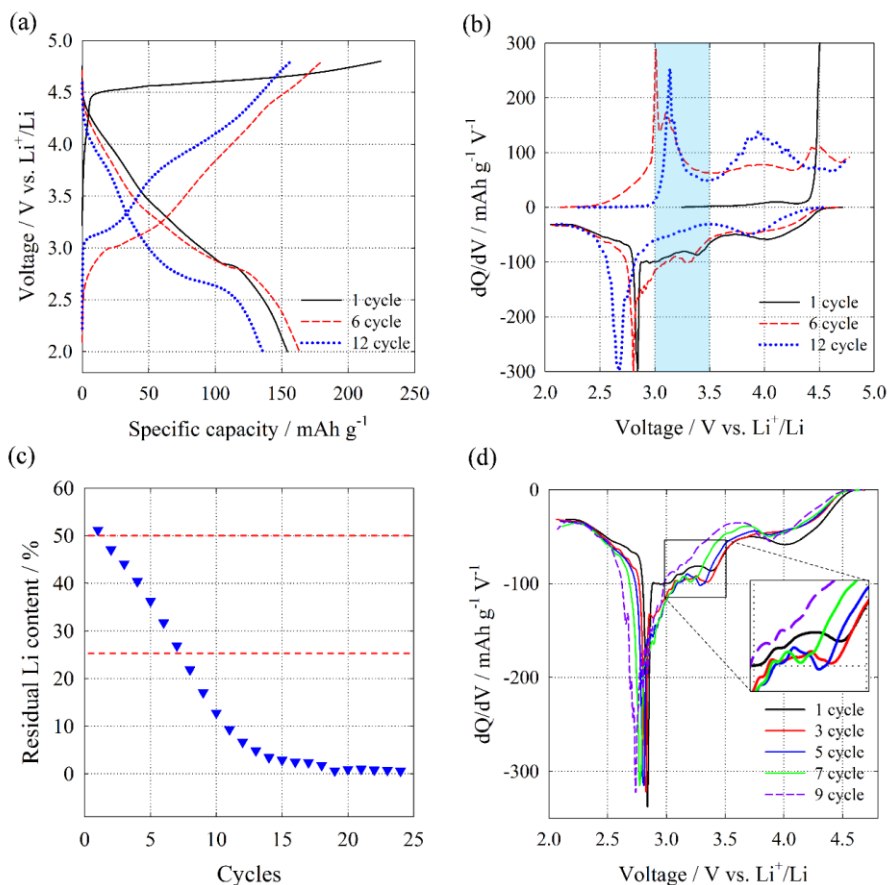


Figure 6.1.7 (a) Galvanostatic charge-discharge profiles recorded by CC charging mode with a constant current density of 23 mA g^{-1} in the voltage range between 2.0 and 4.8 V vs. Li/Li^+ at the 1st, 6th, 12th cycles and (b) Corresponding dQ/dV curves. (c) Residual Li content x in $\text{Li}_{2-x}\text{MnO}_3$ electrode and (d) Corresponding dQ/dV curves of the Li_2MnO_3 during the discharge at the 1st, 3rd, 5th, 7th, and 9th cycles.

6.2 Effects of Defects in Monoclinic Li_2MnO_3 [20]

Following the previous study introduced in Section 6.1 as a solution for suppressing the phase transformation of Li_2MnO_3 , [11] We present a combined experimental and computational study of an oxygen-deficient $\text{Li}_2\text{MnO}_{3-\delta}$ ($\delta \approx 0.071$) cathode for understanding the role and effects of the oxygen vacancies on phase transformation and electrochemical activity in Li-ion batteries. The oxygen-deficient $\text{Li}_2\text{MnO}_{3-\delta}$ exhibits improved electrochemical reactivity toward Li^+ without significant loss of structural stability. The oxidation of O during Li^+ extraction can be suppressed by the enhanced redox reaction of Mn in this material. Furthermore, the inevitable phase transformation of Li_2MnO_3 can be impeded by the increased kinetic barriers to Mn migration in $\text{Li}_2\text{MnO}_{3-\delta}$ ($\Delta E_{\text{barrier}} = 1 \sim 2.5$ eV), because of the obstacle to the formation of intermediate stable coordination geometries due to the oxygen vacancies. These findings reveal the underlying mechanism on the role of the oxygen vacancies in changing phase transformation and electrochemical activity in inactive Li_2MnO_3 , and provide a scientific insight to the electrochemical reactivity and sustainability of Li-rich oxide cathode materials in Li-ion batteries.

For experimental studies, $\text{Li}_2\text{MnO}_{3-\delta}$ was successfully prepared by a carbothermal reduction of Li_2MnO_3 synthesized at 850 °C, followed by a post heat-treatment. Digital photos of as-prepared Li_2MnO_3 and $\text{Li}_2\text{MnO}_{3-\delta}$ powders are compared in Figure 6.2.1a and Figure 6.2.1b, which represent dramatic color change from brown (inset of 6.2.1a) to black (inset of 6.2.1b). The color change is generally induced by the formation of oxygen vacancies in the structure, because oxygen vacancies are responsible for lowering the band gap of $\text{Li}_2\text{MnO}_{3-\delta}$, directly affecting its light-absorbing character. Figure 6.2.2 shows a powder XRD pattern of the as-synthesized Li_2MnO_3 and $\text{Li}_2\text{MnO}_{3-\delta}$ samples with Rietveld refinement. All reflections of both synthesized materials are indexed to the monoclinic Li_2MnO_3 structure of the

$C2/m$ space group (JCPDS 84-1634). We detected a small reduction in the (130) and (131) peaks in the $\text{Li}_2\text{MnO}_{3-\delta}$ pattern, at 37.02° and 44.78° , respectively, compared with those of Li_2MnO_3 ; this may have been due to the formation of oxygen vacancies in the structure. Atomic models for DFT calculations described in Figure 6.2.1c and 6.2.1d were modelled for understanding the oxygen deficient $\text{Li}_2\text{MnO}_{3-\delta}$ and established based on the $C2/m$ space group, which are in good agreement with XRD patterns of the as-synthesized samples. The position of the oxygen vacancy in the $\text{Li}_2\text{MnO}_{3-\delta}$ structure was determined to be the 8j site (Figure 6.2.1d), based on thermodynamic comparisons of the oxygen vacancy formation enthalpies for all possible configurations, our Rietveld refinement and from previous reports.

Both Li_2MnO_3 and $\text{Li}_2\text{MnO}_{3-\delta}$ have similar particle sizes ($\sim 5 \mu\text{m}$), as confirmed by FESEM images shown in Figure 6.2.1a and 6.2.1b. Moreover, it is difficult to find any morphological difference between the materials. For further inspection, STEM analysis was conducted, as shown in Figure 6.2.3. We note that $\text{Li}_2\text{MnO}_{3-\delta}$ and Li_2MnO_3 have a fine atomic arrangement in the directions of the (001), (200), and (20-2) planes, as confirmed by fast Fourier transformation (FFT) patterns with a zone axis of [010].

For further structural investigation of Li_2MnO_3 and $\text{Li}_2\text{MnO}_{3-\delta}$, we carefully carried out Rietveld refinements for obtained powder XRD patterns using a High-Score Plus software as shown in Figure 6.2.2a and Figure 6.2.2b. The Rietveld refinement analyses allow for quantitative probing of crystal structures of Li_2MnO_3 and $\text{Li}_2\text{MnO}_{3-\delta}$. According to the results, the as-prepared Li_2MnO_3 shows a fine crystal structure (JCPDS 84-1634). In contrast, we found slight increases in the lattice parameters, volume, and average bond length between Mn and O in the $\text{Li}_2\text{MnO}_{3-\delta}$ structure (Table 6.2.1), which has a similar inclination with the calculated values based on our atomic models for the first-principles calculations. In addition, increased average bond length between Mn and O of $\text{Li}_2\text{MnO}_{3-\delta}$ represents the weaker bonding of Mn and O

owing to the deficiency of oxygen ions, which corresponds to the slightly expanded structural parameters of $\text{Li}_2\text{MnO}_{3-\delta}$.

The presence of oxygen vacancies in the $\text{Li}_2\text{MnO}_{3-\delta}$ was confirmed using both quantitative and qualitative techniques. Table 6.2.1 show oxygen deficiencies from the Rietveld refinement and DFT calculation. From the occupancies of oxygen (O(4i): 1.0 and O(8j): 0.9646) in Rietveld refinement, oxygen deficiency of 0.071 was estimated. Moreover, Thermogravimetric analysis (TGA) represents a maximum weight percent of around 100.7 % at 170 °C. From the result, we can deduce that oxygen deficiency (δ) of $\text{Li}_2\text{MnO}_{3-\delta}$ could be estimated as more than 0.044 with consideration for the weight loss from residual water evaporation in the sample. In practice, it is well recognized that the oxygen deficient $\text{Li}_2\text{MnO}_{3-\delta}$ phase absorbed oxygen into the bulk structure at first weight gain period, and then the phase decomposed in the layered- and spinel-type phases with a loss of oxygen again. In order to clearly understand the effects of oxygen vacancy in Li_2MnO_3 , we modelled $\text{Li}_2\text{MnO}_{3-\delta}$ atomic model for DFT calculation with larger oxygen vacancies ($\delta = 0.25$) than that of the experiments, as described in Figure 6.2.1d.

Figure 6.2.4 compares the XPS spectra of Li_2MnO_3 and $\text{Li}_2\text{MnO}_{3-\delta}$ for the Mn 2p signals. From this comparison, we determined that the characteristic Mn 2p peaks in the $\text{Li}_2\text{MnO}_{3-\delta}$ were slightly shifted to a lower binding energy than those of Li_2MnO_3 , indicating that the binding energy between the Mn and O ions in $\text{Li}_2\text{MnO}_{3-\delta}$ was weakened by the oxygen deficiency, which is well-matched with increased average bond length between Mn and O. In addition, we focused on the change in the valence state of Mn. Several peaks corresponding to Mn^{4+} ($2p_{3/2}$: ~642.5 eV and $2p_{1/2}$: 654.1 eV), Mn^{3+} ($2p_{3/2}$: ~641.2 eV and $2p_{1/2}$: 652.5 eV), and Mn^{2+} ($2p_{3/2}$: ~640.4 eV and $2p_{1/2}$: 651.2 eV) were obvious in the spectra collected from both Li_2MnO_3 and $\text{Li}_2\text{MnO}_{3-\delta}$ samples. Mn^{4+} state is dominant in both of

Li_2MnO_3 and $\text{Li}_2\text{MnO}_{3-\delta}$, but Mn^{3+} and Mn^{2+} peaks are slightly increased at $\text{Li}_2\text{MnO}_{3-\delta}$ comparing to those of Li_2MnO_3 , which means electrochemically active Mn ions would be increased due to the formation of oxygen vacancies.

In order to clarify the role of oxygen vacancy in the $\text{Li}_2\text{MnO}_{3-\delta}$ structure, we performed theoretical investigations using a first-principles calculation. As shown in Figure 6.2.5a, not only the enthalpy of the Li^+ extraction for $\text{Li}_{2-x}\text{MnO}_{3-\delta}$ was generally lower than that of $\text{Li}_{2-x}\text{MnO}_3$, but also the enthalpies of formation for $\text{Li}_{2-x}\text{MnO}_{3-\delta}$ and $\text{Li}_{2-x}\text{MnO}_3$ were found to be below zero during the Li^+ extraction. Thus, it is worthwhile to note that the oxygen-deficient $\text{Li}_2\text{MnO}_{3-\delta}$ structure could be more structurally stable than the stoichiometric Li_2MnO_3 structure during Li^+ extraction. Regarding the oxygen evolution from Li_2MnO_3 during cycling, we also investigated the oxygen stability in the $\text{Li}_2\text{MnO}_{3-\delta}$ structure by calculating the formation enthalpy of the additional oxygen vacancies E_{O} (Figure 6.2.4b). From these results, we infer that additional oxygen vacancy formation is less favorable in an oxygen-deficient $\text{Li}_2\text{MnO}_{3-\delta}$ structure ($E_{\text{O}} \approx 0$ eV at $x = 1.0$) compared to a stoichiometric Li_2MnO_3 structure ($E_{\text{O}} \approx 0$ eV at $x = 0.75$).

Figure 6.2.6a shows the PDOS of the structures after partial Li^+ extraction for $\text{Li}_{1.75}\text{MnO}_3$ (top) and $\text{Li}_{1.75}\text{MnO}_{3-\delta}$ (bottom). While a small number of electrons were extracted from the Mn d-orbital of $\text{Li}_{1.75}\text{MnO}_3$, a remarkably large number of electrons were withdrawn from the Mn d-orbital of $\text{Li}_{1.75}\text{MnO}_{3-\delta}$ during the Li^+ extraction. This supports the conclusion that the oxygen-deficient $\text{Li}_2\text{MnO}_{3-\delta}$ structure allows for greater enhancement of the Mn ion redox reaction and reduced O ion oxidation than the stoichiometric Li_2MnO_3 . For quantitative analysis, the average net charges of the Mn and O ions of both structures were compared, as shown in Figure 6.2.6b. We observed an increased Mn ion charge variation in $\text{Li}_{2-x}\text{MnO}_{3-\delta}$ during Li^+ extraction, which was responsible for the enhanced Mn ion redox reaction. $\text{Li}_{2-x}\text{MnO}_{3-\delta}$ exhibits a lower average net O ion charge, indicating a more

stable O ion electronic structure than $\text{Li}_{2-x}\text{MnO}_3$. As a result, the electronic band structures indicate that the oxygen-deficient $\text{Li}_2\text{MnO}_{3-\delta}$ (Figure 6.2.6d) exhibits a narrow band gap (a better electronic conductivity) compared to that of the stoichiometric Li_2MnO_3 structure (Figure 6.2.6c), because the released electrons from the oxygen vacancies form energy bands in the -0.6 eV region.

To investigate the correlation between oxygen vacancy and the electrochemical properties of Li_2MnO_3 , we examined the electrochemical performance of Li_2MnO_3 and $\text{Li}_2\text{MnO}_{3-\delta}$ as cathodes for LIBs. Figure 6.2.7a shows the galvanostatic charge (Li^+ extraction) and discharge (Li^+ insertion) profiles of both cathodes recorded at a constant current of 10 mA g^{-1} , where the specific capacity of $\text{Li}_2\text{MnO}_{3-\delta}$ is almost twice than that of Li_2MnO_3 . The reaction voltage of $\text{Li}_2\text{MnO}_{3-\delta}$ is lower than that of Li_2MnO_3 , which is in good agreement with the average calculated voltages (in inset of Figure 6.2.7a). The improved reactivity toward Li^+ insertion and extraction can be reasonably explained by the enhanced Mn ion redox reaction and the reduced O ion oxidation in the $\text{Li}_2\text{MnO}_{3-\delta}$ structure, allowing smooth Li^+ extraction. In addition, the $\text{Li}_2\text{MnO}_{3-\delta}$ phase transformation proceeded slowly during cycling, as evidenced by Figure 6.2.7b. $\text{Li}_2\text{MnO}_{3-\delta}$ exhibited a maximum specific capacity ($\sim 59.5 \text{ mAh g}^{-1}$) at the 20th cycle, approximately 95% of which was then retained until 50 cycles were completed. In contrast, Li_2MnO_3 exhibited a considerably smaller specific capacity ($\sim 32.5 \text{ mAh g}^{-1}$) and more severe capacity fading. Note that the $\text{Li}_2\text{MnO}_{3-\delta}$ phase transformation occurs more slowly than that of Li_2MnO_3 . In other words, the oxygen vacancy in $\text{Li}_2\text{MnO}_{3-\delta}$ would impede the phase transformation.

To elucidate the origins and mechanism of the interruption of the $\text{Li}_2\text{MnO}_{3-\delta}$ phase transformation by the oxygen vacancies, the kinetic barriers to the Mn migration from the 4g to 4h sites for both Li_2MnO_3 and $\text{Li}_2\text{MnO}_{3-\delta}$ were examined, for various Li contents. Figure 6.2.7c gives the higher Mn migration barriers in the $\text{Li}_2\text{MnO}_{3-\delta}$ structure ($\Delta E_{\text{barrier}} = 1 \sim 2.5 \text{ eV}$), which

would impede the $\text{Li}_2\text{MnO}_{3-\delta}$ phase transformation. Our analysis suggests that the higher migration barriers originate from changes in the coordination geometry due to the oxygen vacancies. Unlike Mn ions, which have an octahedral coordination geometry (coordination number: 6) in Li_2MnO_3 , the Mn ion coordination number in $\text{Li}_2\text{MnO}_{3-\delta}$ is 5 due to an absent oxygen ion. However, the Mn ions at the intermediate migration states (upper inset of Figure 6.2.7d) have a coordination number of 3, which is insufficient for the formation of a stable coordination geometry, e.g., tetrahedral and octahedral structures.

Figure 6.2.7d shows a comparison of the barriers to Mn migration from the 4g to 4h sites in $\text{Li}_{1.75}\text{MnO}_3$ and $\text{Li}_{1.75}\text{MnO}_{3-\delta}$, and the corresponding atomic structures during this migration. This figure indicates that the Mn migration barrier in $\text{Li}_{1.75}\text{MnO}_{3-\delta}$ (~5.49 eV) is considerably higher than that in $\text{Li}_{1.75}\text{MnO}_3$ (~3.10 eV). Furthermore, during the migration, the Mn and O ions cannot establish a stable coordination geometry in the $\text{Li}_{1.75}\text{MnO}_{3-\delta}$ structure, which differs from the formation of a tetrahedral coordination geometry observed in the $\text{Li}_{1.75}\text{MnO}_3$ structure (lower inset of Figure 6.2.7d). Hence, the Mn and O atomic frameworks become unstable during the Mn migration, leading to increased kinetic migration barriers, which slows the phase transformation kinetics.

With the aim of understanding mechanism of the role and effects on the phase transformation and electrochemical activity toward Li^+ of inactive Li_2MnO_3 configured with Mn^{4+} , the structural and electrochemical properties of oxygen-deficient $\text{Li}_2\text{MnO}_{3-\delta}$ have been thoroughly investigated through both experiment and first-principles calculation. The oxygen-deficient $\text{Li}_2\text{MnO}_{3-\delta}$ ($\delta \approx 0.071$) has the same crystal structure as stoichiometric Li_2MnO_3 , with slightly expanded lattice parameters. The $\text{Li}_2\text{MnO}_{3-\delta}$ exhibited improved electrochemical reactivity for Li^+ insertion and extraction without structural degradation. In addition, the more beneficial effects of the oxygen

vacancies in the $\text{Li}_2\text{MnO}_{3.6}$ structure were clearly identified, such as lowering of the activation voltage and delaying of the phase transformation from a structural perspective. The understood underlying mechanisms of the oxygen vacancies are the suppressed oxidation of oxygen by the enhanced redox reaction of Mn (lowering of the voltage), and the increased migration barriers of Mn ($\Delta E_{\text{barrier}} = 1 \sim 2.5$ eV) by the unstable intermediate migration states (delaying of the phase transformation). It is expected that these understandings provide an useful conceptual framework of using similar defects (*e.g.*, halogen substitution of oxygen) to improve and modify the electrochemical reactivity and sustainability of Li-rich oxide cathode materials such as $x\text{Li}_2\text{MnO}_3 \cdot (1-x)\text{LiMO}_2$ and Li_2MO_3 in Li-ion batteries.

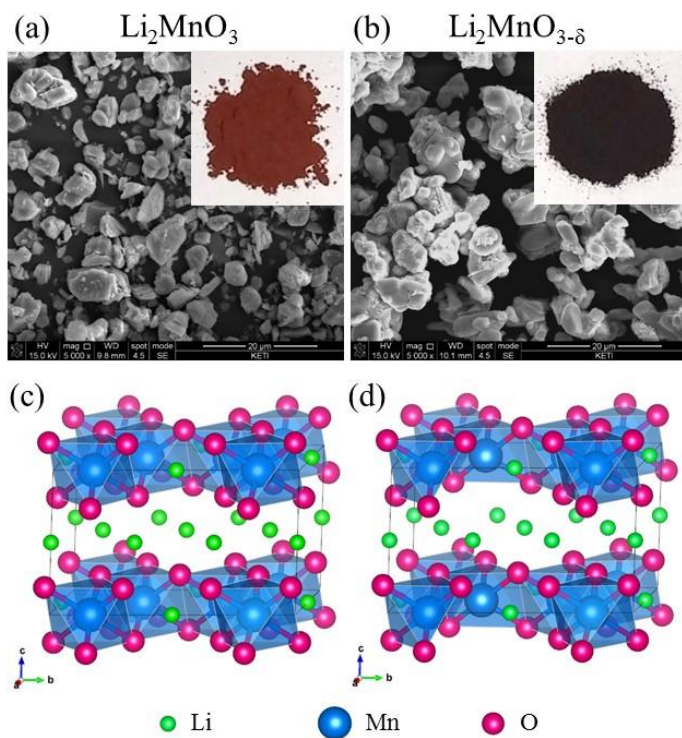


Figure 6.2.1 (a, b) FESEM images of (a) Li_2MnO_3 and (b) $\text{Li}_2\text{MnO}_{3-\delta}$. As-synthesized Li_2MnO_3 (inset of a) and $\text{Li}_2\text{MnO}_{3-\delta}$ (inset of b) powders. (c, d) Atomic models for DFT calculations of monoclinic (c) Li_2MnO_3 and (d) $\text{Li}_2\text{MnO}_{3-\delta}$ structures (space group: $C2/m$).

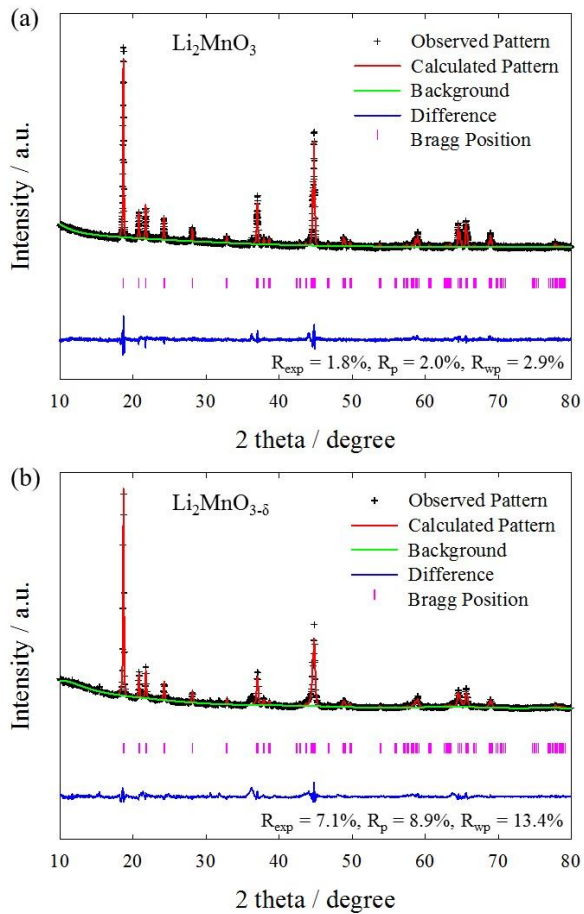


Figure 6.2.2 (a, b) Rietveld refinement of XRD patterns of (a) Li_2MnO_3 and (b) $\text{Li}_2\text{MnO}_{3-\delta}$ with agreement indices of the Rietveld refinement such as expected R factor (R_{exp}), R profile factor (R_p), and weighted R profile factor (R_{wp}).

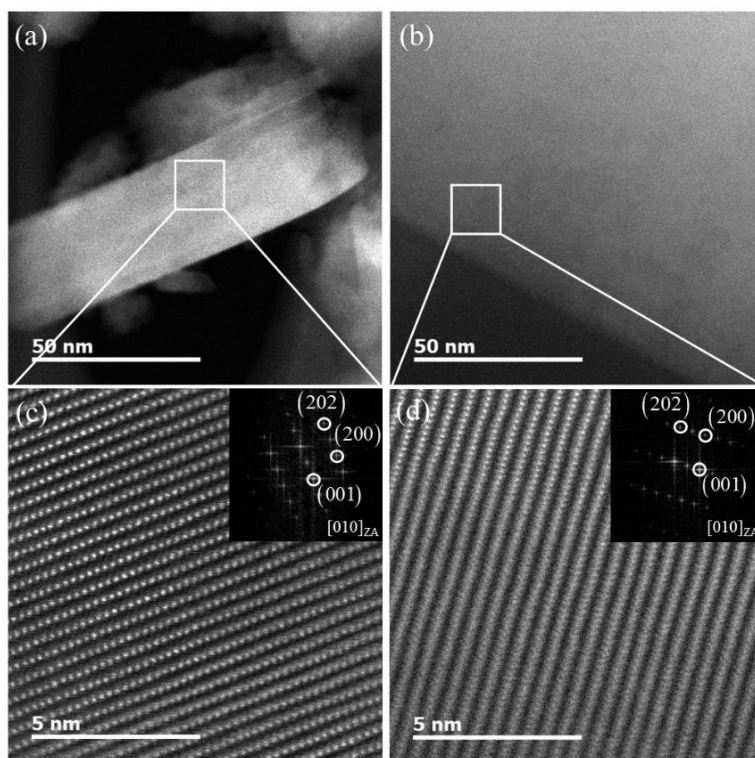


Figure 6.2.3 (a, b) STEM images of (a) Li_2MnO_3 and (b) $\text{Li}_2\text{MnO}_{3-\delta}$. (c, d) Magnified STEM images of the panel in (a) and (b) of synthesized (c) Li_2MnO_3 and (d) $\text{Li}_2\text{MnO}_{3-\delta}$ with corresponding FFT images with zone axis (inset).

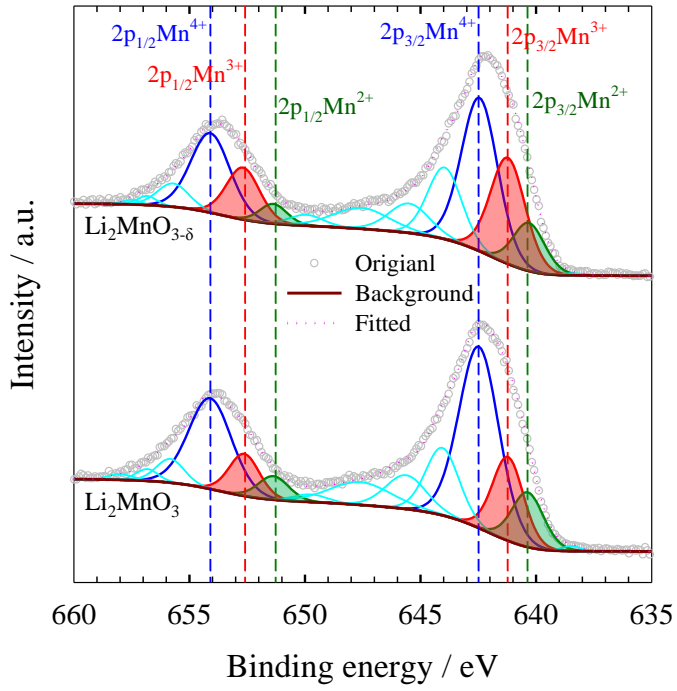


Figure 6.2.4 XPS spectra of Mn 2p for Li_2MnO_3 and $\text{Li}_2\text{MnO}_{3-\delta}$ after an Ar ion sputtering time of 300 s.

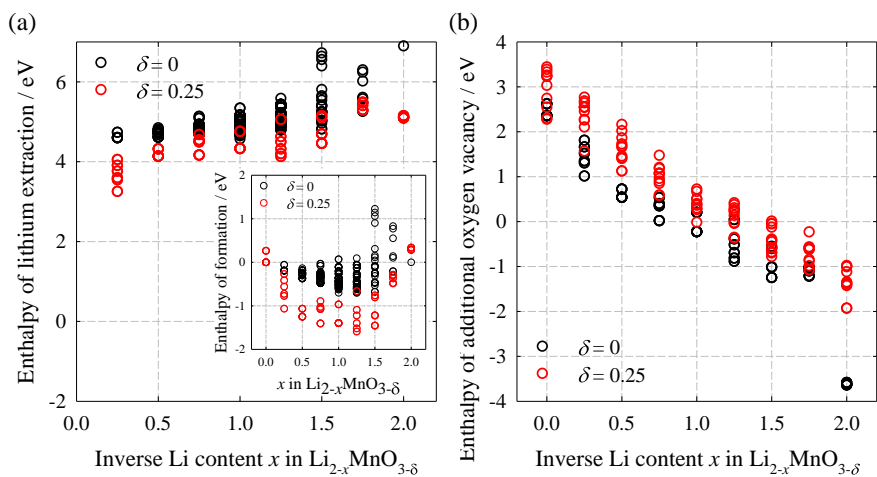


Figure 6.2.5 (a) Enthalpy of lithium extraction and enthalpy of formation (inset of a), enthalpy of (b) additional oxygen vacancy for $\text{Li}_{2-x}\text{MnO}_3$ (black circles) and $\text{Li}_{2-x}\text{MnO}_{3-\delta}$ (red squares) with respect to inverse Li content x in $\text{Li}_{2-x}\text{MnO}_{3-\delta}$.

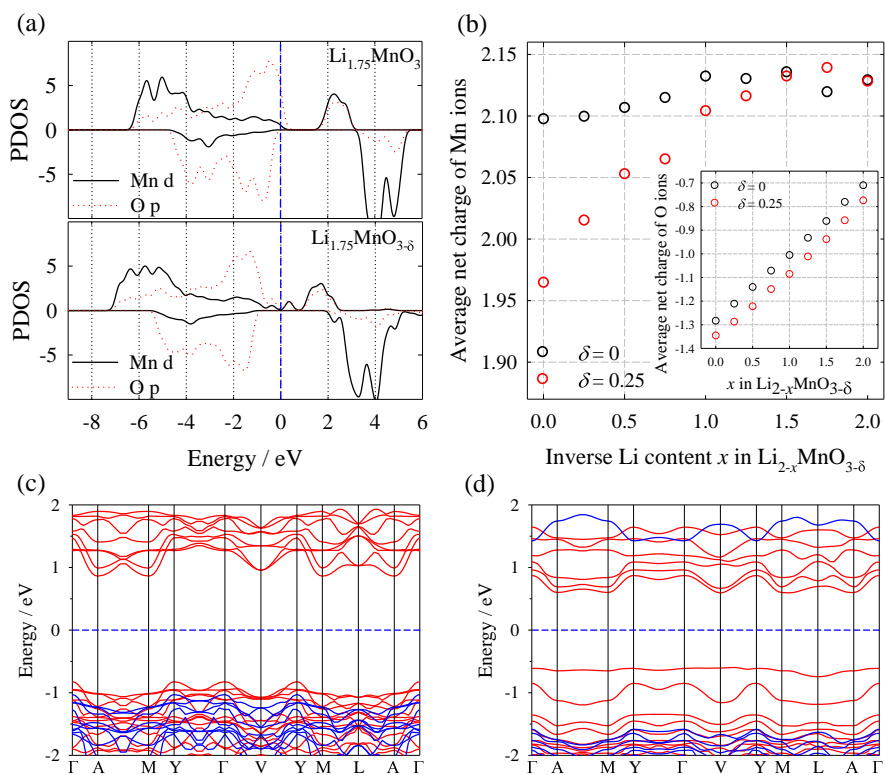


Figure 6.2.6 (a) PDOS for Mn d- (black line) and O p-orbitals (red dotted line) of $\text{Li}_{1.75}\text{MnO}_3$ (top) and $\text{Li}_{1.75}\text{MnO}_{3-\delta}$ (bottom). (b) Average Mn- and O-ion net charges (b, inset) for $\text{Li}_{2-x}\text{MnO}_3$ (black circles) and $\text{Li}_{2-x}\text{MnO}_{3-\delta}$ (red squares) with respect to the inverse Li content x in $\text{Li}_{2-x}\text{MnO}_{3-\delta}$. (c, d) Spin-resolved electronic band structures for spin-up (red line) and spin-down (blue line) for (c) Li_2MnO_3 and (d) $\text{Li}_2\text{MnO}_{3-\delta}$. The Fermi level is 0 eV (blue dashed line).

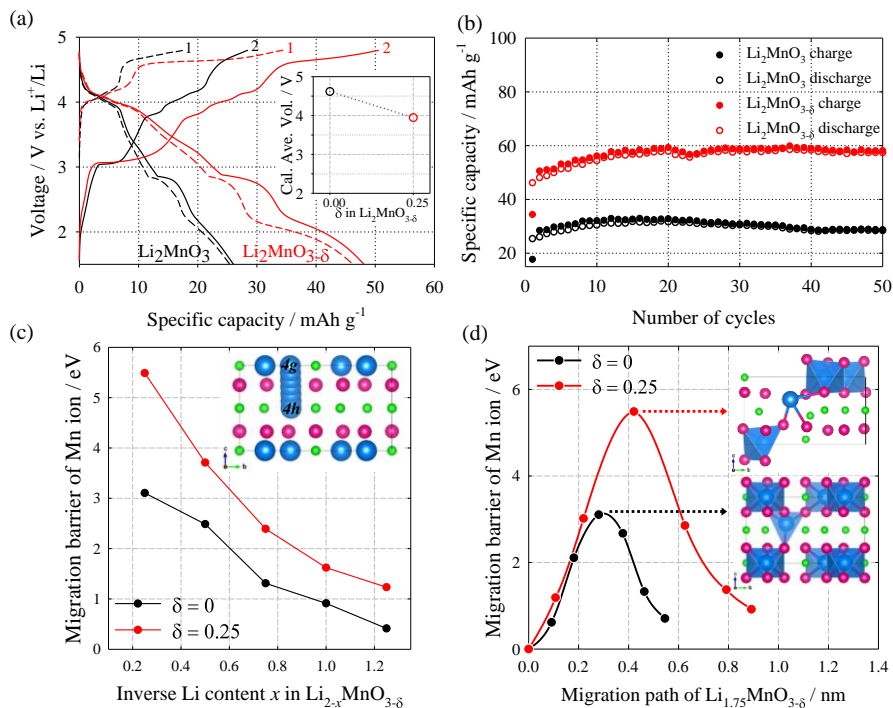


Figure 6.2.7 (a) Galvanostatic charge-discharge profiles at 10 mA g^{-1} for 1.5–4.8 V vs. Li/Li^+ of Li_2MnO_3 (black) and $\text{Li}_2\text{MnO}_{3-\delta}$ (red) at 1st (dashed line) and 2nd (solid line) cycles, and (inset) calculated average Li_2MnO_3 (black circle) and $\text{Li}_2\text{MnO}_{3-\delta}$ (red circle) voltages. (b) Comparison of Li_2MnO_3 (black circles) and $\text{Li}_2\text{MnO}_{3-\delta}$ (red squares) cycling performances. (c) Mn migration barriers (4g to 4h site) with respect to inverse Li content x in $\text{Li}_{2-x}\text{MnO}_3$ (black line with black circles) and $\text{Li}_{2-x}\text{MnO}_{3-\delta}$ (red line with red squares). (d) Mn migration barriers (4g to 4h site) with respect to migration paths in $\text{Li}_{1.75}\text{MnO}_3$ (black line with black circles) and $\text{Li}_{1.75}\text{MnO}_{3-\delta}$ (red line with red squares), and their atomic structures at the migration center-point (insets).

Table 6.2.1 Comparison of oxygen deficiency δ , volume, and average bond length between Mn and O of Li_2MnO_3 and $\text{Li}_2\text{MnO}_{3-\delta}$, obtained by Rietveld refinement of XRD patterns and DFT calculations.

		δ	Vol. [\AA^3]	$\langle\text{Mn-O}\rangle[\text{\AA}]$
Li_2MnO_3	Rietveld	0.0	198.27	1.9207
	DFT	0.0	208.67	1.9408
$\text{Li}_2\text{MnO}_{3-\delta}$	Rietveld	~ 0.071	199.14	1.9360
	DFT	0.250	214.91	1.9608
	TGA	> 0.044	-	-

6.3 Effects of Crystal Field Stabilization in High-Mn, Li-rich Oxides[21]

For advance to Li-rich oxides from Li_2MnO_3 by TM doping, high-Mn, Li-rich oxides (HMLOs; $x\text{Li}_2\text{MnO}_3$ $(1-x)\text{LiNi}_{1/3}\text{Co}_{1/3}\text{Mn}_{1/3}\text{O}_2$ at $x > 0.5$) warrant in-depth study because of their good cyclic performance at high operating voltages and potentially large specific capacities. Here, to understand the synergistic effects and enhanced cyclic stability of HMLOs, mechanically blended HMLO (m-HMLO) and chemically bonded HMLO (c-HMLO) were prepared and investigated. c-HMLO exhibits relatively high reaction voltages, large specific capacities, and enhanced cyclic stabilities (~99 %) at a high operating voltage (~4.8 V vs. Li/Li^+) compared with m-HMLO. First-principles calculations with electronic structure analysis were performed with an atomic model developed by Rietveld refinement using as-synthesized c-HMLO. The redox mechanisms of Ni, Co, and Mn ions were determined *via* the PDOSs of the ground states predicted by the CEM, which elucidates that $\text{LiNi}_{1/3}\text{Co}_{1/3}\text{Mn}_{1/3}\text{O}_2$ stabilizes the TM layer of Li_2MnO_3 and separates Li delithiation potentials in Li_2MnO_3 in the HMLO. Kinetic analyses including electronic structures revealed that the interlayer migration from the TM layer to the Li layer of TMs depends on the crystal field stabilization. Thus, TMs with reduced character in the tetrahedral sites than the octahedral sites owing to the effects of the crystal field stabilization, such as Ni ions, in HMLO would face a higher interlayer migration barrier, impeding phase transformation to spinel phases. Furthermore, Cu ion could constitute a doping source for HMLO to improve the material's cyclic stability through this mechanism. These characteristics may be widely applied to explain experimental phenomena and improve the properties of cathode materials for Li-ion batteries.

To fundamentally understand the differences between HMLOs and the existing TM layered oxides ($\text{LiNi}_{1/3}\text{Co}_{1/3}\text{Mn}_{1/3}\text{O}_2$) and Li_2MnO_3 and to elucidate the synergistic effects between inactive Li_2MnO_3 and

$\text{LiNi}_{1/3}\text{Co}_{1/3}\text{Mn}_{1/3}\text{O}_2$, m-HMLO with chemically separated phases and c-HMLO with chemically bonded phases were prepared with following composition: $2/3\text{Li}_2\text{MnO}_3 \cdot 1/3\text{LiNi}_{1/3}\text{Co}_{1/3}\text{Mn}_{1/3}\text{O}_2$. Figure 6.3.1a presents the XRD patterns of m-HMLO (black line) and c-HMLO (red line) powders, and the insets show the enlarged superlattice peaks indexed to (020) and (110) planes from 20° to 24° , which were mainly contributed by the Li_2MnO_3 phase. Because of the formation of the chemically bonded phase of c-HMLO during synthesis, the XRD pattern of c-HMLO shows sharper peaks than that of m-HMLO, including the superlattice peaks.

For in-depth structural characterization of the as-prepared m-HMLO and c-HMLO materials, STEM analysis coupled with EDS was performed, as described in Figure 6.3.1b, 6.3.1c, and 6.3.1d. Figure 6.3.1b and 6.3.1c show the images collected *via* STEM with EDS for separated Li_2MnO_3 and $\text{LiNi}_{1/3}\text{Co}_{1/3}\text{Mn}_{1/3}\text{O}_2$ phases. In addition to the STEM with EDS analyses described above, the corresponding SAED patterns of both the Li_2MnO_3 (inset of Figure 6.3.1b) and $\text{LiNi}_{1/3}\text{Co}_{1/3}\text{Mn}_{1/3}\text{O}_2$ (inset of Figure 6.3.1c) phases were investigated to determine whether the separated phases maintained their unique crystal structures. The inset of Figure 6.3.1b shows the SAED pattern of the Li_2MnO_3 phase with a $C2/m$ structure and a zone axis of [010], whereas Figure 6.3.1c focuses on the $\text{LiNi}_{1/3}\text{Co}_{1/3}\text{Mn}_{1/3}\text{O}_2$ phase, and the inset of Figure 6.3.1c presents the SAED pattern of the $\text{LiNi}_{1/3}\text{Co}_{1/3}\text{Mn}_{1/3}\text{O}_2$ phase with a $R-3m$ structure and a zone axis of [0001]. Based on Figure 6.3.1b and 6.3.1c, m-HMLO is confirmed to consist of a mechanically blended (chemically separated) powder of the Li_2MnO_3 and $\text{LiNi}_{1/3}\text{Co}_{1/3}\text{Mn}_{1/3}\text{O}_2$ phases.

By contrast, Figure 6.3.1d shows the images collected *via* STEM with EDS of the c-HMLO powder. Here, the chemically bonded particles can be clearly identified in the low magnification STEM images with uniformly distributed EDS mapping data for Ni, Co, and Mn. To confirm the detailed

crystal structure of the chemically bonded c-HMLO in Figure 6.3.1d, STEM images with higher magnifications were compared with the FFT image shown in Figure 6.3.1e. Figure 6.3.1e reveals fine atomic arrangements with crystallinity, and the inset of Figure 6.3.1e presents the FFT pattern, which indicates a $C2/m$ crystal structure with a zone axis of [010]. Therefore, Figure 6.3.1d and 6.3.1e confirm that the as-prepared c-HMLO consists of chemically bonded Li_2MnO_3 and $\text{LiNi}_{1/3}\text{Co}_{1/3}\text{Mn}_{1/3}\text{O}_2$ phases with a $C2/m$ crystal structure.

Galvanostatic charge-discharge experiments were performed to characterize the electrochemical behaviors of m-HMLO and c-HMLO, as shown in Figure 6.3.2. Figure 6.3.2a and 6.3.2b present the charge-discharge profiles of m-HMLO and c-HMLO with a constant specific current of 25 mA g^{-1} in the voltage range of 2.0 to 4.8 V vs. Li/Li^+ at the 1st, 2nd, and 20th cycles. Comparing Figure 6.3.2a and 6.3.2b reveals that the electrochemical reaction voltages of c-HMLO are higher than those of m-HMLO from the initial charging process at the 1st cycle. Additionally, the specific capacities of c-HMLO are much larger than those of m-HMLO. To examine and compare the reaction voltages of m-HMLO and c-HMLO in greater detail, the corresponding differential capacity (dQ/dV) curves at the 1st and 20th cycles are shown in Figure 6.3.2c. The upper graph of Figure 6.3.2c shows that the first charge process of c-HMLO (red dashed line) starts at approximately 4.0 V vs. Li/Li^+ , whereas that of m-HMLO (black solid line) starts at approximately 3.65 V vs. Li/Li^+ . Similarly, at the 20th cycle, the reaction voltages of c-HMLO are generally higher than those of m-HMLO.

The cyclic performances of m-HMLO (black circle) and c-HMLO (red circle) over 50 cycles were also determined, as shown in Figure 6.3.2d. Both the charge and discharge cyclic performances of c-HMLO are enhanced compared with those of m-HMLO. The first discharge capacity of m-HMLO (black filled circle) is 81.96 mAh g^{-1} , and it decreases to 50.54 mAh g^{-1} in the

50th cycle, where the discharge capacity retention is approximately 62 %. In the case of the discharge process (red filled circle) of c-HMLO, the discharge capacity gradually increased from 124.10 mAh g⁻¹ to 175.27 mAh g⁻¹ at the initial cycles induced by the electrochemical activation, which is also maintain at 174.33 mAh g⁻¹ in the 50th cycle, where the discharge capacity retention is approximately 99 %. This enhanced cyclic stability of c-HMLO at a high operating voltage is considered to be a synergistic effect of Li₂MnO₃ and LiNi_{1/3}Co_{1/3}Mn_{1/3}O₂ in HMLO because the cyclic performances of Li₂MnO₃ and LiNi_{1/3}Co_{1/3}Mn_{1/3}O₂ gradually decrease as the number of cycles increases.[21] Therefore, HMLO is affected by a hidden synergistic effect, which is difficult to elucidate based on the electrochemical performances of Li₂MnO₃ and LiNi_{1/3}Co_{1/3}Mn_{1/3}O₂. An in-depth discussion of these effects will be included in the theoretical parts below.

To achieve a fundamental understanding of the interesting experimental phenomena exhibited by HMLO, such as its improved electrochemical characteristics and enhanced cyclic stabilities, first-principles investigations were performed according to thermodynamic, kinetic, and statistical approaches. To develop a reasonable atomic model of the HMLO system, we modelled the HMLO atomic structure based on the C2/m crystal structure with 9 formula units of 2/3Li₂MnO₃ · 1/3LiNi_{1/3}Co_{1/3}Mn_{1/3}O₂, as described in Figure 6.3.3a, because the XRD pattern of the c-HMLO in Figure 6.3.1a shows sharp superlattice peaks of the (020) and (110) planes. Additionally, the locations of Ni, Co, and Mn atoms corresponding to LiNi_{1/3}Co_{1/3}Mn_{1/3}O₂ were determined by thermodynamic energy comparisons through DFT calculations. To validate the appropriateness of this HMLO atomic model in terms of the as-prepared c-HMLO powder, Rietveld refinement was performed by analyzing the XRD pattern of the c-HMLO in Figure 6.3.1a and the developed atomic model in Figure 6.3.3a. Figure 6.3.3b shows the result of the Rietveld refinement with a weighted R profile of 3.767 and an R profile of 2.524.

These values confirm that the simulation model presented in Figure 6.3.3a can reasonably describe the behavior of the as-prepared c-HMLO powder.

To perform an in-depth theoretical investigation of the HMLO system at various Li concentrations, 16 ground states for each Li concentration were evaluated by CEM, followed by complete relaxation of both the cell and the atoms. Based on these CEM results, the reaction voltage and average charge variation with respect to various Li concentrations were evaluated as described in Figure 6.3.4a. The calculated voltage (blue solid line) exhibited a slope similar to that of the experimental charge profile (red dashed line): the initial reaction began at approximately 4 V *vs.* Li/Li⁺ and exceeded 4.5 V *vs.* Li/Li⁺ at approximately 100 mAh g⁻¹. The inset of Figure 6.3.4a presents the average charge variation, which reflects the redox reaction behaviors of TMs and O: Ni and Co ions are likely to participate in redox reactions from 0 to 100 mAh g⁻¹ at voltages below 4.5 V *vs.* Li/Li⁺ (green box). Meanwhile, Mn ions retain their inactive character and participate minimally in the redox reaction. More importantly, the redox reactions are generated below voltages around 4.7 V *vs.* Li/Li⁺ until 270 mAh g⁻¹ due to the intercalation of Li ions in the Li layer, but the remarkable voltage increase is observed from the intercalation of Li ions in the TM layer after 270 mAh g⁻¹. In other words, the intercalation potential of Li ions in the TM layer is higher than that of Li ions in the Li layer, since the NCM component would stabilize the TM layer of the HMLO system and could help a structural stability of Li₂MnO₃ during Li intercalations.

Based on the qualitative results obtained for the PDOSs of the Mn, Co, and Ni d orbitals in Figure 6.3.4b, 6.3.4c, and 6.3.4d, the behaviors of Ni, Co, and Mn ions described above are consistent. Figure 6.3.4b confirms the inactivity of the Mn⁴⁺ ion at two different Li concentrations, while the Co ion changes its oxidation state from Co³⁺ to Co^{3~4+} as the Li concentration decreases in Figure 6.3.4c. Additionally, Figure 6.3.4d indicates that Ni ions

exist in the relatively stable Ni^{2+} state when the system is fully lithiated (black line) because of the d electron-donor effect[11, 38, 60] and changes to the Ni^{4+} state in $\text{Li}_{1.34}\text{Ni}_{0.11}\text{Co}_{0.11}\text{Mn}_{0.78}\text{O}_{2.67}$ (red dashed line) through the double redox reaction. For Ni ions, the Ni^{2+} state is more stable than the Ni^{3+} state in terms of its electronic structure because of the crystal field stabilization; therefore, the redox potential of the Ni^{2+} state in this HMLO system (~ 4.1 V vs. Li/Li^+) is higher than that of the Ni^{3+} state in $\text{LiNi}_{1/3}\text{Co}_{1/3}\text{Mn}_{1/3}\text{O}_2$ (~ 3.75 V vs. Li/Li^+). This might be the reason why the HMLO system exhibits higher electrochemical reaction voltages, as observed above experiments.

The enhanced cyclic stability of c-HMLO was investigated *via* electronic structure analyses of the TMs' kinetic migration states to understand the origins and mechanism of the impeded phase transformation behaviors. In these migration simulations, the interlayer migrations of TMs from the TM layer to the Li layer through the tetrahedral site between two octahedral sites in these layers were handled as shown in the inset in Figure 6.3.5a: not only is passing through tetrahedral sites a geometrically indispensable pathway for migration from the TM layer to the Li layer,[10, 11] but an experimental study on Li-rich oxides obtained annular dark-field (ADF) TEM images of TMs in tetrahedral sites.[55]

Figure 6.3.5a describes the TM migration barriers faced by Mn, Co, and Ni ions in terms of the inverse Li content x in the HMLO atomic model. Here, the difference between the slopes of the Mn and Co ions and that of the Ni ions should be particularly noted. The migration barriers of Mn and Co ions decrease as Li is extracted, whereas that of the Ni ions increases during delithiation. The migration barriers of Mn and Co ions are 5.35 and 4.54 eV at $x = 0.11$ and decrease to 1.94 and 1.77 eV at $x = 0.78$, respectively. In contrast, the migration barrier of the Ni ions is 3.51 eV at $x = 0.11$, which increases to 4.86 eV at $x = 0.78$. More importantly, the increasing migration barriers of Ni ions and Mn and Co ions at high Li concentrations could contribute to the

impeded phase transformation of the HMLO system.

To determine the reason underlying the relatively high migration of Ni ions, the net charges of the Mn, Co, and Ni ions were determined *via* Bader charge analysis at different coordination geometries, as shown in Figure 6.3.5b. Based on the net charge variations of the initial octahedral site (TM layer), middle tetrahedral site (between layers), and final octahedral site (Li layer), the redox reactions—oxidation (electron loss) and reduction (electron gain)—affecting the TMs at different coordination geometries could be elucidated. Figure 6.3.5b shows that the net charges of Mn and Co ions in the middle tetrahedral site are slightly higher than those in the initial and final octahedral sites, indicating that Mn and Co ions are oxidized in the middle tetrahedral site. However, the net charge of Ni ions in the middle tetrahedral site is lower than those in the initial and final octahedral sites, indicating that Ni ions are reduced when passing through the middle tetrahedral site during migration. Hence, the reason underlying the higher migration of Ni ions in the HMLO system is attributable to its reduced character at the tetrahedral sites compared with the octahedral sites. To gain electrons, the Ni ion in the tetrahedral site is likely to take electrons from surrounding O atoms. As a result, the oxidized O atoms make the whole structure unstable, increasing its energy state and, thus, increasing the migration barrier faced by Ni ions. By contrast, the oxidized character of the Mn and Co ions allows them to donate electrons to surrounding O atoms, thereby stabilizing the entire structure, lowering its energy state, and decreasing the migration barriers.[11]

To understand the origins of the reduced and oxidized character of the TMs, the PDOS of Mn, Co, and Ni ions in $\text{Li}_{1.11}\text{Ni}_{0.11}\text{Co}_{0.11}\text{Mn}_{0.78}\text{O}_{2.67}$ at both the initial octahedral and middle tetrahedral sites are shown in Figure 6.3.5c, 6.3.5e, and 6.3.5g, with the corresponding crystal field splitting diagrams (CFSDs) presented in Figure 6.3.5d, 6.3.5f, and 6.3.5h, respectively. The PDOS of the Mn d orbital at the octahedral site (black solid line) describes the

electronic structure of Mn^{4+} state. The inactive character of Mn^{4+} in the fully lithiated state (black solid line in Figure 6.3.4b) indicates that three electrons occupy the t_{2g} level in the upper CFSD of Figure 6.3.5d. However, the Mn ion in the tetrahedral site (red dashed line) is oxidized to Mn^{4-5+} , as described in Figure 6.3.5b and 6.3.5c, because of the reversal of the crystal field shown in the lower CFSD of Figure 6.3.5d. In other words, the crystal field of the Mn ion in the tetrahedral site could be stabilized by filling the e level with two electrons and donating an electron to the surrounding O ions, thereby stabilizing the entire structure, decreasing its energy state, and reducing the migration barrier faced by Mn ions. Similarly, the PDOS of the Co d orbital in the octahedral site indicates the Co^{3-4+} state, as illustrated by the black solid line in Figure 6.3.5e, because slight oxidation from the Co^{3+} state at full lithiation (black solid line in Figure 6.3.4c) occurs during delithiation. During migration, the Co ion in the tetrahedral site (red dashed line) would be oxidized to Co^{4+} , as shown in Figure 6.3.5b and 6.3.5e, because of the reversal of the crystal field described in the lower CFSD of Figure 6.3.5f. The low spin state of Co^{3+} at the octahedral site with 6 electrons in the t_{2g} level should be stable, as shown in the upper CFSD of Figure 6.3.5f. However, in the tetrahedral site, the high spin state of Co^{4+} with 5 electrons could also be stable, as indicated in Figure 6.3.5e and the lower CFSD of Figure 6.3.5f. Therefore, both Co ions and Mn ion in the HMLO system are more favorably oxidized in the tetrahedral site during their migration from the TM layer to the Li layer. This is because of the effect of crystal field stabilization, which stabilizes the entire structure, decreases its energy state by donating electrons to surrounding O atoms, and contributes to decreasing the migration barriers faced by Mn and Co ions.

As mentioned above, in contrast, Ni ions undergo a double redox reaction from Ni^{2+} to Ni^{4+} , as explained in Figure 6.3.4d. Thus, Ni ions have a reduced character during migration from the Ni^{4+} state in the octahedral site to

the Ni³⁺ state in the tetrahedral site, as shown in Figure 6.3.5g and 6.3.5h. This is also because of the effect of the crystal field stabilization; the Ni⁴⁺ state in the octahedral site has 6 electrons in the t_{2g} level, as shown by the upper CFSD of Figure 6.3.5h. However, in the tetrahedral site, 4 electrons fill the e level of the reversed crystal field and 3 electrons fill the spin-up states in the t₂ level of the reversed crystal field, as shown in the lower CFSD of Figure 6.3.5h. Hence, Ni ions in the tetrahedral site are reduced by accepting an electron from the surrounding O atoms and are converted to the relatively stable Ni³⁺ state, as illustrated in the lower CFSD of Figure 6.3.5h. This process destabilizes the entire structure, increases its energy state by absorbing electrons from surrounding O atoms, and increases the migration barrier faced by the Ni ions. Therefore, the TMs with reduced character in the tetrahedral sites compared with the octahedral sites, such as Ni ions, will face a higher migration barrier from the TM layer to the Li layer, which could impede the phase transformation during charge-discharge processes. The effect of the high migration barrier on Ni ions will likely be generated in Li-rich and Mn-rich environments (such as the HMLO system) where the oxidation states of Mn ions are similar to the inactive 4⁺ state, and a small quantity of Ni ions are rapidly converted to the 4⁺ state at the beginning of delithiation.

As doping materials for the impeded phase transformation in the HMLO system, Cu and Zn are possible candidates because these elements could be predicted to exhibit reduced character based on the periodic table. However, Zn would be an inactive element in the HMLO system because Zn²⁺ has 10 electrons, which fill the entire d-orbitals in both octahedral and tetrahedral sites. Thus, Cu is likely a more reasonable candidate. Therefore, in this study, a Li_{1.67}Ni_{0.11}Co_{0.11}Mn_{0.67}Cu_{0.11}O_{2.67} atomic model was developed by substituting 0.11 mol of Mn with the same amount of Cu, as described in Figure 6.3.6a. As done for the atomic model of Li_{1.67}Ni_{0.11}Co_{0.11}Mn_{0.78}O_{2.67}, the

location of the Cu atom was determined by comparing the thermodynamic energies obtained *via* first-principles calculations.

The migration barriers of Cu ions from the initial octahedral sites in the TM layer to the final octahedral sites in the Li layer *via* the middle tetrahedral sites are shown in Figure 6.3.6b in terms of the inverse Li content x . At $x = 0.11$, the migration barrier of Cu ions is approximately 5.06 eV and decreases to 3.56 eV at $x = 0.33$; subsequently, it increases to 3.67 eV at $x = 0.56$ and 4.35 eV at $x = 0.78$. To characterize the reduced character of Cu ions in the HMLO system, the net charges of Cu ions at different migration positions were investigated, as represented in Figure 6.3.6c. This revealed that Cu ions exhibit relatively low net charges in the middle tetrahedral sites than at the initial and final octahedral sites. Quantitatively, Cu ions in the HMLO system have more electrons in the tetrahedral site than in both octahedral sites and exhibit a reduced character during migration. To achieve an in-depth understanding of this reduced character, Figure 6.3.6d shows the PDOS of the Cu d-orbital at the octahedral (black solid line) and tetrahedral (red dashed line) sites in $\text{Li}_{1.11}\text{Ni}_{0.11}\text{Co}_{0.11}\text{Mn}_{0.67}\text{Cu}_{0.11}\text{O}_{2.67}$, with the corresponding CFSDs presented in Figure 6.3.6f. The PDOS of the Cu d-orbital in the octahedral site indicates the existence of the Cu^{3+} state with 8 electrons, as shown by the black solid line in Figure 6.3.6d. This is because Cu^{3+} ions in the octahedral sites can be stabilized with 8 electrons: 6 electrons in the t_{2g} level and 2 electrons in the spin-up e_g level, as shown in the upper CFSD in Figure 6.3.6f. In contrast, Cu ions in the tetrahedral sites would have more electrons than those in the octahedral sites because of the decreased number of unoccupied states in the Cu d-orbital, as shown by the red dashed line in Figure 6.3.6d. This could be explained by the crystal field stabilization effect: Cu^{3+} with 8 electrons in the tetrahedral site is more unstable than that in the octahedral site, and thus, Cu^{3+} in the tetrahedral site is likely to gain more electrons and become an electronic structure between Cu^{2+} and Cu^{3+} because of the crystal

field stabilizing gained by filling the remaining unoccupied states, as illustrated in Figure 6.3.6d and 6.3.6e. This is why Cu ions with reduced character in the HMLO system were observed both quantitatively and qualitatively. Therefore, the reduction of the Cu ions in the tetrahedral sites during migration will oxidase the surrounding O ions and make the entire structure unstable, increasing its energy state and the migration barrier faced by Cu ions from the TM layer to the Li layer and potentially impede the phase transformation of the HMLO system.

In summary, the synergistic role and the enhanced cyclic stability related to the impeded interlayer migration of TMs during high-voltage operation of HMLO can be fundamentally understood in terms of the crystal field stabilization, as shown both experimentally and theoretically. Mechanically blended m-HMLO and chemically bonded c-HMLO were characterized by XRD, FESEM, STEM with SAED and EDS. c-HMLO shows enhanced cyclic stability with a discharge capacity retention of ~99 % after 50 cycles of high-voltage operation at ~4.8 V vs. Li/Li⁺, while m-HMLO exhibits a discharge capacity retention of ~62 % under the same conditions. Moreover, the reaction voltages of c-HMLO are approximately 0.5 V vs. Li/Li⁺ higher than those of m-HMLO, and the charge and discharge specific capacities of c-HMLO are more than three times larger than those of m-HMLO after 50 cycles.

The affirmative effects described above were fundamentally elucidated using theoretical approaches *via* first-principles calculations based on the electronic structures in terms of the crystal field stabilization. To achieve reasonable atomic calculation modelling of the as-prepared c-HMLO powder, Rietveld refinement was applied, and the agreement between the atomic model and as-synthesized c-HMLO was validated by the weighted R profile factor: 3.767. From the reaction mechanism based on this atomic model, it was revealed that the NCM component would stabilize the TM layer of

HMLO and could help the structural stability of Li_2MnO_3 . TM migration analyses with electronic structures quantitatively and qualitatively revealed the redox character of the TMs during migration from the TM layer to the Li layer. Unlike the Mn and Co ions, which exhibit oxidized character, Ni ions show a reduced character, which takes electrons from surrounding O ions, thereby oxidizing them, to stabilize the crystal field of the Ni ions in the tetrahedral sites. In other words, oxidizing the O atoms make the entire HMLO system unstable, increasing its energy state and the migration barriers of Ni ions and thereby impeding the phase transformation. Based on the crystal field stabilization mechanisms found here, Cu ions are suggested as a doping source to suppress phase transformation and improve cyclic stability by increasing the migration barriers faced by TMs.

Based on these findings relating to the effect of crystal field stabilization on impeded interlayer migration of TMs, it could be understood that a small amount of NCM would stabilize a large amount of inactive Li_2MnO_3 in Li-rich oxides. Moreover, this study provides fundamental insights into enhancing the cyclic stability by designing various Li-rich and Mn-rich layered oxide cathodes.

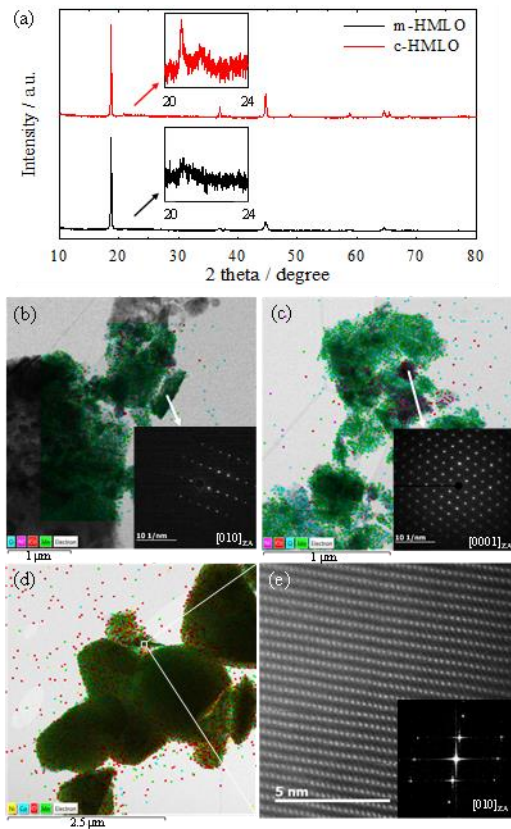


Figure 6.3.1 (a) Powder XRD patterns of m-HMLO (black solid line) and c-HMLO (red solid line). Enlarged insets represent superlattice peaks indexed to the (020) and (110) planes from 20° to 24° . (b, c) STEM images of as-prepared m-HMLO with EDS elemental mapping of Mn (green), O (cyan), Ni (purple), and Co (red) and corresponding SAED patterns for Li_2MnO_3 with a zone axis of $[010]$ (inset of b) and $\text{LiNi}_{1/3}\text{Co}_{1/3}\text{Mn}_{1/3}\text{O}_2$ with a zone axis of $[0001]$ (inset of c). (d, e) STEM images of as-prepared c-HMLO with EDS elemental mapping of Mn (green), O (red), Ni (yellow), and Co (cyan) at (d) low magnification, and STEM image of c-HMLO at (e) high magnification with corresponding FFT pattern and a zone axis of $[010]$ (inset of e).

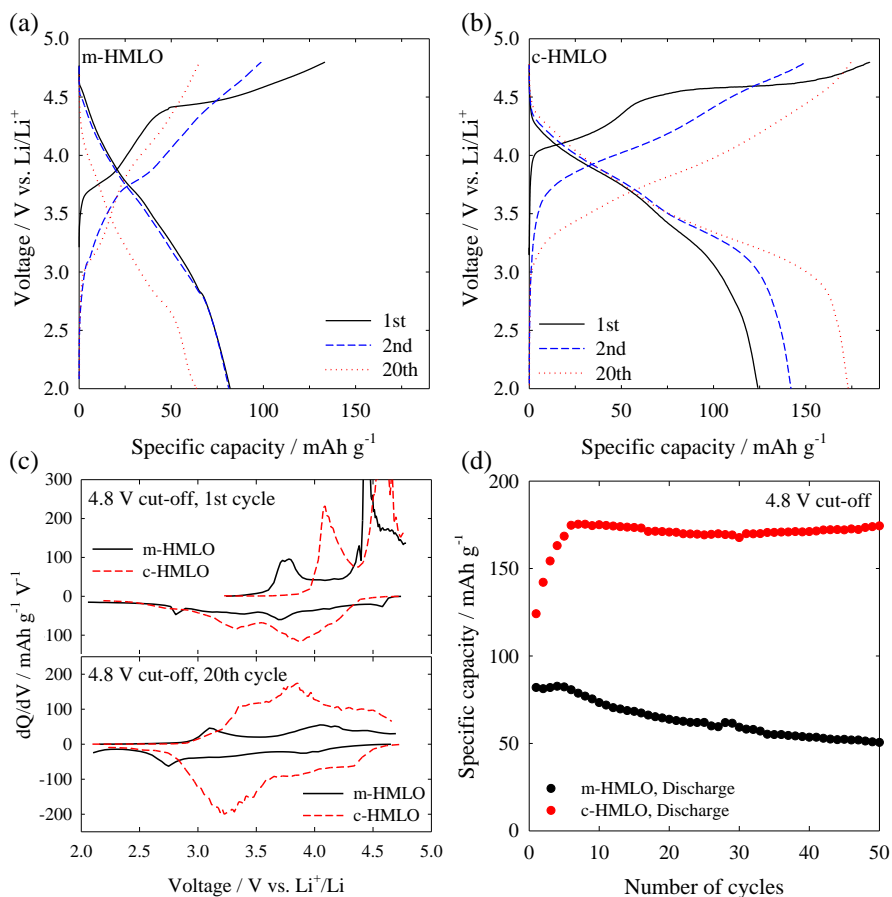


Figure 6.3.2 (a, b) Galvanostatic charge-discharge profiles of as-prepared (a) m-HMLO and (b) c-HMLO recorded in CC mode with a constant specific current of 25 mA g^{-1} in the voltage range between 2.0 and 4.8 V vs. Li/Li⁺ at the 1st, 2nd, and 20th cycles. (c) Corresponding dQ/dV curves of m-HMLO (black solid line) and c-HMLO (red dashed line) at the 1st (upper) and 20th (lower) cycles. (d) Comparison of the discharge cyclic performances of m-HMLO (black circle) and c-HMLO (red circle).

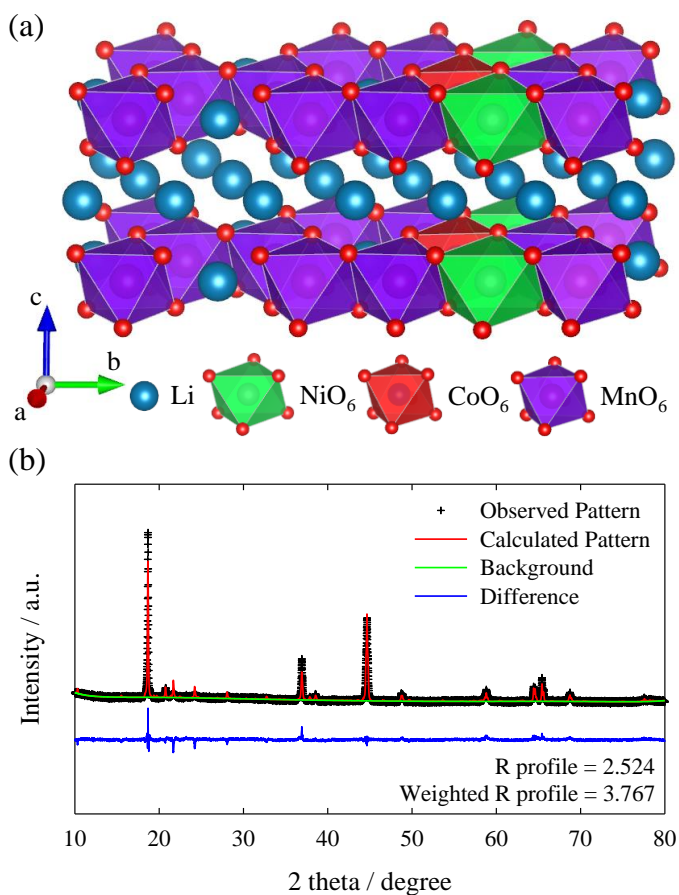


Figure 6.3.3 (a) Atomic model of $\text{Li}_{1.67}\text{Ni}_{0.11}\text{Co}_{0.11}\text{Mn}_{0.78}\text{O}_{2.67}$ (space group: $C2/m$). (b) Rietveld refinement of the XRD pattern of as-synthesized c-HMLO using the atomic model (a).

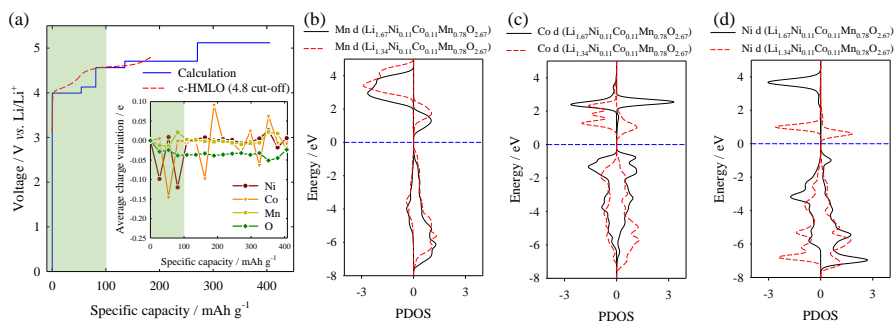


Figure 6.3.4 (a) Calculated voltage (blue solid line) with respect to the specific capacity predicted by the Li concentration and the 1st charge profile of the c-HMLO from Figure 6.3.2b. Average charge variations of Ni, Co, Mn, and O ions (inset of (a)) according to the calculated voltage. (b, c, d) PDOS for (b) Mn, (c) Co, and (d) Ni d-orbitals of $\text{Li}_{1.67}\text{Ni}_{0.11}\text{Co}_{0.11}\text{Mn}_{0.78}\text{O}_{2.67}$ (black solid line) and $\text{Li}_{1.34}\text{Ni}_{0.11}\text{Co}_{0.11}\text{Mn}_{0.78}\text{O}_{2.67}$ (red dashed line), where the Fermi level is 0.0 eV (blue dashed line).

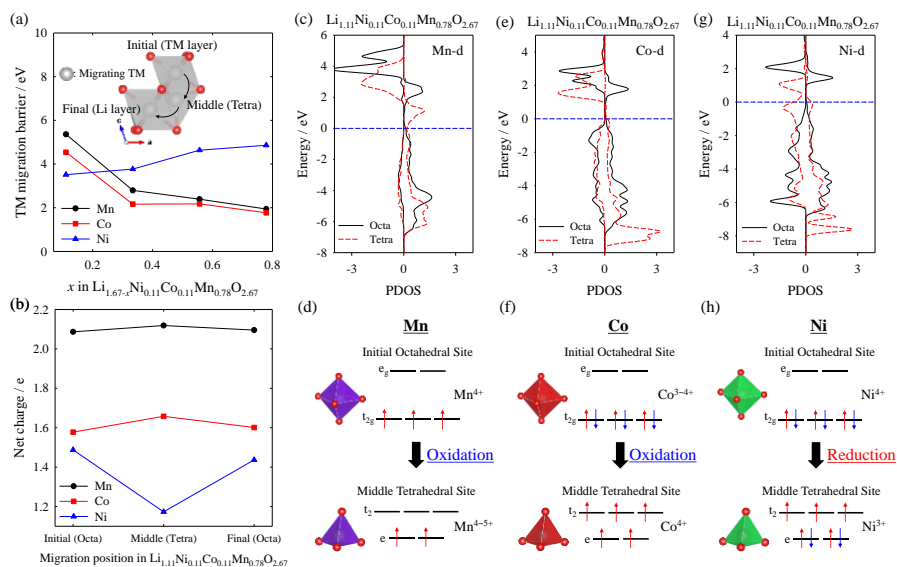


Figure 6.3.5 (a) Migration barriers of Mn (black circle), Co (red square), and Ni (blue triangle) ions in terms of the inverse Li content x in $\text{Li}_{1.67-x}\text{Ni}_{0.11}\text{Co}_{0.11}\text{Mn}_{0.78}\text{O}_{2.67}$ from the initial TM layer to the final Li layer *via* the middle tetrahedral site (inset). (b) Net charges of Mn (black circle), Co (red square), and Ni (blue triangle) ions in the three different migration sites (inset of (a)). (c, e, g) PDOS for (c) Mn, (e) Co, and (g) Ni d-orbitals in the initial octahedral site (black solid line) and middle tetrahedral site (red dashed line) for $\text{Li}_{1.11}\text{Ni}_{0.11}\text{Co}_{0.11}\text{Mn}_{0.78}\text{O}_{2.67}$, where the Fermi level is 0.0 eV (blue dashed line). (d, f, h) Corresponding CFSDs of (d) Mn, (f) Co, and (h) Ni d-orbitals in the initial octahedral site (upper) and middle tetrahedral site (lower) for $\text{Li}_{1.11}\text{Ni}_{0.11}\text{Co}_{0.11}\text{Mn}_{0.78}\text{O}_{2.67}$.

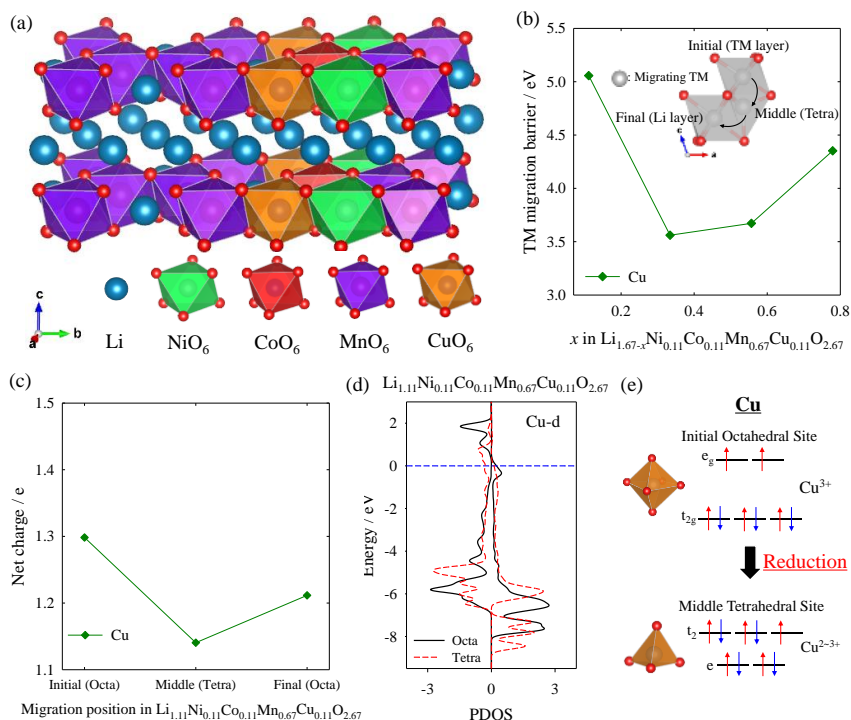


Figure 6.3.6 (a) Atomic model of $\text{Li}_{1.67}\text{Ni}_{0.11}\text{Co}_{0.11}\text{Mn}_{0.67}\text{Cu}_{0.11}\text{O}_{2.67}$ (space group: $C2/m$). (b) Migration barriers of Cu ion (green diamond) in terms of the inverse Li content x in $\text{Li}_{1.67-x}\text{Ni}_{0.11}\text{Co}_{0.11}\text{Mn}_{0.67}\text{Cu}_{0.11}\text{O}_{2.67}$ from the initial TM layer to the final Li layer *via* the middle tetrahedral site (inset). (c) Net charges of Cu ions (green diamond) at the three different migration sites (inset of (b)). (d) PDOS for Cu d-orbitals in the initial octahedral site (black solid line) and middle tetrahedral site (red dashed line) for $\text{Li}_{1.67}\text{Ni}_{0.11}\text{Co}_{0.11}\text{Mn}_{0.67}\text{Cu}_{0.11}\text{O}_{2.67}$, where the Fermi level is 0.0 eV (blue dashed line). (e) Corresponding CFSDs of Cu d-orbital in the initial octahedral site (upper) and middle tetrahedral site (lower) for $\text{Li}_{1.67}\text{Ni}_{0.11}\text{Co}_{0.11}\text{Mn}_{0.67}\text{Cu}_{0.11}\text{O}_{2.67}$.

6.4 p-type Conductivity in High-Mn, Li-rich Oxides[22]

For further development of the high-Mn, Li-rich oxides (HMLOs) before we introduced in Section 6.3, we improved intrinsic electronic conductivity of HMLOs by introducing p-type conductivity, which was based on fundamental understanding through first-principles electronic structure analysis with experimental observations. In our previous report as explained in Section 6.3 on the underlying mechanism of phase transformation for HMLO,[21] Cu-doping was suggested to impede the phase transformation in Li-rich oxides and therefore enhance the cyclic degradation. During a subsequent experimental investigation on Cu-doping in HMLO, we have obtained a relatively good cyclic retention, and also observed intrinsic p-type conductivity, which enhanced both the specific energy and the power characteristics. Although the Cu-doped HMLO (CuHMLO) has an identical crystal structure to the original HMLO, the electrochemical performance of CuHMLO is superior in terms of specific energy and power characteristics. Specifically, CuHMLO exhibits a larger specific capacity with enhanced rate capability, and could be charged at lower voltages and discharged at higher voltages. For the first-principles calculations, HMLO and CuHMLO structures are modeled based on Rietveld refinement of the powder X-ray diffraction (XRD) data of the powders synthesized herein. The electronic structure of CuHMLO reveals the generation of an electron hole in the valance band, above the Fermi level, indicating p-type conductivity and improving the electronic conductivity. The interpretation based on the crystal field theory elucidates that the generation of this electron hole is responsible for the relatively reduced character of Cu than Mn in the highly oxidized HMLO environment. Combination of this observed enhancement with a fundamental understanding on the origin of the p-type conductivity could assist in improving the specific energy and power characteristics of Li-rich oxides.

Figure 6.4.1 shows the powder XRD patterns of HMLO and CuHMLO, and the HRTEM image of CuHMLO with EDS elemental mapping results of Ni, Co, Mn, O, and Cu. As shown in Figure 6.4.1a, the XRD patterns of both HMLO and CuHMLO exhibited the monoclinic layered structure of the $C2/m$ space group (JCPDS 84-1634) with superlattice peaks that were indexed to the (020) and (110) planes from 20° to 24° , which originated mainly from Li_2MnO_3 . [21] In addition, the particle sizes and morphologies of HMLO and CuHMLO were comparable. [22] Figure 6.4.1b shows a HRTEM image of CuHMLO combined with EDS elemental mapping results, which indicates homogeneous distribution of the TM elements in the structure. Furthermore, the elemental ratio of Li:Ni:Co:Mn:Cu in the CuHMLO was confirmed as 1.6106:0.1195: 0.1078:0.7493:0.0235 using ICP-MS analysis. These results are in agreement with the target compositions of both HMLO (0.11:0.11:0.78) and CuHMLO (0.11:0.11:0.75:0.028).

To obtain detailed structural information, high magnification STEM images of HMLO and CuHMLO were examined with their corresponding fast Fourier Transform (FFT) patterns. Figure 6.4.2a and 6.4.2d show the fine atomic arrangements of HMLO and CuHMLO, respectively. The corresponding FFT pattern of HMLO can be seen in Figure 6.4.2b, which shows a zone axis of [010], and d -spacings of 0.49 nm and 0.24 nm for the (001) and (200) planes, respectively, with an angle of 72.01° . Similarly, the FFT pattern of CuHMLO (Figure 6.4.2e) with a zone axis of [0-10] indicates d -spacings of 0.49 nm and 0.24 nm for the (001) and (200) planes, respectively, with an angle of 72.60° . Furthermore, we investigated the ideal crystal structures of HMLO and CuHMLO along the same direction in the STEM images (Figure 6.4.2a and 6.4.2d), which shows agreeable atomic structures with calculated atomic models in Figure 6.4.2c and 6.4.2f, respectively. Slightly smaller values of the d -spacings for the (001) and (200) planes in the atomic models can be reasonably explained by the

underestimated angles of both HMLO and CuHMLO structures. Based on these characterizations, we could conclude that the synthesized HMLO and CuHMLO exhibited similar crystal structures, atomic arrangements, and structural parameters, along with homogeneous elemental distributions of the target compositions.

For comparison, electrochemical measurements were conducted for the prepared HMLO and CuHMLO electrodes. Figure 6.4.3a and 6.4.3b show the galvanostatic charge-discharge profiles of HMLO and CuHMLO for the 1st and 10th cycles between 2.0 and 4.8 V *vs.* Li/Li⁺, with a constant current of 25 mA g⁻¹. In the first cycle, the specific charge and discharge capacities of CuHMLO were measured to be 226.7 and 157.5 mAh g⁻¹, respectively, which values are larger than those of HMLO by ~35 mAh g⁻¹. Interestingly, CuHMLO exhibited a relatively lower voltage during charge and a higher voltage during discharge compared with HMLO. This indicates that the specific energy can be improved by the quantity represented by the shaded area in Figure 6.4.3a. Similar electrochemical behaviors were observed in the 10th cycle (Figure 6.4.3b), where CuHMLO showed larger specific capacities and reduced overpotential during cycle demonstrating an enhancement in specific energy. These results confirm that the CuHMLO cathode can be charged using a smaller electrical energy (i.e., charge) than HMLO, and can exhibit a greater electrical energy (i.e., discharge) leading to improved energy storage efficiency.

In terms of cycle performance, good cyclic retentions were observed for both HMLO and CuHMLO at constant currents of 40 mA g⁻¹ (Figure 6.4.3c) and 100 mA g⁻¹ (Figure 6.4.3d), respectively (between 2.0 and 4.8 V *vs.* Li/Li⁺), which can be reasonably explained by the reduced character of TMs during the redox reactions, because the reduced character of the TMs is responsible for impeding phase transformations by increasing migration barriers of TMs from TM layers to Li layers.[21]

In addition, the power characteristics of CuHMLO were also superior to those of HMLO. At a specific current of 40 mA g^{-1} , the difference in specific capacities between HMLO and CuHMLO was estimated to be $\sim 10 \text{ mAh g}^{-1}$, while at a specific current of 100 mA g^{-1} , this difference increased to around 30 mAh g^{-1} , without significant capacity fading during cycles. Even at higher current densities up to 400 mA g^{-1} (Figure 6.4.3e), the rate capability of CuHMLO was superior to that of HMLO, and the difference in specific capacities between HMLO and CuHMLO gradually increasing with an increase in specific current density. From the electrochemical experiments, we emphasize that CuHMLO exhibits both enhanced specific energies and power characteristics compared with HMLO. These superior properties were accompanied by good cyclic retention.

To understand the origins and mechanism of the superior characteristics of CuHMLO compared to HMLO, first-principles electronic structure analyses were performed. Initially, atomic models were established for HMLO and CuHMLO by comparing the calculated XRD patterns with Rietveld refinement using the XRD patterns of the prepared HMLO and CuHMLO electrodes. Figure 6.4.4a and 6.4.4b show the developed atomic models for 36 *f.u.* of HMLO and CuHMLO with chemical formulae of $\text{Li}_{1.67}\text{Ni}_{0.11}\text{Co}_{0.11}\text{Mn}_{0.78}\text{O}_{2.67}$ and $\text{Li}_{1.67}\text{Ni}_{0.11}\text{Co}_{0.11}\text{Mn}_{0.75}\text{Cu}_{0.028}\text{O}_{2.67}$, respectively. TM locations were determined by first-principles thermodynamic comparisons,[21] and the Rietveld refinements were performed based on the large atomic models (36 *f.u.* with 192 atoms). Thus, according to the Rietveld refinement analyses shown in Figure 6.4.4c and 6.4.4d, monoclinic structures with a $C2/m$ space group were established, and the agreement indices of the R profiles and weighted R profiles were 6.4135 and 9.7822 for HMLO, and 6.4842 and 9.4993 for CuHMLO, respectively. Thus, as indicated by the STEM images and the FFT patterns shown previously in Figure 6.4.2, the results of the Rietveld refinement and the DFT calculations confirm that

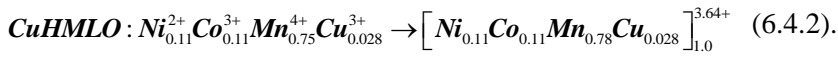
HMLO and CuHMLO exhibit comparable crystal structures.

Based on these atomic models, we have investigated the electronic properties of HMLO and CuHMLO by analyzing their electronic structures through DFT calculations (see Figure 6.4.5 and 6.4.6). Figure 6.4.5 shows the total density of states (TDOS) for HMLO and CuHMLO, which indicates that the Fermi level of HMLO is located in the middle of the band gap. In comparison, the Fermi level of CuHMLO is located at the top of valence band, indicating the generation of an electron hole consistent with its p-type conductivity. This confirms that the p-type conductivity caused by the generation of an electron hole improves the electronic conductivity of CuHMLO, thus improving its specific energy and enhancing its power characteristics.

We have also examined the partial (projected) density of states (PDOS) for TMs (Figure 6.4.6) to elucidate the origins and mechanism of this p-type conductivity. Figure 6.4.6a, 6.4.6b, and 6.4.6c show the PDOSs for the Ni, Co, and Mn d-orbitals of HMLO, respectively. The shapes of the PDOSs indicate the oxidation states of the Ni²⁺, Co³⁺, and Mn⁴⁺ species, as represented by the crystal field splitting diagrams (CFSDs) in Figure 6.4.6h, 6.4.6i, and 6.4.6j, respectively. As expected, in a similar manner to the TDOS (Figure 6.4.5a) the Fermi level is located in the middle of the band gap. However, the PDOSs of the Ni, Co, Mn, and Cu d-orbitals (Figure 6.4.6d, 6.4.6e, 6.4.6f, and 6.4.6g) indicate that the Fermi level has moved towards the valence band, even though the electronic states of the Ni²⁺, Co³⁺, and Mn⁴⁺ in CuHMLO are similar to those of HMLO.

As the TMs have stable chemical states due to both the crystal field stabilization[21] and the effect of the *d* electronic donor,[11, 38, 60] the Mn ion in both HMLO and CuHMLO adopts the stable Mn⁴⁺ state with the electron configuration of $t_{2g}^3 e_g^0$. This highly oxidized Mn⁴⁺ environment allows Ni and Co to maintain their stable crystal fields through the Ni²⁺ (t_{2g}^6

e_g^2) and Co^{3+} ($t_{2g}^6 e_g^0$) configurations, as shown in Figure 6.4.6h, 6.4.6i, and 6.4.6j. When Cu is substituted at Mn site through Cu-doping, Cu remains in its relatively reduced Cu^{3+} state (compared to Mn^{4+}) in this highly oxidized environment, i.e., a stable crystal field in the octahedral geometry, as indicated in Figure 6.4.6g and 6.4.6k. Note that Cu^{3+} state is higher oxidation state of Cu than usual 1+ or 2+ states. Based on these nominal charge states of the TMs, the total charge of the TMs in HMLO and CuHMLO can be calculated as follows:



Since the total charged state of the TMs in HMLO and CuHMLO is $\text{TM}^{3.67+}$ ($\text{Li}^{1+}_{1.67} \text{TM}^{3.67+} \text{O}^{2-}_{2.67}$), Ni, Co, and O atoms in CuHMLO would be further oxidized to increase the TM oxidation from 3.64+ to 3.67+, as shown in Equation 6.4.1 and 6.4.2. Thus, the valence state of CuHMLO has moved upward in energy, generating an electron hole above the Fermi level, as outlined in Figure 6.4.5b, 6.4.6d, 6.4.6e, 6.4.6f, and 6.4.6g. This electron hole results in the observed p-type conductivity and improves the electronic conductivity of CuHMLO, thus accounting for the lower charge voltage, higher discharge voltage, and enhanced rate capability observed in the electrochemical measurements. We have also measured the electronic conductivity of pelletized HMLO and CuHMLO powders using a four-point probe method (Loresta-GP MCP-T610, Mitsubishi Chemical) to experimentally validate the enhanced electronic conductivity of CuHMLO. From the results, a noticeable improvement in electronic conductivity was observed for CuHMLO ($\sim 4.125 \times 10^{-6} \text{ S cm}^{-1}$) compared with HMLO ($\sim 2.924 \times 10^{-7} \text{ S cm}^{-1}$), indicating that the p-type conductivity induced by incorporation of Cu would be effective for improving the electronic conductivity.

In summary, based on a combination of experimental and theoretical approaches, we herein report the generation of p-type conductivity from the creation of an electron hole in high-Mn and Li-rich environments through the introduction of Cu doping. The prepared high-Mn, Li-rich oxide (HMLO) and Cu-doped HMLO (CuHMLO) materials exhibited similar crystal structures and comparable structural parameters, as demonstrated by both experimental and theoretical studies. Despite this structural similarity, CuHMLO exhibited significantly enhanced electrochemical performances compared to HMLO. Importantly, with its larger specific capacity, CuHMLO can be charged at lower voltages and discharged at high voltages than HMLO, thus enhancing its specific energy efficiency. Furthermore, it was evident that CuHMLO exhibited enhanced power characteristics. From the first-principles electronic structure investigations based on atomic models developed using Rietveld refinements, the generation of an electron hole was observed in the valance band, above the Fermi level in CuHMLO, thus indicating p-type conductivity. Interpretations based on the crystal field theory have indicated that this p-type conductivity was generated by the highly reduced character of Cu in the highly oxidized HMLO environment. Thus, based on the enhanced characteristics and the elucidated mechanism, a design strategy could therefore be suggested to improve the specific energy and power characteristics through enhancement of the electronic conductivity using p-type conductivity in Li-rich oxide systems.

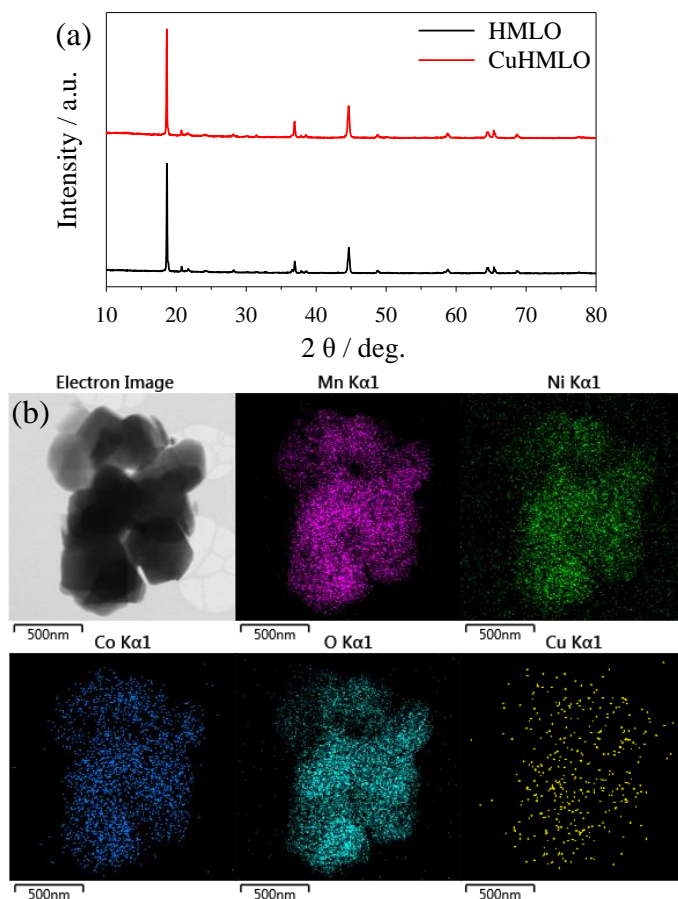


Figure 6.4.1 (a) Powder XRD patterns of HMLO (black solid line) and CuHMLO (red solid line). (b) HRTEM image of CuHMLO with EDS elemental mapping of Ni (green), Co (blue), Mn (purple), Cu (yellow), and O (cyan).

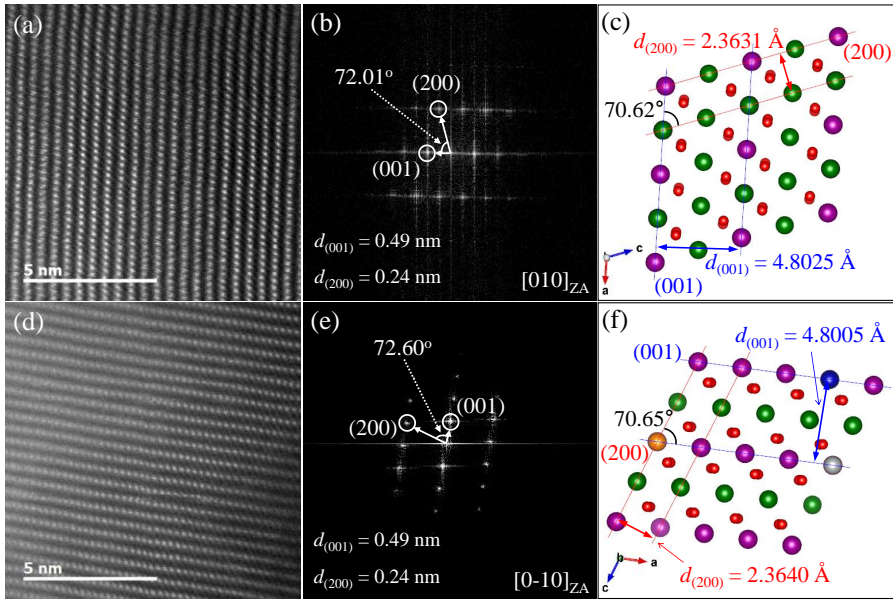


Figure 6.4.2 High magnification STEM images of (a) HMLO and (d) CuHMLO with the corresponding FFT patterns of (b) HMLO with a zone axis of $[010]_{ZA}$ and (e) CuHMLO with a zone axis of $[0-10]_{ZA}$. Ideal crystal structures along the same directions with the STEM images of (c) HMLO and (f) CuHMLO obtained by first-principles calculations.

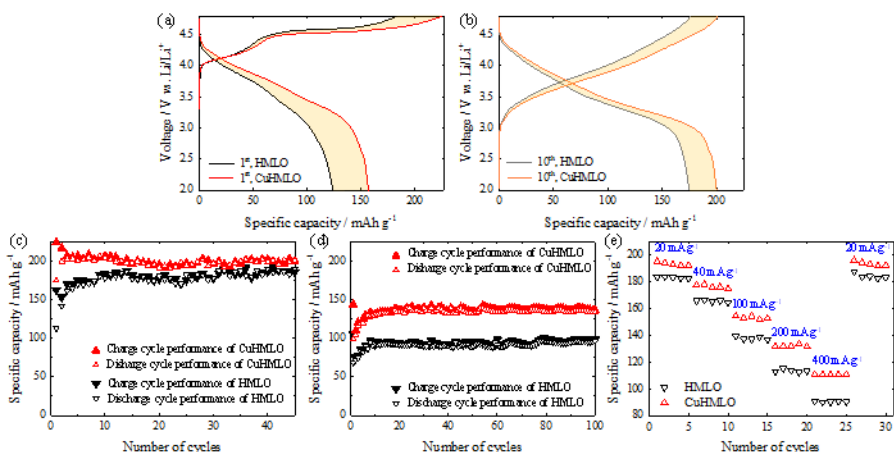


Figure 6.4.3 (a, b) Galvanostatic charge-discharge profiles of the prepared HMLO (black solid line) and CuHMLO (red solid line) between 2.0 and 4.8 V vs. Li/Li⁺ with a constant specific current of 25 mA g⁻¹ in the (a) 1st and (b) 10th cycles. (c, d) Charge (bold triangles) and discharge (hollow triangles) cycle performances of HMLO (black inverse triangles) and CuHMLO (red triangles) with constant specific currents of (c) 40 mA g⁻¹ and (d) 100 mA g⁻¹ between 2.0 and 4.8 V vs. Li/Li⁺. (e) Rate capability of the discharge specific capacity between 20 mA g⁻¹ and 400 mA g⁻¹ for HMLO (black inverse triangles) and CuHMLO (red triangles).

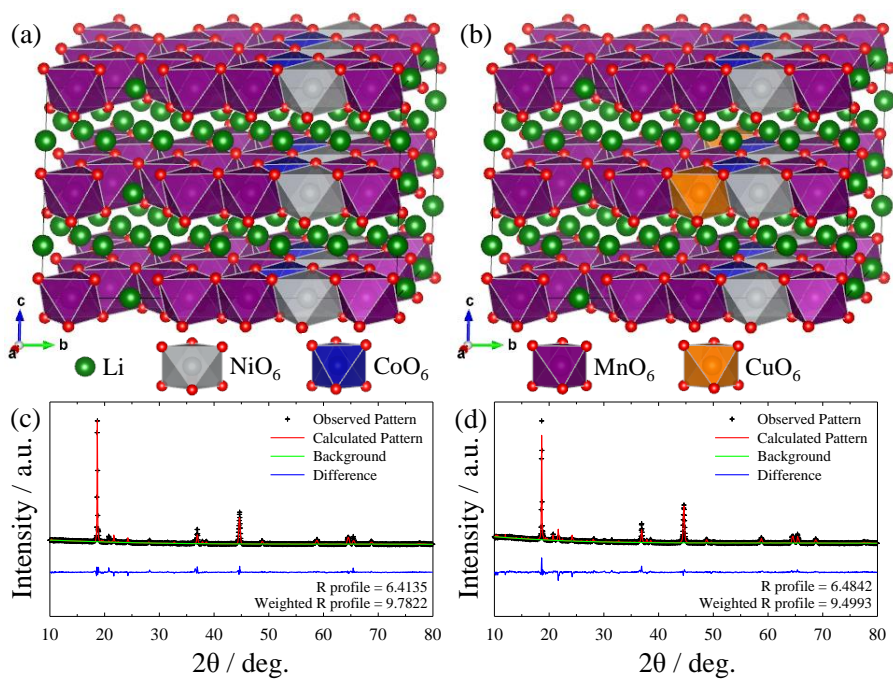


Figure 6.4.4 (a, b) Atomic models of (a) HMLO and (b) CuHMLO (space group: $C2/m$). (c, d) Rietveld refinements of the XRD patterns of (c) HMLO and (d) CuHMLO using the atomic models in parts (a) and (b), and the agreement indices of the R profile and the weighted R profile factors.

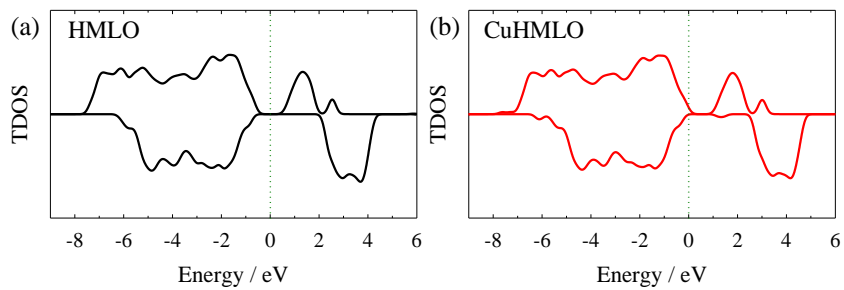


Figure 6.4.5 Total density of states (TDOS) of (a) HMLO and (b) CuHMLO.

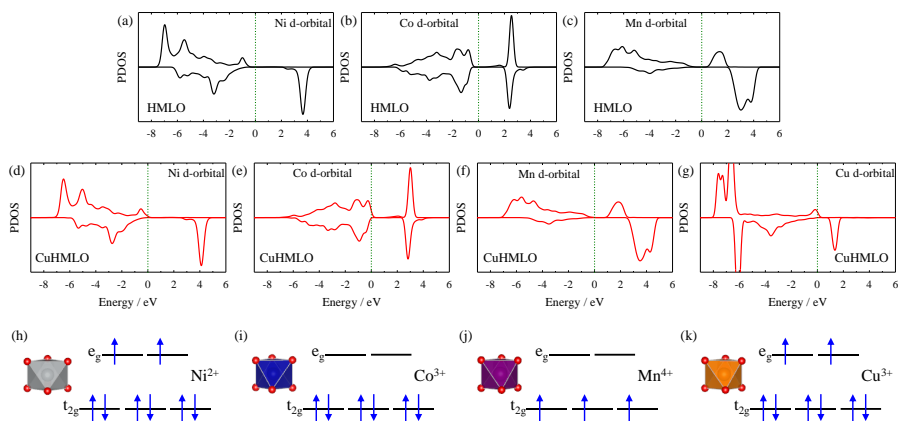


Figure 6.4.6 (a, b, c) Partial (projected) density of states (PDOS) for the (a) Ni, (b) Co, and (c) Mn d-orbitals of HMLO (black solid lines) in their fully-lithiated states. (d, e, f, g) PDOS for the (d) Ni, (e) Co, (f) Mn, and (g) Cu d-orbitals of CuHMLO (red solid lines) in their fully-lithiated states. (h, i, j, k) Corresponding crystal field splitting diagrams (CFSDs) for the (h) Ni, (i) Co, (j) Mn, and (k) Cu d-orbitals in the octahedral sites for HMLO and CuHMLO.

6.5 Doping Effects on Phase Separation in Spinel LiMn_2O_4 [23]

A multiscale computational approaches is conducted to propose a theoretical solution for the suppression of the severe cyclic degradation in spinel LiMn_2O_4 cathode. Based on the our previous report,[23] the electrochemical performance of the Al-doped sample shows enhanced cyclic performance than that of the pristine one. A multiscale phase field model in nanodomain shows that the phase separation of the pristine spinel occurs to inactive $\text{Li}_0\text{Mn}_2\text{O}_4$ (i.e. fully delithiated) gradually during cycles. In contrast, the Al-doped spinel does not show phase separation to an inactive phase. This is why the Al-doped spinel maintains the capacity of the first charge during the subsequent cycles. Based on these mechanistic understanding of the origins and mechanism on the suppression of the phase transformations to an inactive phase, fundamental insight for making tremendous cuts in the cyclic degradation could be provided for the Li-Mn-O compounds of Li-ion batteries.

The multiscale modeling on the phase transformation, which is a bridged methodology from first-principles calculation to the multiscale phase separation kinetics, was adopted to understand the enhanced cyclic performance of LMAO in terms of a mesoscale phase transformation.[1, 26]

The qualitative phase behaviors of LMO and LMAO can be predicted based on zero-temperature mixing enthalpy shown in Figure 6.5.1. Figure 6.5.1a describes the 4 ground states of LMO at $x = 0.0, 0.125, 0.375,$ and 1.0 . From $x = 0.375$ to 1.0 , a two-phase reaction would occur in LMO, and LMO could be transformed to an irreversible $\text{Li}_0\text{Mn}_2\text{O}_4$ phase (e.g., L_0MO), which causes cyclic degradation. On the other hand, LMAO has two additional ground states at $x = 0.625,$ and 0.875 , which could prevent the transformation to L_0MAO . For detailed analysis of the phase behaviors, Figure 6.5.2 shows the homogeneous bulk free energy f_h and chemical potential $-\mu_i/e$ of LMO and LMAO at room temperature, and the spinodal points are represented as black dotted lines for LMO ($x = 0.18, 0.32, 0.51,$ and 0.85) and blue dotted

lines for LMAO ($x = 0.33, 0.54, 0.68, \text{ and } 0.82$). Figure 6.5.2a and 6.5.2c shows that phase separation is likely to occur in LMO because the SOC of the first charge of LMO (82.8%) is between the spinodal points (light gray area in Figure 6.5.2a and 6.5.2c), which is in the stable two-phase reaction region. In contrast, the SOC of the first charge of LMAO (64.4%) is outside of the spinodal regions in Figure 6.5.2b and 6.5.2d, which is an unstable nucleation region, meaning that the two-phase reactions could not be generated.

From the phenomenological descriptions of the phase separation kinetics presented in Figure 6.5.3, the better cyclic performance of LMAO could be understood by a phase separation phenomenon. Both phase separation simulations were performed with 256×256 computational cell using a solid solution at state of charge (SOC) of the first charge (LMO: 82.8% and LMAO: 64.4%), and phase separation was triggered by random noise. We took a nearest-neighbor distance for the characteristic lengths (LMO: 0.3591 nm, LMAO: 0.3601 nm), and utilized the square-shaped nanodomains with the side of 91.93 nm for LMO and 92.19 nm for LMAO, as described in Figure 6.5.3. After the first charge process, the phase of LMO was separated to $L_{0.625}\text{MO}$ and $L_0\text{MO}$, which caused irreversible MnO_2 phase generation, as shown in Figure 6.5.3a. In contrast, Figure 6.5.3b shows that phase separation did not occur in LMAO after the first charge process. This is because of the existence of a ground state at approximately $x = 0.625$, shown in Figure 6.5.2b. Because LMAO reacts until an SOC of 64.4% is achieved at 4.3 V vs. Li/Li^+ in the electrochemical experiment,[23] $L_{0.356}\text{MAO}$ would remain at around $x = 0.625$ rather than separate to $L_{0.375}\text{MAO}$ and $L_{0.125}\text{MAO}$, which prevents an change of inactive $\text{Li}_0\text{Mn}_2\text{O}_4$ phase. From the different phase separation kinetics of LMO and LMAO, better cyclic performance of LMAO could be understood in terms of the mesoscale phase behaviors.

In summary, multiscale modeling were performed to obtain a fundamental understanding of the suppression of the cyclic degradation by Al

doping. The electrochemical properties of as-synthesized LMO showed a decreasing capacity after cycling, while the cycle performance of LMAO was retained during cycling. To examine the origins and mechanism of electrochemically improved properties, multiscale approaches from first-principles calculations to phase field model have been performed. Based on this mechanistic understanding, the multiscale phase separation kinetics showed that the phase separation of $L_{0.828}MO$ to $L_{0.625}MO$ and L_0MO causes an irreversible phase transformation to the inactive $Li_0Mn_2O_4$ phase. In contrast, LMAO has a stable ground state at $x = 0.625$ ($L_{0.375}MAO$), which would prevent the transformation to the inactive phase. Finally, mesoscale phase separation behaviors could help to predict and improve the cyclic performances in newly designed cathode materials for LIBs.

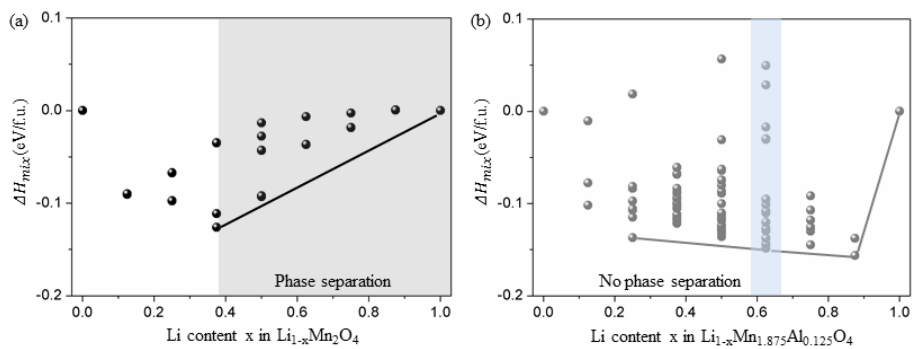


Figure 6.5.1 Zero-temperature mixing enthalpy calculated from first-principles calculations in (a) $L_{1-x}MO$ (black circles) and (b) $L_{1-x}MAO$ (gray circles) from $x = 0$ to 1.

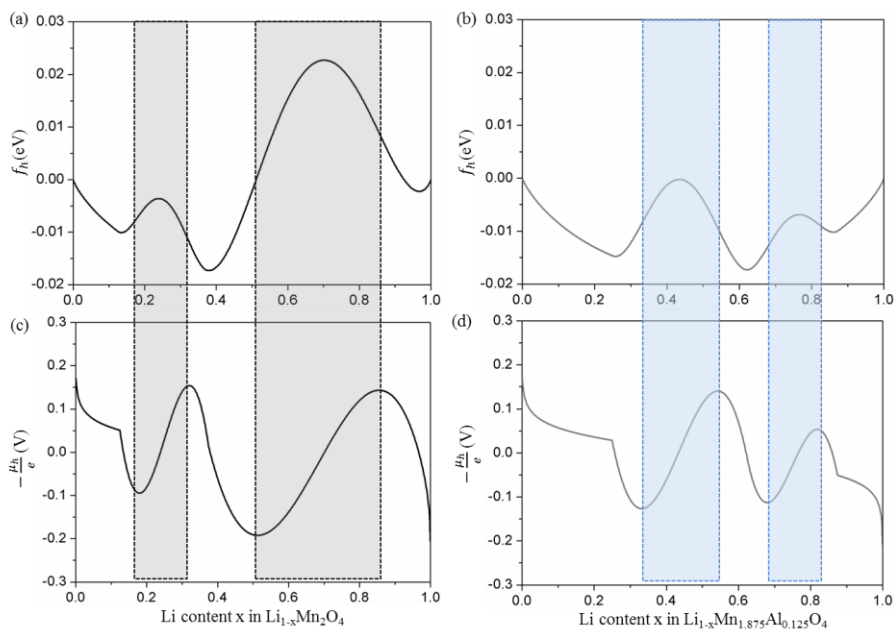


Figure 6.5.2 Homogeneous bulk free energy f_h of (a) LMO and (b) LMAO, and the chemical potential $-\mu_h/e$ of (c) LMO and (d) LMAO at room temperature with respect to the inverse Li content x . The black dashed lines in (a) and (c) are the spinodal points of LMO and the blue dashed lines in (b) and (d) are the spinodal points of LMAO.

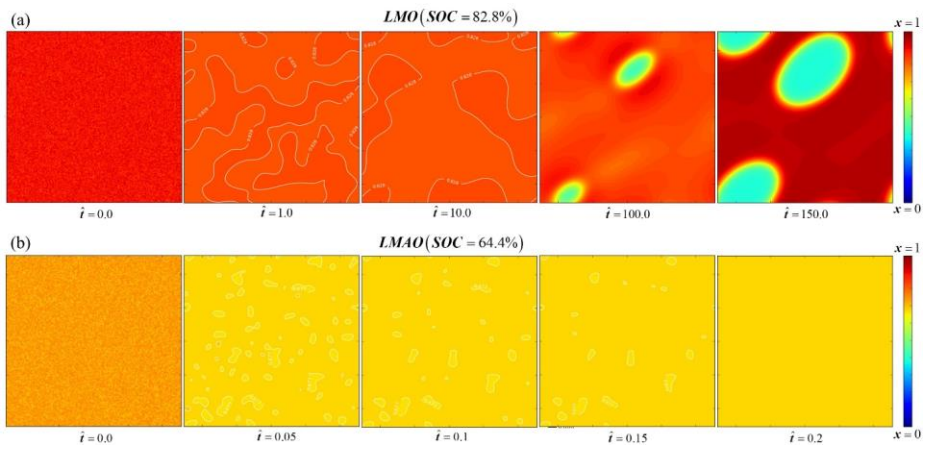


Figure 6.5.3 Phase separation kinetics in (a) LMO (SOC = 82.8%) and (b) LMAO (SOC=64.4%) during relaxation from a solid solution at various dimensionless time \hat{t} .

6.6 Surface Doping for High-voltage Spinel $\text{LiNi}_{0.5}\text{Mn}_{1.5}\text{O}_4$ [24]

High-voltage spinel oxides ($\text{LiNi}_{0.5}\text{Mn}_{1.5}\text{O}_4$, LNMO) have been extensively investigated as potential cathode materials for advanced lithium-ion batteries (LIBs) in large-scale energy storage applications.[61, 62] LNMO, along with the commercial spinel LiMn_2O_4 (LMO), has received much attention as a promising candidate material for automotive applications, such as electric vehicles (EVs), owing to its high operating voltage (4.75 V vs. Li/Li^+) and excellent rate capability. However, LNMO suffers from poor cyclic performance during high-temperature operation---a major technical challenge for its successful commercialization.[63, 64]

It is well known that the severe cyclic degradation of LNMO is mainly a result of the dissolution of transition metals (TMs) present in the structure, especially manganese, during cycles. In particular, hydrofluoric acid generated by electrolyte oxidation accelerates the dissolution of Mn^{2+} . [41, 65] To solve this problem, many structural modifications of LNMO have been attempted, such as elemental substitutions, surface coatings, and electrolyte modifications.[38, 63, 64, 66, 67]

In this respect, a surface-doping approach has been proposed to suppress the dissolution of Mn in spinel LMO.[68] It was claimed that surface-doping is more effective for reducing TM dissolution without performance fading, compared with bulk doping and surface coating approaches. Despite all these efforts, the mechanism of TM dissolution remains unresolved, and a fundamental solution for this challenge is yet to be found. Therefore, it is imperative to elucidate the origin and mechanism of TM dissolution at the surface of LNMO, to suppress TM dissolution in spinel compounds.

To develop atomic scale understanding, we investigated the TM dissolution mechanism in the LNMO cathode material, based on first-principles predictions of surface models. The electronic structures of nickel

and manganese ions at the surface of LNMO are compared with those in the bulk. The calculated metal dissolution energies indicate that titanium as a dopant may suppress TM dissolution on the surface at elevated temperatures by improving the structural stability and increasing the dissolution energies of nickel and manganese ions. These theoretical findings are validated by experimental results, which show that TM dissolution in LNMO can be effectively reduced by titanium surface doping, leading to enhanced electrochemical performance. These findings provide insights for mitigating TM dissolution in spinel cathode materials.

Figure 6.6.1a shows the atomic model of bulk LNMO from first-principles calculations. To investigate the thermodynamic phase stability of LNMO, we calculated the enthalpy of formation of $\text{Li}_{1-x}\text{Ni}_{0.5}\text{Mn}_{1.5}\text{O}_4$ with respect to the inverse lithium content x as presented in Figure 6.6.1b. All the enthalpy values are positive during Li^+ extraction, indicating that there is no intermediate ground state, and that LNMO undergoes a two-phase reaction between $\text{Li}_{1.0}\text{Ni}_{0.5}\text{Mn}_{1.5}\text{O}_4$ and $\text{Li}_{0.0}\text{Ni}_{0.5}\text{Mn}_{1.5}\text{O}_4$ during the cycles at low temperature limit. Despite the thermodynamic two-phase reaction, the formation of metastable intermediate phases would be possible during charge-discharge processes. Thus, we carefully investigated the intermediate atomic models with various lithium concentrations based on the enthalpy of formation.

The electronic structure of bulk LNMO was also investigated in the fully lithiated ($x=0$) and fully delithiated ($x=1$) states. From a comparison of the partial (projected) density of states (PDOS) of the Ni d-orbital, Mn d-orbital, and O p-orbital of bulk LNMO (Figure 6.6.1c), Ni and Mn oxidation states are identified as 2^+ and 4^+ , respectively, based on the effects of crystal field stabilization[11, 21] and d-electronic donor,[38, 60] as shown in the red solid lines. As expected, the changes in Mn d- and O p-orbitals are negligible during Li^+ extraction, indicating that Mn and O ions do not participate in the

electrochemical reactions. Only the Ni ions are involved in the electrochemical reactions as redox centers in the bulk, by the double redox reaction from Ni^{2+} to Ni^{4+} during delithiation.[69] In addition, the PDOSs of the intermediate phases also describe the double redox reaction of Ni^{2+} to Ni^{4+} without significant changes of Mn and O ions during the redox reaction.

Meanwhile, it is essential to examine the corresponding electrochemical reactions at the surface of LNMO, because this is where TM dissolution is initiated and propagated into the bulk material. For this purpose, both (111) and (400) surface models of LNMO are established using the Gibbs dividing surface[37] with vacuum regions of 20 Å between the top and bottom parts of periodic slabs. The (111) and (400) surfaces not only are the major peaks of the XRD pattern of LNMO, but also have an important role in the electrochemical performances of the spinel compounds.[70] Thus, it is important to understand TM dissolution behaviors of the (111) and (400) surfaces of LNMO. The atomic model of the (111) surface slab consists of 156 atoms with a thickness of 11.8311 Å, and that of the (400) surface slab consists of 82 atoms with a thickness of 10.5720 Å, as shown in Figure 6.6.2a and 6.6.2d, respectively. To assess the validity of these surface models, we investigate the electronic structures of the TMs in the middle (semi-bulk region) of each model. PDOSs for the Ni and Mn d- orbitals in semi-bulk (Figure 6.6.2b and 6.6.2e) show electronic structures similar to those in bulk LNMO (Figure 6.6.1), confirming the validity of the surface models. In contrast, PDOSs for the Ni and Mn d-orbitals on the surface display oxidized Ni ions and slightly changed Mn^{4+} , respectively (Figure 6.6.2c and 6.6.2f), indicating the electrochemical changes at the surface.

The effects of surface doping on the TM dissolution of LNMO are investigated with both (111) and (400) surface models (Figure 6.6.3a and 6.6.3b, respectively), by replacing a Mn atom with a dopant atom so that the Ni ions remain the redox center in the LNMO structure. To examine the

qualitative evaluations of surface-doping elements, we modeled the doped surface models by replacing one Mn atom on the (111) and (400) surfaces of LNMO with dopants. A successful dopant needs to satisfy two criteria of (i) being in the same chemical state (4^+) as the Mn ion to maintain the redox state of Ni ions, and (ii) having strong binding with O ions to enhance the structural stability of the LNMO surface. Four potential dopants, namely Si, Ti, V, and Zr are considered, and Figure 6.6.3c shows the calculated dissolution energies for Ni and Mn ions at the (111) and (400) surfaces with and without doping. The dissolution energy E_{dis} was calculated as follows:

$$E_{dis} = E_V - E_s + \mu_M \quad (6.6.1)$$

where E_V is the total energy of the surface model with a metal vacancy, E_s is the total energy of the pristine surface model, and μ_M is the chemical potential of the metal element. In this study, μ_M is determined by M^{2+} state in MO compounds, because the HF generation from the electrolyte oxidation causes the dissolution of metals in the form of M^{2+} , [38, 41, 65, 66] which can be defined as follows:

$$\mu_M = E_{MO} - \mu_O \quad (6.6.2)$$

where E_{MO} is the total energy of the MO compound and μ_O is the chemical potential of oxygen estimated by O_2 gas. The dissolution energy indicates the thermodynamic stability of the dissolutions in the form of M^{2+} . That is to say, in the assumption that the dissolution is directly related to the formation energy of metal vacancy in the surface structures, we can predict potential candidates for surface doping on the surfaces of LNMO to mitigate undesirable TM dissolutions owing to the electrolyte oxidation and HF generation. From these data, Ti produces the highest dissolution energies for Mn and Ni in almost all the cases indicating that Ti would make the dissolution of TMs at the surfaces thermodynamically unstable. Therefore, *ab initio* analysis predicts that Ti is the most promising dopant for improving the

surface stability of LNMO.

To clarify the specific role of Ti at the surface of LNMO, we further examined the corresponding surface models of Ti-surface-doped LNMO (TSD-LNMO). The role of Ti ions can be more clearly understood from the electronic structure of O ions at the TSD-LNMO surfaces, Figure 6.6.3d and 6.6.3e show that, on both (111) and (400) surfaces of TSD-LNMO, O ions surrounding the Ti ions have a lower average net charge (i.e., with more electrons) compared with other O ions. The more negative charge of the former indicates the formation of a stronger structural frame with the TM ions. In terms of PDOS (Figure 6.6.3f and 6.6.3g), the electronic structures of O p-orbital surrounding Ti (red solid lines) show a more reduced character than those of other O p-orbital (green dashed lines), at both (111) and (400) surfaces of TSD-LNMO.

To investigate whether surface Ti doping actually mitigates TM dissolution according to the prediction, LNMO and TSD-LNMO nanoparticles were synthesized by a sol-gel reaction. Figure 6.6.4a shows the powder XRD patterns of the two synthesized nanoparticles. All the patterns are matched to a cubic spinel structure (JCPDS 80-2162). There is no evidence of impurity or secondary phase in the patterns of LNMO and TSD-LNMO, indicating that Ti is doped into the surface lattice structure of LNMO. Rietveld refinement results indicate that LNMO and TSD-LNMO have almost identical lattice parameters and similar crystallite sizes estimated by the Scherrer equation (44.2131 nm for LNMO and 42.4235 nm for TSD-LNMO). The successful doping is further confirmed by ion-sliced high-resolution transmission electron microscopy (HRTEM) images combined with energy dispersive X-ray spectroscopy (EDS) mapping results (Figure 6.6.4b, 6.6.4c, 6.6.4d, and 6.6.4e). As shown in Figure 6.6.4e, unlike Ni, Mn, and O, most of the Ti atoms are mapped near the surface, indicating the doped Ti is concentrated in the surface region. The EDS line profile data for TSD-LNMO

also demonstrates the surface doping of Ti. The concentration of Ti from the EDS results based on HRTEM (Figure 6.6.4) for TSD-LNMO was measured to be 0.63 wt%, which was comparable value with the inductively coupled plasma mass spectrometry (ICP-MS) analysis (≈ 0.63 wt%).

As mentioned earlier, the dissolution energies of Mn and Ni are increased by Ti surface doping, which means TSD-LNMO is likely to have improved surface structural stability. In this context, experimental X-ray photoelectron spectroscopy (XPS) spectra of Ti 2p show the stable Ti^{4+} state (Figure 6.6.5a), which is in good agreement with the calculated PDOS shape of Ti^{4+} in Ti d-orbitals at both (111) and (400) surfaces (Figure 6.6.5b). In addition, because of the small amount of Ti surface doping (≈ 1 wt%), a slight shift (≈ 0.16 eV) of the O 1s peak of TSD-LNMO towards higher binding energy (left) is evident in Figure 6.6.5c. These results indicate that Ti could reinforce the surface structure, so that the TM dissolution could be suppressed by supplemental TM–O bonding and higher TM dissolution energies.

To quantify the suppression of TM dissolution by Ti doping, we measured the amount of dissolved Mn and Ni in the cell electrolyte with respect to storage times at 25 °C (room temperature). As expected, the dissolved TM concentrations decreased after the surface doping with Ti, as shown in Figure 6.6.6. Importantly, the suppression of TM dissolution became more evident as the storage time lengthened.

Figure 6.6.7a and 6.6.7c show the cyclic performances of LNMO and TSD-LNMO cathodes at 25 and 40 °C, at the current density of 1 C (148 mA g^{-1}) for 200 cycles. Figure 6.6.7b and 6.6.7d represent the corresponding initial galvanostatic charge–discharge profiles. The cyclic performances of LNMO and TSD-LNMO are hardly different at room temperature, but TSD-LNMO shows enhanced cyclic performance at 40 °C. The effect of surface doping was more evident at high temperature (40 °C) because the electrolyte decompositions could be accelerated by the increased hydrolysis of LiPF_6 and

HF generation at elevated temperatures. In other words, Ti surface doping improves the cyclic performance by suppressing TM dissolution at the surface under severe working conditions. Therefore, Ti surface doping does suppress the TM dissolution in LNMO during cycling, in agreement with the first-principles predictions.

In conclusion, we investigated the dissolution mechanism of TM in the $\text{LiNi}_{0.5}\text{Mn}_{1.5}\text{O}_4$ (LNMO) structure, based on first-principles surface calculations. The calculation results suggest that Ti doping on the surface of LNMO could suppress undesirable TM dissolution, and that TM dissolution is directly related to the electronic structures of Ni and Mn ions at the surface. The structural stability of LNMO surfaces can be effectively improved by Ti surface doping, because the doped Ti ions maintain their strongly oxidized character, allowing the surrounding O ions to retain more electrons. Therefore, the surface ionic bonding of TM–O is reinforced, and the TM dissolution energies are increased. These theoretical findings are validated experimentally. TSD-LNMO shows reduced TM dissolution, leading to much improved specific capacity and cyclic performance especially at elevated temperatures. This study reveals a new approach to improve LNMO cathode performance by the surface doping, which could be applied to other electrode materials. Meanwhile, the combined framework of first-principles predictions and experiments for surface doping could be generalized to the design of other electrode materials.

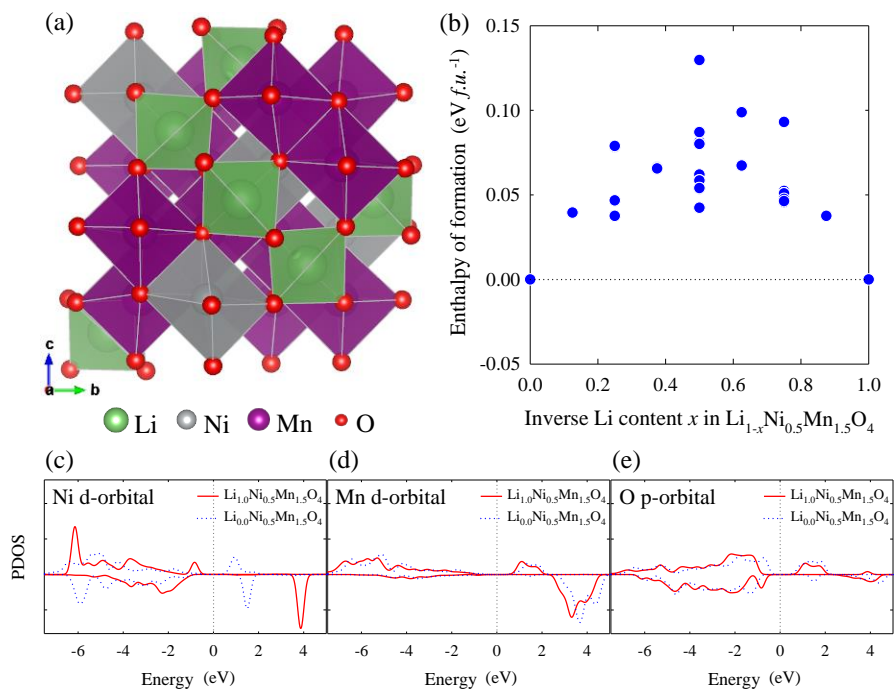


Figure 6.6.1 (a) Atomic model of $\text{LiNi}_{0.5}\text{Mn}_{1.5}\text{O}_4$. (b) Enthalpy of formation with respect to the inverse Li content x . Partial (projected) density of states of (c) Ni d-orbital and (d) Mn d-orbital, and (e) O p-orbital, in $\text{Li}_{1.0}\text{Ni}_{0.5}\text{Mn}_{1.5}\text{O}_4$ (red solid line) and $\text{Li}_{0.0}\text{Ni}_{0.5}\text{Mn}_{1.5}\text{O}_4$ (blue dotted line).

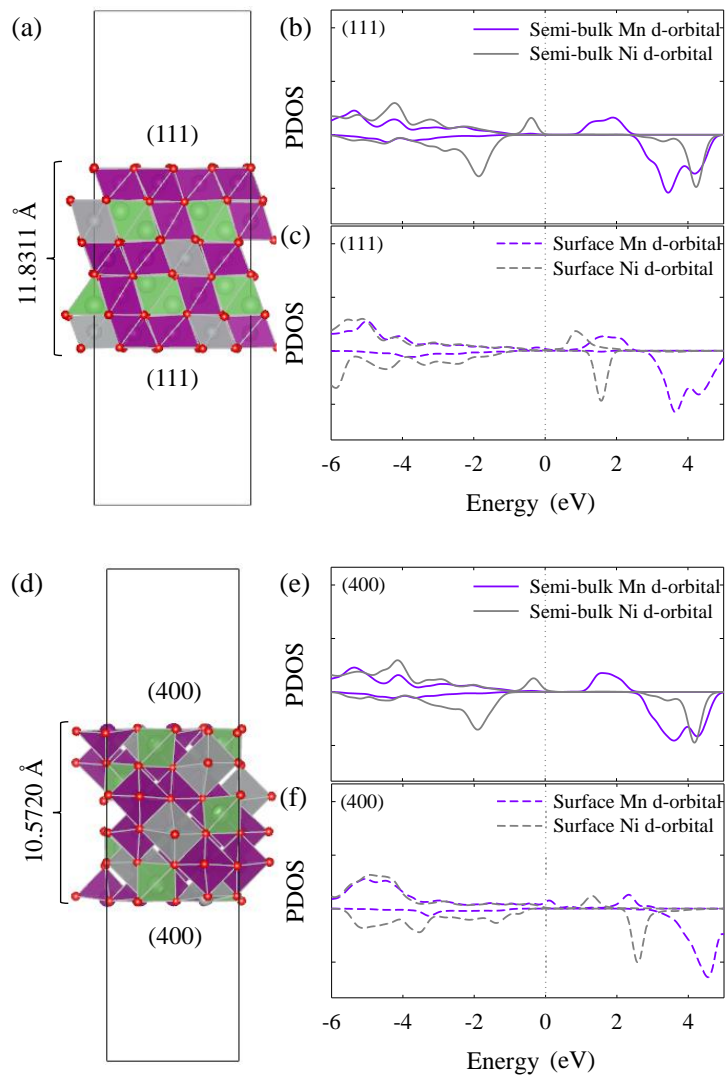


Figure 6.6.2 Atomic models of (a) the (111) surface, and the corresponding PDOS of the Ni (gray lines) and Mn (purple lines) d-orbitals at (b) semi-bulk and (c) surface regions. Atomic models of (d) the (400) surface, and the corresponding PDOS of the Ni (gray lines) and Mn (purple lines) d-orbitals at (e) semi-bulk and (f) surface regions.

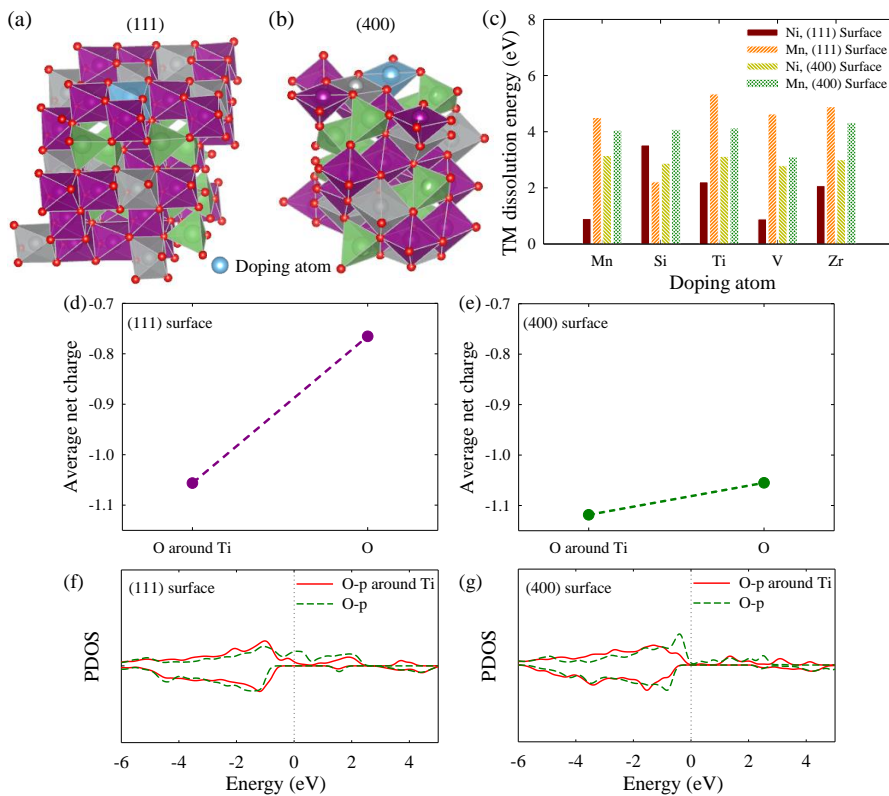


Figure 6.6.3 Surface doping models with one doping atom on the (a) (111) and (b) (400) surfaces in LNMO. (c) Calculated dissolution energies of Ni and Mn ions at (111) and (400) surfaces. Average net charge of O ions around and away from the Ti ions on the (d) (111) and (e) (400) surfaces of TSD-LNMO. PDOS of O p-orbitals of O ions around Ti (red solid line) and other O ions (green dashed line) on (f) (111) and (g) (400) surfaces of TSD-LNMO. The Fermi level is 0 eV (gray dotted line).

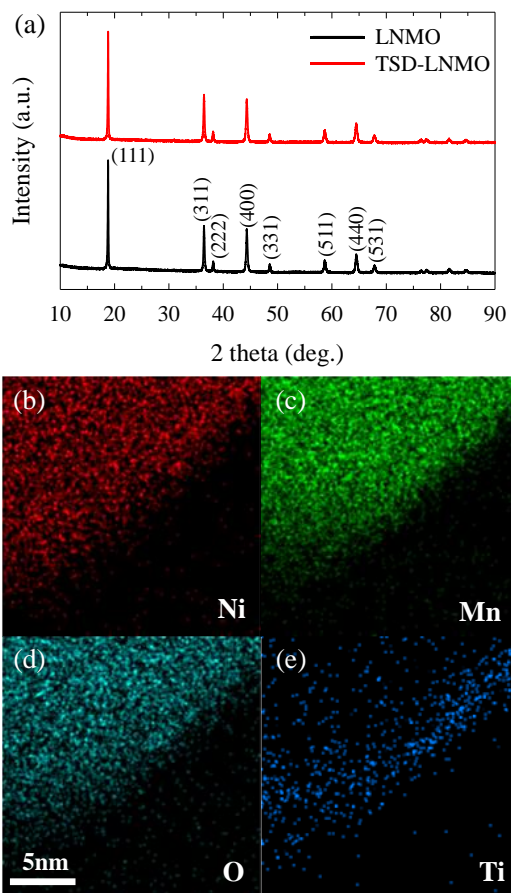


Figure 6.6.4 (a) X-ray diffraction patterns of pristine LNMO (black), TSD-LNMO (red). EDS mapping data of ion-sliced HRTEM for (b) Ni, (c) Mn, (d) O, and (e) Ti in TSD-LNMO.

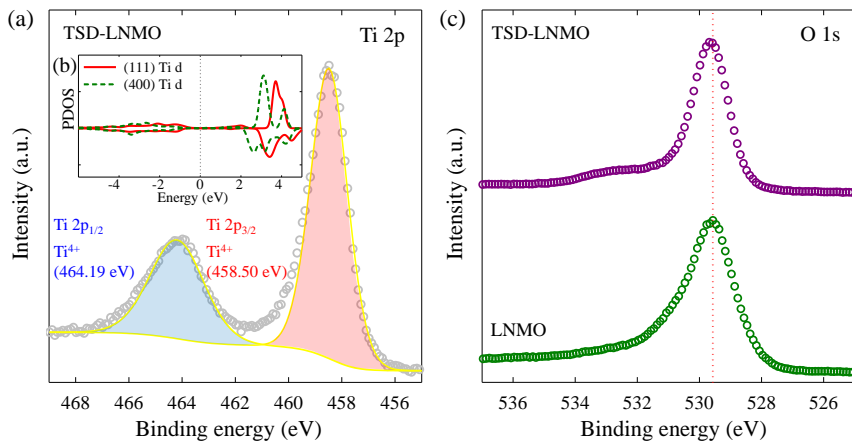


Figure 6.6.5 (a) X-ray photoelectron spectroscopy (XPS) spectra of Ti 2p of TSD-LNMO. Inset: (b) calculated PDOS of Ti d-orbital on the (111) and (400) surfaces (red solid and green dashed lines, respectively). The Fermi level is 0 eV (gray dotted line). (c) The O 1s peak for TSD-LNMO (purple open circles) and LNMO (green open circles).

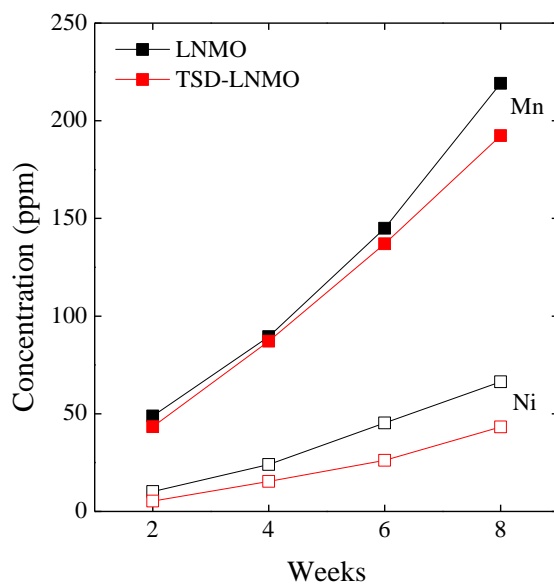


Figure 6.6.6 Concentrations of Ni (open squares) and Mn (filled squares) in the electrolyte with respect to the storage time (week) for LNMO (black) and TSD-LNMO (red).

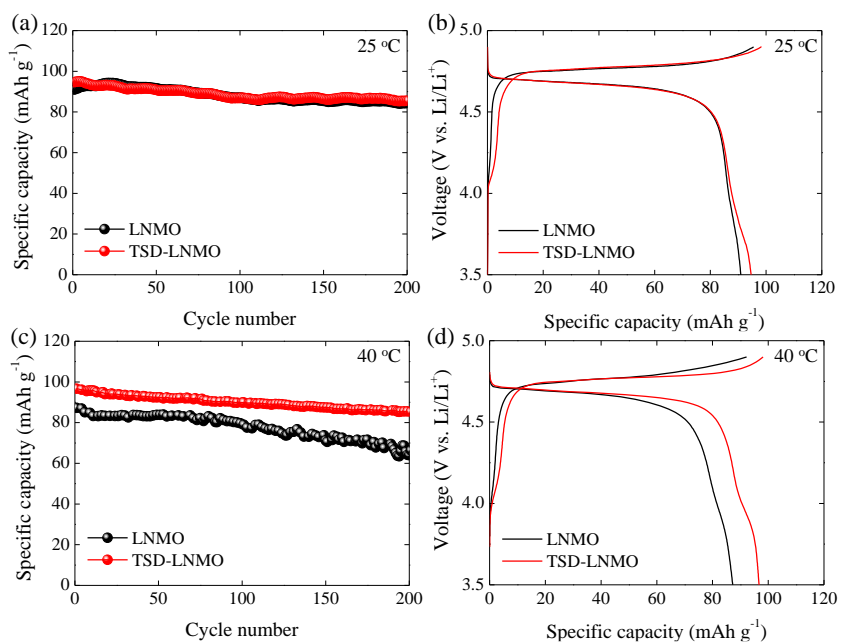


Figure 6.6.7 (a) Discharge cyclic performance and (b) initial charge-discharge profiles at 25 °C, of LNMO (black), and TSD-LNMO (red) at 1C. (c) Discharge cyclic performance and (d) initial charge-discharge profiles at 40 °C.

6.7 Elastic Softness and Power Characteristics in Spinel $\text{LiNi}_{0.5}\text{Mn}_{1.5}\text{O}_4$ [25]

The power characteristics of lithium-ion batteries (LIBs) are crucial for the advent of commercialized, high-power applications, such as electric vehicles. Through both first-principles multiscale simulations and experiments, here, we present fundamental understandings on the power characteristics of the high-voltage spinel cathode correlated with its elastic softness and phase transformation in nanodomains for high-power LIBs. Atomic models of $\text{LiNi}_{0.5}\text{Mn}_{1.5}\text{O}_4$ and $\text{LiNi}_{0.5}\text{Mn}_{1.5-x}\text{Ti}_x\text{O}_4$ are developed for multiscale phase modeling based on structural information for the as-prepared nanopowders. First-principles calculations suggest that the thermodynamic phase stability of $\text{LiNi}_{0.5}\text{Mn}_{1.5}\text{O}_4$ can be effectively enhanced by the incorporation of Ti into the structure without any change to the redox mechanism. Ti incorporation provides a faster ionic mobility of $\text{LiNi}_{0.5}\text{Mn}_{1.5}\text{O}_4$ because of the improved phase stability and slightly expanded structure. Based on the multiscale phase transformation kinetics, $\text{LiNi}_{0.5}\text{Mn}_{1.5-x}\text{Ti}_x\text{O}_4$ exhibits an enhanced elastic softness and slower phase separation than $\text{LiNi}_{0.5}\text{Mn}_{1.5}\text{O}_4$ in the nanodomain during Li^+ insertion and extraction. Such characteristics are mainly responsible for the improved electrochemical performance at higher current rates, as confirmed by electrochemical experiments. This fundamental understanding of the power characteristics with respect to the correlations with elastic softness and phase transformation will provide a guideline to develop and design advanced materials for high-power LIBs.

Figure 6.7.1 shows powder X-ray diffraction (XRD) patterns for the as-synthesized LNMO and LNMTO with Rietveld refinement profiles. All the diffractions can be indexed to a cubic spinel structure (JCPDS 80-2162). The a lattice parameter slightly increased with respect to the amount of Ti doping because of the larger ionic radius of Ti^{4+} (0.61 Å) than that of Mn^{4+} (0.54 Å).[71] Corresponding atomic models of LNMO (Figure 6.7.1a) and LNMTO (Figure 6.7.1b) were carefully developed for the DFT calculations based on

the structural information obtained from the Rietveld refinement. In the given spinel structures, Li (green atoms) occupied the tetrahedral sites surrounded by O (red atoms); and Mn (purple atoms), Ni (gray atoms), and Ti (blue atoms) occupied the octahedral sites.

The morphologies of the as-prepared LNMO and LNMTO nanoparticles were characterized using FESEM. Both materials have a uniform morphology with an average particle size of ~100 nm. The HRTEM with EDS mapping results indicate that Ti is uniformly distributed in the LNMTO structure. According to STEM images and line profiles for LNMO (Figure 6.7.1c) and LNMTO (Figure 6.7.1d), LNMTO has a slightly larger *d*-spacing (0.5094 nm) than LNMO (0.5041 nm), which is consistent with the calculated *a* lattice parameters of the fully relaxed LNMO and LNMTO structures

Figure 6.7.2 shows the chemical states of each element in LNMO (black circles) and LNMTO (red triangles) measured by XPS after Ar ion sputtering for 300 s. The XPS spectra carefully fitted with the C 1s spectra at 284.6 eV. We found that LNMO and LNMTO represent almost identical chemical states of Mn 2p and Ni 2p, indicating that the chemical states of Mn and Ni ions are similar in both LNMO and LNMTO structures. The results are in good agreement with the electronic structures of Mn and Ni d-orbitals for LNMO and LNMTO. The Ti2p spectra in Figure 6.7.2a shows almost perfect Ti⁴⁺ in LNMTO, which agrees with the description of Ti⁴⁺ (absence of electrons in the valence band) in the PDOS of Ti d-orbital. Interestingly, the O1s spectra of LNMTO was shifted to the direction of strong binding energy compared with LNMO (Figure 6.7.2b), which suggests that O ions in LNMTO are likely to have higher binding energy than those of LNMO. Therefore, the strong Ti-O bonds (662 kJ mol⁻¹)[25] and larger Ti⁴⁺ ion size are attributed to the slightly expanded structure of LNMTO with stronger binding energy than LNMO, which allows an affirmative role to the

performance of LNMTO.

The Li⁺ diffusion kinetics was investigated experimentally and theoretically to elucidate the effect of Ti incorporation on the ionic mobility in the structure. Figure 6.7.2c shows the Li⁺ diffusion coefficients for LNMO and LNMTO measured using the GITT. Both materials present the two minima related to the Ni²⁺/Ni⁴⁺ redox during discharge. The chemical diffusion coefficient can be calculated according to the following equation:

$$D_{Li} = \frac{4}{\pi\tau} \left(\frac{m_B V_M}{M_B A} \right)^2 \left(\frac{\Delta E_S}{\Delta E_\tau} \right)^2 \quad (6.7.1)$$

where τ is the constant current flux time, m_B is the active mass of the electrode, V_M is the molar volume of the electrode, M_B is the molecular weight of the electrode, A is the surface area of the electrode (3.874 m² g⁻¹ for LNMO and 3.399 m² g⁻¹ for LNMTO determined from the BET surface area), ΔE_S is the total change in the cell voltage during a single step, and ΔE_τ is the change in the steady-state voltage during a single step. The calculated D_{Li} values for LNMTO are in the range of 2.04×10^{-9} – 9.74×10^{-8} cm s⁻¹, i.e., slightly higher than those for LNMO. At the same time, we calculated migration barriers, ΔE , of Li⁺ in both LNMO (black circles) and LNMTO (red triangles) structures with 0.875 mol of Li because the diffusion coefficient is proportional to $e^{-\Delta E/k_B T}$ (k_B is the Boltzmann constant and T is the absolute temperature) based on the Arrhenius expression. The LNMTO exhibits a lower migration barrier (0.26 eV) than that of LNMO (0.39 eV), as shown in Figure 6.7.2d. As a result, the diffusion coefficient is estimated to be $\propto 2.8 \times 10^{-7}$ for LNMO and $\propto 4.3 \times 10^{-5}$ for LNMTO. Note that the diffusion coefficient of LNMTO is theoretically $\sim 1.5 \times 10^2$ time higher than that of LNMO, which is mainly attributed to the slightly expanded structure of LNMTO, as previously discussed.

Additionally, the phase transformation behaviors of LNMO and

LNMTMO were investigated by multiscale approaches from atomic-scale to meso-scale analyses. The first-principles mixing enthalpy at the ground state (0 K), homogeneous bulk free energy (f_h), and open-circuit voltage (OCV) were calculated at a finite temperature (300 K). The mesoscale phase separation behaviors of both structures were simulated based on this multiscale calculation.[1, 13, 15-17, 26, 48] Figure 6.7.3 show the first-principles mixing enthalpy per *f.u.* of L_{1-y} NMO and L_{1-y} NMTO, respectively, for all possible configurations with respect to the inverse Li content, y . The mixing enthalpy for LNMO (black circles, Figure 6.7.3a),[24] was greater than that for LNMTMO (red triangles, Figure 6.7.3b). This finding can be reasonably explained by the improved thermodynamic stability of LNMTMO induced by the incorporation of Ti into the structure. More importantly, the lower mixing enthalpy of LNMTMO induces a lower homogeneous bulk free energy, f_h (~0.032 eV), than that of LNMO (~0.046 eV). As y increases, f_h gradually increases because of the generation of strain energy from the contraction of the atomic structure. In this context, LNMTMO is thermodynamically more stable than LNMO during the phase transformation and structural contractions because of the lower strain energy and reduced phase barrier. In addition, f_h provide the free energy with a phase barrier (or free energy barrier) between the fully-lithiated and fully-delithiated state; that is, the LNMO phase separation is likely faster than LNMTMO because of its sharper slope from the higher phase barrier, which will be discussed later in more detail.

Considering the effect of the finite temperature at 300 K, the calculated OCV of LNMO and LNMTMO are compared in Figure 6.7.3d. The lower mixing enthalpy and the free energy of LNMTMO enhance its thermodynamic phase stability, leading to a reduction of the overpotential during Li^+ insertion and extraction, as confirmed by the GITT profiles in the inset. Furthermore, one-phase reactions (shaded area) occur at both sides of the two-phase

reaction (non-shaded area) because of the miscibility gap from the configuration entropy at 300 K. It reveals that the miscibility gap of LNMTO (red shaded area) is slightly wider than that of LNMO (black shaded area) because of the lower phase barrier of LNMTO. More importantly, the miscibility gap of the delithiated state is wider than that of lithiated state, which induced by the strain energy from the tension and compression during Li^+ extraction. On the other hand, LNMO (black line) shows the step of OCV plateau due to the disordered character of the as-synthesized powder.[72] In contrast, LNMTO (red line) represents smooth electrochemical reactions during Li^+ extraction as shown in GITT profile. This is due to the improved thermodynamic phase stability of LNMTO induced by the lower strain energy and decreased phase barrier that would guarantee improved power characteristics at high operating voltages, allowing for a smooth and stable Li^+ insertion and extraction during the phase transformation (between Li-rich and Li-poor phases) and structural contractions.

For the in-depth investigations on the stress and strain generations and distributions in both the LNMO and LNMTO structures, the variation of the volumetric strain, $\varepsilon_V (\Delta V/V_0)$, with respect to y and the increasing value of the normalized DFT energy ($E-E_0$) *vs.* volume ratio (V/V_0) are represented in Figure 6.7.4, respectively. The bulk moduli of LNMO ($B_{\text{LNMO}} = 181.81$ GPa) and LNMTO ($B_{\text{LNMTO}} = 135.45$ GPa) were evaluated by the Birch-Murnaghan equation of state (EOS).[73, 74]

As shown in Figure 6.7.4a, the volumetric strain of LNMO and LNMTO gradually decreased, and the absolute volumetric strain of LNMTO was slightly larger than that of LNMO (Figure 6.7.4b). LNMTO is elastically softer and generates less stress because its bulk modulus is much smaller than that of LNMO. As a result, the distribution of elastic stress ($\sigma_1 + \sigma_2$) of LNMO (Figure 6.7.4c) is more severe than that of LNMTO (Figure 6.7.4d) at

all values of dimensionless time, \hat{t} . Due to the lower bulk modulus of LNMTO, the stress generations of LNMTO can be effectively mitigated during the phase transformations from solid solution of $y = 0.5$, and the maximum elastic stress of LNMTO ($\sim \pm 0.6$ GPa) is lower than that of LNMO ($\sim \pm 1.2$ GPa). Therefore, the stress generation in LNMTO during Li^+ insertion can be alleviated by the enhanced elastic softness arising from Ti incorporation. This would improve the power characteristics because the smooth Li^+ insertion and extraction reduces the elastic energy dissipation.

Furthermore, the lower phase barrier of LNMTO offers a slower phase separation of $\text{L}_{1-y}\text{NMTO}$ than that of L_{1-y}NMO at $y = 0.5$, which was observed using a meso-scale phase field model in the nanodomains (Figure 6.7.5). In contrast, Figure 6.7.5a describes the faster phase separation of LNMO than that of LNMTO (Figure 6.7.5b) because of the higher phase barrier of LNMO. The shape of the phase distribution for LNMTO at $\hat{t} = 0.5$ is mainly homogeneous at approximately $y = 0.5$, but the phase of LNMO at the same dimensionless time starts to separate to L_1NMO and L_0NMO , and the phase separation has progressed at $\hat{t} = 0.75$. This is mainly because of the different phase barriers of LNMO and LNMTO, which affects the electrochemical rate capability. The intercalating Li ions of LNMO are likely to be hindered by carrying Li ions from the strong phase separation of LNMO during the electrochemical reaction, so the electrochemical reactions at higher rates could be impeded. In contrast, the intercalating Li ions of LNMTO are less interrupted by carrying Li ions from the phase separation because of the lower phase barrier required to separate the phases in LNMTO; thus, the rate capability of LNMTO could be improved over that of LNMO.

For experimental validation, we have compared the rate capabilities of LNMO and LNMTO at various current densities of 240, 400, 600, 800, 1000 mA g^{-1} in a voltage range of 3.5 to 5.0 V vs. Li/Li^+ . As shown in Figure 6.7.5c,

both LNMO and LNMTO showed similar discharge capacities at low current densities (below 400 mA g⁻¹). In contrast, LNMTO exhibited much higher discharge capacities than LNMO at higher current densities of 600, 800, and 1000 mA g⁻¹. The corresponding galvanostatic charge-discharge profiles of LNMO (black lines) and LNMTO (red lines) at the high current densities of 800 and 1000 mA g⁻¹ are presented in Figure 6.7.5d. From this comparison, LNMTO showed a higher specific capacity and reaction voltage than LNMO, which is consistent with our theoretical predictions. Consequently, the rate capability of the LNMO cathode is related to the strength of the phase separation and the elastic softness of the host structures during the cycles, which are essential for determining the power characteristics of spinel LNMO. Thus, it is necessary to reduce the stress generations and alleviate the phase separations to improve the power characteristics.

In summary, the power characteristics of the high-voltage spinel oxides (LNMO and LNMTO) correlated with the elastic softness, and the phase transformations have been fundamentally investigated based on theoretical predictions and experimental observations. Ti incorporation provides LNMTO with an improved thermodynamic stability compared to LNMO without any change of the electrochemical redox mechanism. The theoretical investigations clearly determined the important role of Ti in the given structure. A slight expansion of the LNMTO structure directly affects the Li⁺ diffusion kinetics by lowering the migration barriers of Li⁺ in the structure, which was confirmed by GITT measurements. We found that LNMTO became elastically softer because of the Ti incorporation by comparing the volumetric strain and bulk moduli of LNMO and LNMTO. As a result, the stress generation of LNMTO can be alleviated in the nanodomain during Li⁺ insertion and extraction. Thus, the phase separation in LNMTO is slower in the mesoscale phase field model simulations, leading to improved electrochemical reactions at high rates, as further confirmed by the rate

capability measurements. We believe that a fundamental understanding of the power characteristics, including the elastic stiffness and the phase transformation behaviors, will provide a clue to develop and improve high-power applications, such as EVs.

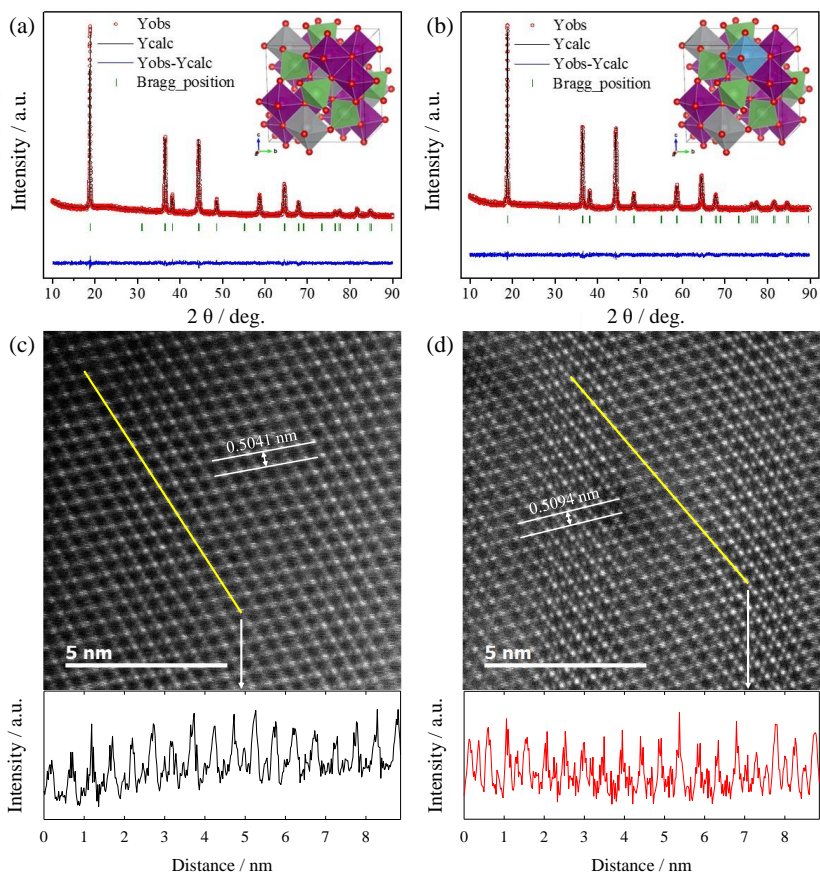


Figure 6.7.1 (a, b) Rietveld refinement of the XRD patterns of as-synthesized (a) LNMO and (b) LNMTO. The atomic models are described in each inset in the figures: Li is green, Mn is purple, Ni is gray, O is red, and Ti is blue. (c, d) STEM images and the line profiles (lower graphs) with d -spacings along each yellow line for as-prepared (c) LNMO (black solid line) and (d) LNMTO (red solid line).

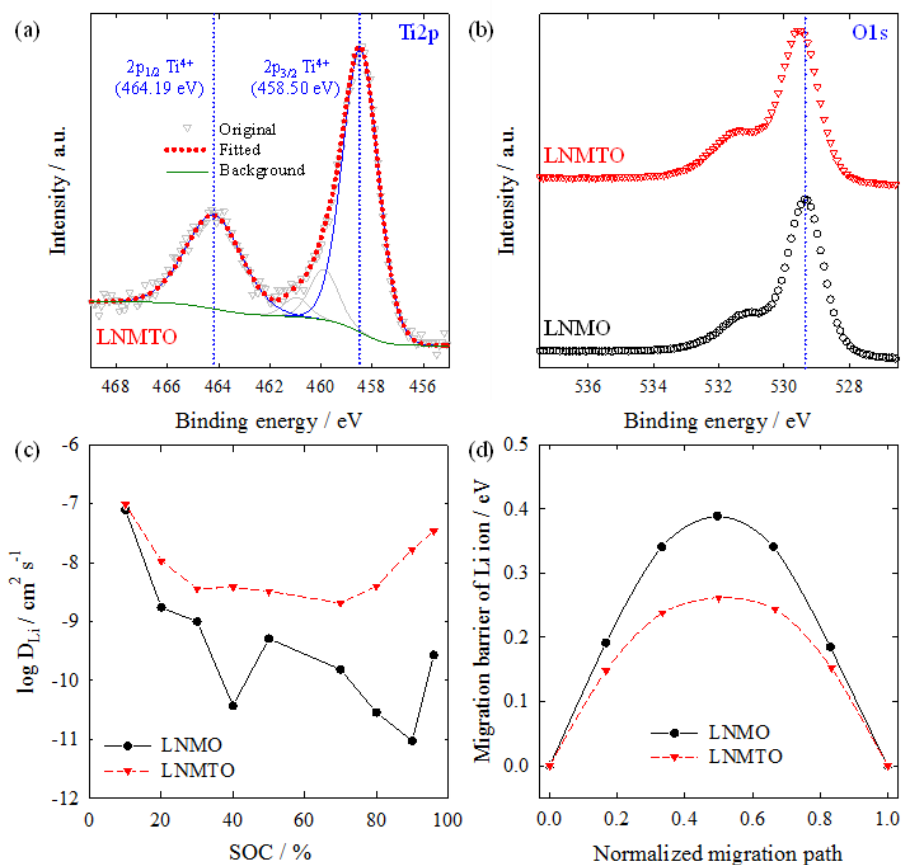


Figure 6.7.2 (a, b) XPS spectra of (a) Ti2p for LNMT0 and (b) O1s for LNMO (black circles) and LNMT0 (red triangles) after Ar ion sputtering for 300 s. (c) Li⁺ diffusion coefficient (D_{Li}) calculated from the GITT curves for LNMO (black circles) and LNMT0 (red triangles) as a function of cell voltage during the discharge processes. (d) Migration barriers of the Li ion in LNMO (black circles) and LNMT0 (red triangles).

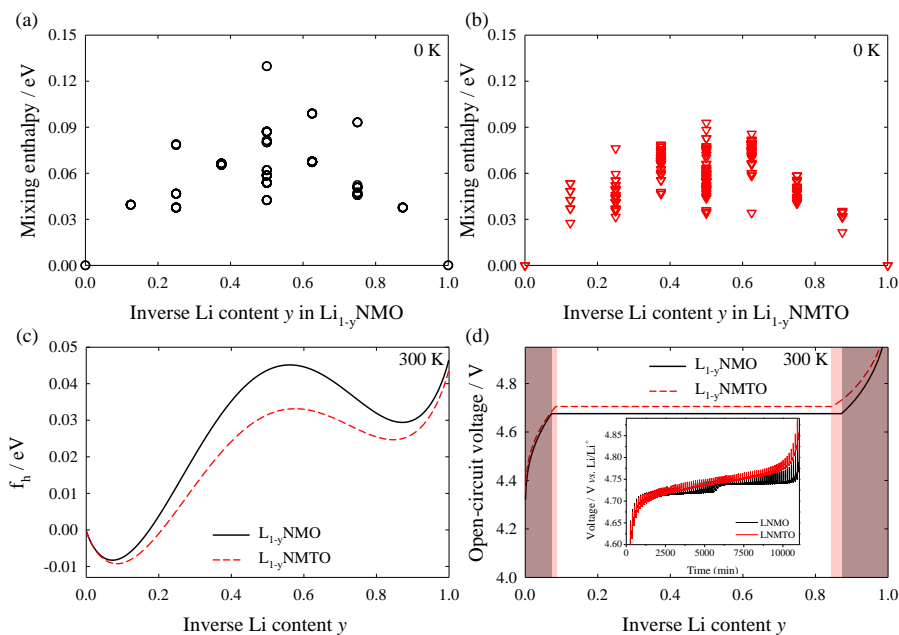


Figure 6.7.3 (a, b) First-principles mixing enthalpy per $f.u.$ at 0 K of (a) $\text{Li}_{1-y}\text{NMO}$ (black circles) and (b) $\text{Li}_{1-y}\text{NMTO}$ (red triangles) as a function of the inverse Li content, y . (c) Homogeneous bulk free energy, f_h , per $f.u.$ and (d) open-circuit voltage at 300 K of $\text{Li}_{1-y}\text{NMO}$ (black solid line) and $\text{Li}_{1-y}\text{NMTO}$ (red dashed line) as a function of the inverse Li content, y , with miscibility gaps of LNMO (black shaded area) and LNMTO (red shaded area), and the GITT curves (inset) of LNMO (black solid line) and LNMTO (red solid line) as a function of time between 3.5 and 4.9 V vs. Li/Li^+ .

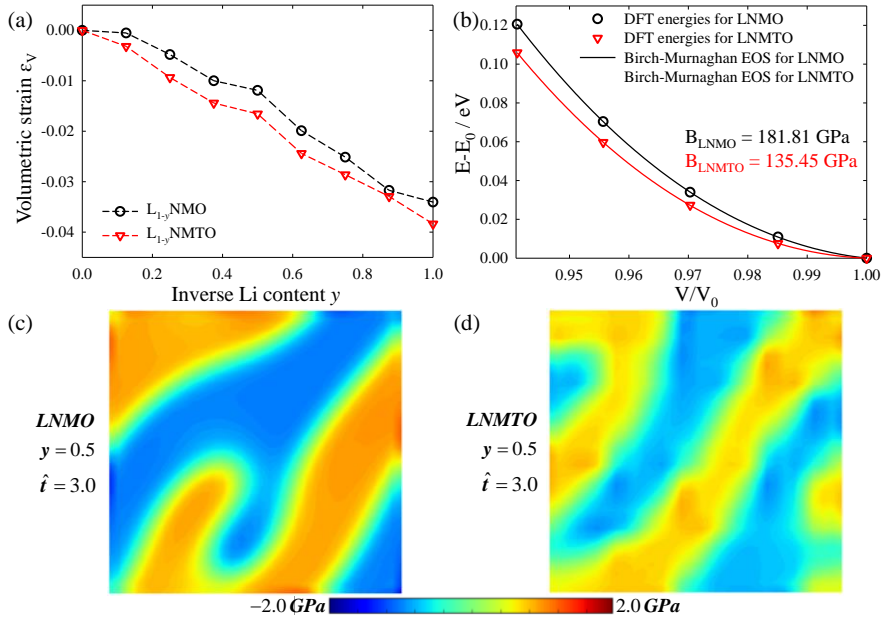


Figure 6.7.4 (a) Volumetric strain, ε_V , of LNMO (black circles and dashed line) and LNMTO (red triangles and dashed line) with respect to the inverse Li content, y . (b) Normalized DFT energy with a fitted line according to the Birch-Murnaghan equation of state (EOS) of LNMO (black circles and solid line) and LNMTO (red triangles and solid line) with respect to the volume ratio (V/V_0). (c, d) Distribution of elastic stress caused by the phase transformation from a solid solution of $y = 0.5$ in LNMO and LNMTO at the dimensionless time, $\hat{t} = 3.0$.

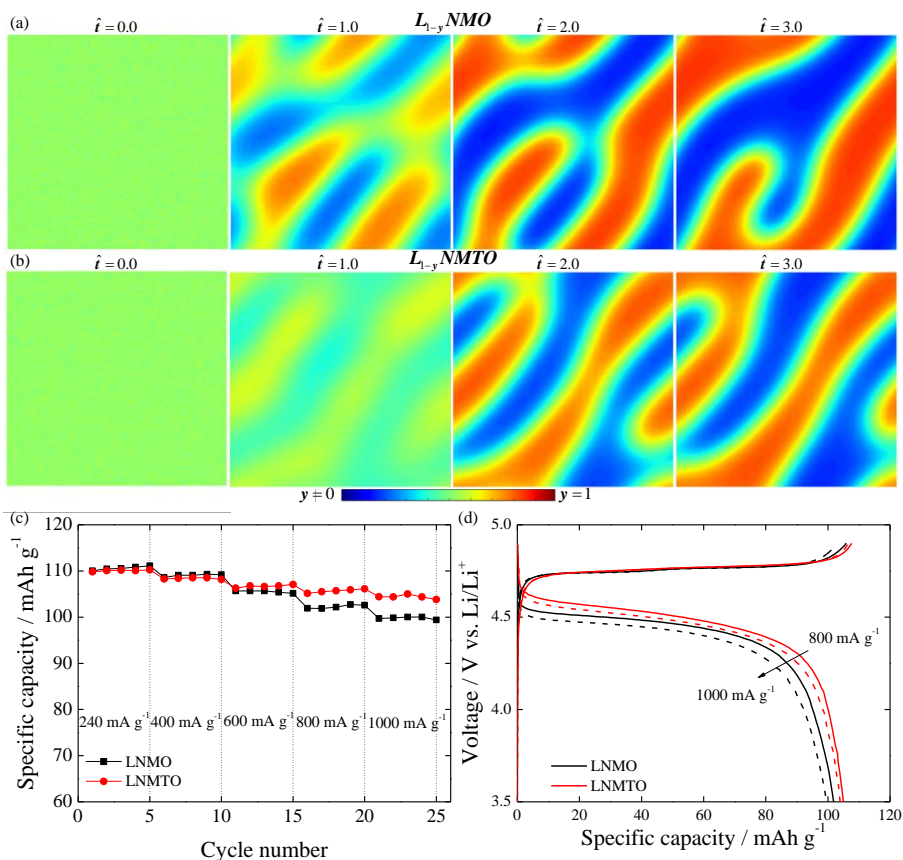


Figure 6.7.5 (a, b) Phase separation kinetics in (a) $L_{1-y}NMO$ and (b) $L_{1-y}NMTO$ from a solid solution of $y = 0.5$ at the dimensionless time, \hat{t} (0.0, 1.0, 2.0, and 3.0). (c) Rate capability at various rates and (d) charge-discharge profiles at specific currents of 800 mA g^{-1} and 1000 mA g^{-1} for LNMO (black circle and lines) and LNMTO (red circle and lines).

6.8 Electrochemistry-coupled Phase Transformation in Li_xFePO_4 [1]

Phase transformations in most electrodes used for electrochemical energy storages follow the conserved dynamics of combined one- and two-phase reactions, which leads to complicated charge-discharge processes with various voltage plateaus; this could affect an electrochemical performance as a generic phenomenon in electrochemical system. In order to fully describe the combined-phase reactions from the atomic scale to the mesoscale, we propose a multiscale-based phase transformation model that also considers electrochemical states and mechanical deformations. This model predicts the miscibility gap, spinodal region, voltage profile, phase transformation, and stress generations of the combined-phase electrodes in the electrochemical reactions. We apply this multiscale model to high-rate cathode material Li_xFePO_4 to fundamentally understand the experimental phase transformation behaviors.[75] This model is applicable to various electrodes for phase behaviors too complex to be detected experimentally due to combined-phase reactions.

Figure 6.8.1a shows the first-principles mixing enthalpy H_{DFT} values of Li_xFePO_4 , which describe the broad two-phase reaction in the range of $0.0 < x < 0.9375$ and the narrow one-phase reaction in the range of $0.9375 < x < 1.0$. In order to estimate enthalpy coefficient ε_i^f , the mixing enthalpies $H_{DFT}^{i,f}$ and H_{CP} were calculated, respectively; the results are shown in Figure 6.8.1b. We note that two different reaction regions exist, and therefore, $\varepsilon_{0,0}^{0,9375}$ is 2.0968 eV per *f.u.* for the two-phase reaction and $\varepsilon_{0,9375}^{1,0}$ is 0.0 eV for the one-phase reaction, which has no phase barrier. We obtain the multiscale-based CP free energy f_{CP} at finite temperature. For the case of Li_xFePO_4 , we additionally considered the configurational electronic entropy due to low electron mobility.[8]

Figure 6.8.1c illustrates f_{CP} at 0 K and 300 K. The miscibility gap arises from the configurational entropies at 300 K. Since the narrow one-phase reaction region over $0.9375 < x < 1.0$ is included in the miscibility gap, the miscibility gap of Li_xFePO_4 has an asymmetric value range (0.049–0.901), which correlates well with the experimental values (0.05–0.89).[75, 76] Figure 6.8.1d depicts the chemical potential $-\mu_{CP}/e$, and as mentioned previously, the chemical potential also exhibits an asymmetric shape due to the existence of the one-phase reaction region. More importantly, Figure 6.8.1c and 6.8.1d imply the characteristics of the phase transformation behaviors. While the solid solution reaction occurs in the outer regions of the miscibility gap (0.0–0.049, 0.901–1.0), the stable two-phase reaction occurs in the inner regions of the spinodal points (0.221–0.718). Unstable nucleation can be generated between the miscibility gap and spinodal region (0.049–0.221, 0.718–0.901).

On the basis of these predicted phase behaviors shown in Figure 6.8.1c and 6.8.1d, the calculated equilibrium voltage profile of Li_xFePO_4 is shown in Figure 6.8.1e. The open-circuit voltage (OCV) calculated by DFT at 0 K (blue squares and line) is obtained. The operating voltage based on this multiscale model V_B can be described using the standard potential V^\ominus and overpotential η as $V_B = V^\ominus + \eta - \mu_{CP}/e$. At thermodynamic equilibrium, the overpotential η tends to zero, and the operating voltage V_B is equal to the standard potential V^\ominus determined by the OCV plateau calculated as per DFT ($V_{DFT}^{i.f}$) within the miscibility gap. Therefore, the OCV estimated by this model can be described by the red dashed line in Figure 6.8.1e, which predicts a profile consistent with the experimental values of Yamada et al.[75] with regard to the miscibility gap and shape of the voltage profile. The slight mismatch in the initial charge process ($0.9375 < x < 1.0$) may have arisen

from the surface redox potential and the overpotential as an innate characteristic of battery electrodes.[37]

For understanding the specific phase transformation kinetics of Li_xFePO_4 based on this model described in Figure 6.8.1, phase transformation simulations were carried out using G_{CP} as determined by our multiscale model; these results are shown in Figure 6.8.2. As shown in Figure 6.8.2 for the case of Li_xFePO_4 , unstable nucleation is generated in the regions outward of the spinodal points, and thus, one-phase reactions can mostly occur yielding a small amount of nucleation, as depicted in Figure 6.8.2c and 6.8.2g ($x = 0.19$ and 0.75 , respectively). In contrast, in the inner region lying within the spinodal points, a stable two-phase reaction is generated, and this is why phase separation is observed in Figure 6.8.2d, 6.8.2e, and 6.8.2f ($x = 0.25$, 0.5 , and 0.69 , respectively), where the degrees of phase separation are related to the slope of $-\mu_{CP}/e$. In Figure 6.8.2h at $x = 0.97$, a naturally perfect one-phase reaction such as solid solution occurs without nucleation and phase separation.

In the context of understanding the corresponding stress generations, the elastic stresses σ_a , σ_b , and σ_{ab} at $\hat{t} = 3.0$ are displayed in Figure 6.8.3. Due to the absence of elastic stresses in the one-phase reaction, the strongly phase-separated case ($x = 0.5$) is represented in Figure 6.8.3a, 6.8.3b, and 6.8.3c. The results show that larger elastic stress along the a direction and alleviated elastic stress along the b direction are generated due to the larger inhomogeneity of concentration in the b direction (Figure 6.8.2e), and the shear stress is mostly relaxed.

In the context of understanding the relationships between overpotential η and phase transformation when a current is applied, Figure 6.8.4 shows the variation in η as a function of \hat{t} for a dimensionless total current of $\hat{I} = 5.0$. For two closely lying concentrations of 0.69 and 0.75 , the behaviors of

η are completely different regardless of whether phase transformation occurs. Within the spinodal region ($x = 0.69$), η is around 0.064 V before phase separation ($\hat{t} < \sim 2.3$) (Figure 6.8.4b, 6.8.4c, and 6.8.4d); however, it reduces to zero after phase separation (Figure 6.8.4e). Meanwhile, η does not vary near the outer point of spinodal region ($x = 0.75$) since there is no phase separation (Figure 6.8.4f, 6.8.4g, 6.8.4h, and 6.8.4i).

In summary, in order to analyze complicated phase behaviors from the atomic scale to the mesoscale, we introduced a multiscale-based phase transformation model for combined one- and two-phase reactions in a conserved-dynamics. Further, this model was developed to also account for stress generations in electrochemical non-equilibrium states. This framework was applied to Li_xFePO_4 , and our model predictions were compared with the experimental results. The free energy and chemical potential values of Li_xFePO_4 as obtained by this model revealed the occurrence of CP reactions (0.0–0.9375: two-phase reaction, 0.9375–1.0: one-phase reaction), an asymmetric miscibility gap range (0.049–0.901), and equilibrium voltage profile, which results agree very well with those of experiments.[75, 76] Furthermore, with this model, we performed numerical simulations of the phase transformation, generation of the elastic stresses, and variation in the overpotential η . These resulting phenomena describe distinct phase transformation behaviors that cannot be reproduced by non-multiscale theories and experiments.

On the basis of these findings, the present model could be applied to various electrode systems with CP reactions in the absence of experimental measurements. For phase transformations that cannot easily be detected through experimental observations due to the multiphase behaviors, the CP Cahn–Hilliard free energy functional can be utilized over a wide range of developed simulation methodologies.

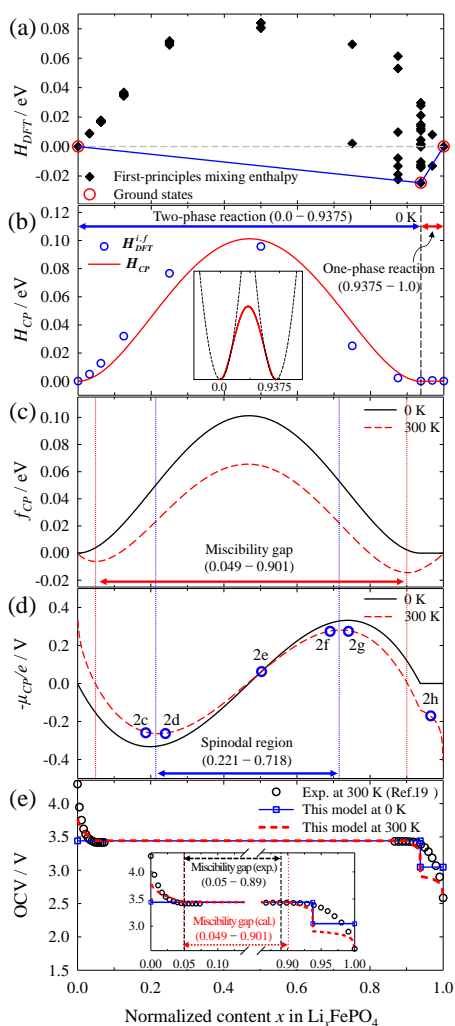


Figure 6.8.1 (a) H_{DFT} (black diamonds) and the ground states (red circles), (b) H_{CP} (red line) with H_{DFT}^{i-f} (blue circles) and scheme of double-well function (inset), (c, d) f_{CP} (c) and $-\mu_{CP}/e$ (d) at 0 K (black solid line) and 300 K (red dashed line), and (e) experimental open circuit voltage (OCV, black circles) reproduced from Yamada et al.[19] and the predicted voltages of this model at 0 K (blue squares and line) and 300 K (red dashed line) as function of Li content x in Li_xFePO_4 .

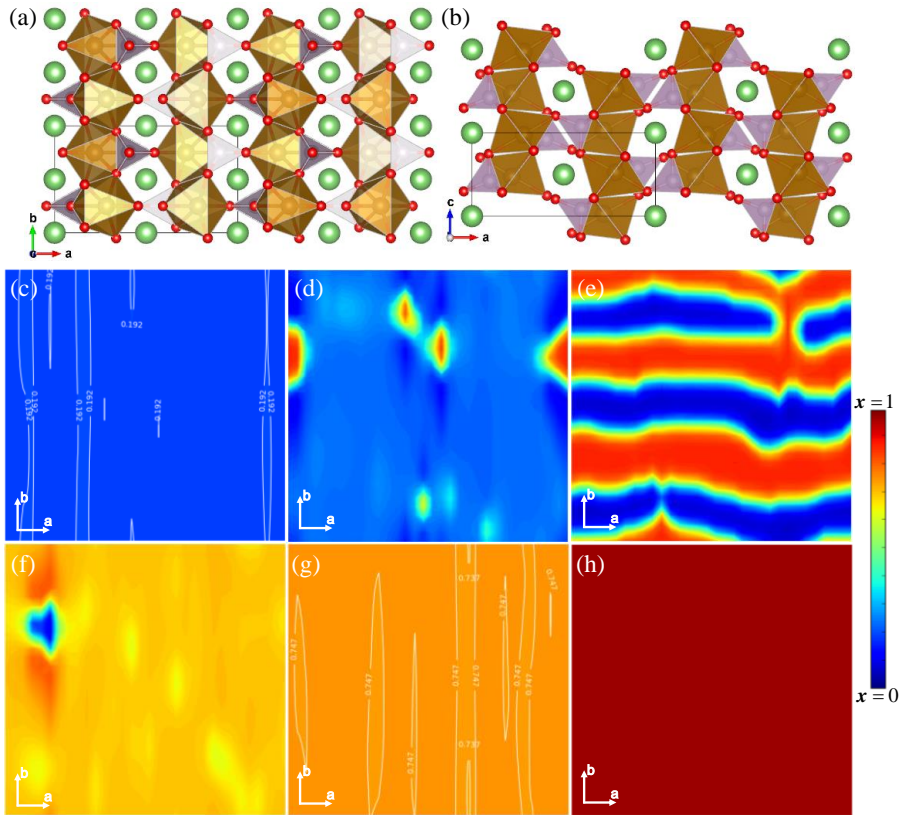


Figure 6.8.2 (a, b) Atomic model for olivine LiFePO_4 along (a) ab and (b) ac planes. (c-h) Phase transformations in the nanodomain with dimensions of 15.17×15.17 nm in Li_xFePO_4 during relaxation from a solid solution at dimensionless time $\hat{t} = 3.0$ and dimensionless current $\hat{I} = 0.0$. As illustrated in Figure 6.8.1d, the initial concentrations lie before, at the middle, and after the spinodal points ($x =$ (c) 0.19, (d) 0.25, (e) 0.5, (f) 0.69, and (g) 0.75), and (h) the middle of the one-phase reaction region at $x = 0.97$.

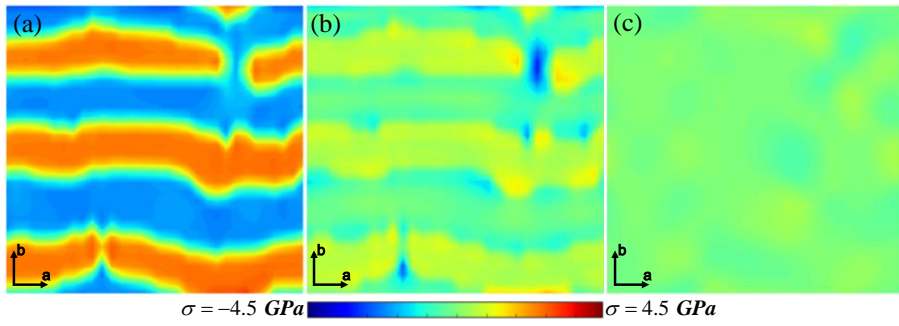


Figure 6.8.3 Elastic stresses (a) σ_a , (b) σ_b , and (c) σ_{ab} during phase transformation from $x = 0.5$ at dimensionless time $\hat{t} = 3.0$ and dimensionless current $\hat{I} = 0.0$.

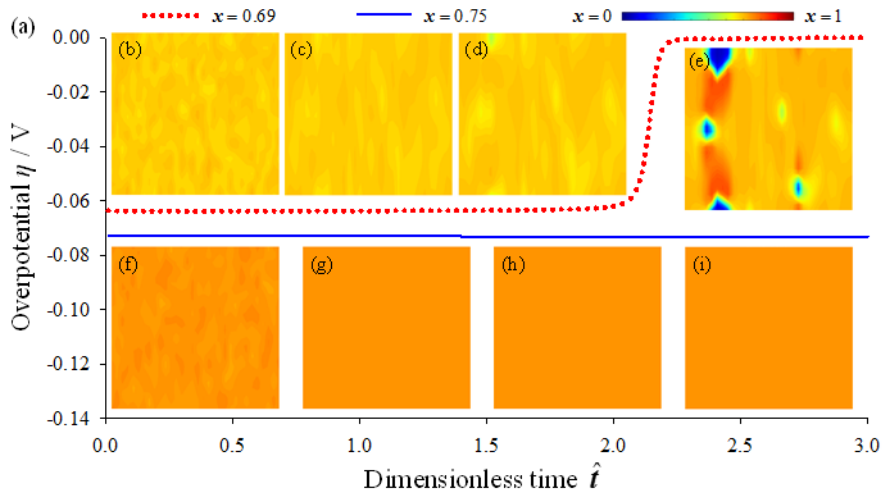


Figure 6.8.4 (a) Overpotential η as a function of dimensionless time \hat{t} for dimensionless current $\hat{I} = 5.0$. Red dotted and blue solid lines indicate overpotential for $x = 0.69$ and 0.75 , respectively. (b-i) Distributions of concentration during phase transformations at $x =$ (b-e) 0.69 (upper row) and (f-i) 0.75 (lower row) for $\hat{t} =$ (b, f) 0.0 , (c, g) 1.0 , (d, h) 2.0 , and (e, i) 3.0 .

6.9 Heterogeneous Structural Distortions in Ni-rich Layered Oxides[26]

Ni-rich transition metal layered oxides ($\text{LiNi}_x\text{Co}_y\text{Mn}_{1-x-y}\text{O}_2$, with $x > 0.5$, Ni-rich NCM) have been spotlighted during the past decade as the most promising candidates for high capacity cathode materials in Li-ion batteries (LIBs) due to their high energy densities ($>200 \text{ mAh g}^{-1}$ until $\sim 4.6 \text{ V vs. Li/Li}^+$). Although $\text{LiNi}_{1/3}\text{Co}_{1/3}\text{Mn}_{1/3}\text{O}_2$ (NCM111) has been successfully commercialized, in order to meet the demand for large-scale energy storage applications such as electric vehicles (EVs) and energy storage systems (ESSs), further NCM research and development has been directed toward enhancing its specific capacity by increasing the ratio of the Ni component toward $\text{LiNi}_{0.8}\text{Co}_{0.1}\text{Mn}_{0.1}\text{O}_2$ (NCM811).[2, 30, 77-80]

While the increase of the Ni ratio in NCM contributes to an enhanced specific discharge capacity, it also results in severe capacity degradation caused by cation mixing, surface side reactions, and crack propagation with structural instability. Nevertheless, micro-crack propagation in the secondary particle related to structural instability remains problematic, although cation mixing and surface deterioration can be prevented through the above-mentioned approaches. Among the promising Ni-rich compounds, severe structural changes and crack propagation have been observed experimentally in $\text{LiNi}_x\text{Co}_y\text{Al}_{1-x-y}\text{O}_2$ (NCA) cathodes.[81, 82] Although, Meng et al. recently reported the experimental observation of micro-crack generation of NCM811 with severe cyclic degradation and suggested surface coating with Li_2TiO_3 to mitigate the crack propagation,[83] the fundamental origin has not been adequately addressed for the Ni-rich NCM cathodes. Moreover, the underlying mechanism for the phase transformation and structural changes in NCM811 is not fully understood. For these reasons, we focused on the study of intrinsic characteristics of the phase transformation and structural changes of NCM811 to elucidate its inherent structural instability regardless of cation mixing and surface deterioration.

For these reasons, we focused on the origins of crack generation from phase transformations and structural distortions in Ni-rich $\text{LiNi}_{0.8}\text{Co}_{0.1}\text{Mn}_{0.1}\text{O}_2$ using multiscale approaches, from first-principles to meso-scale phase-field model. Atomic-scale structure analysis demonstrated that opposite changes in the lattice parameters are observed until the inverse Li content $x = 0.75$; then, structure collapses due to complete extraction of Li from between transition metal layers. Combined-phase investigations represent the highest phase barrier and steepest chemical potential after $x = 0.75$, leading to phase transformations to highly Li-deficient phases with an inactive character. Abrupt phase transformations with heterogeneous structural collapse after $x = 0.81$ ($\sim 220 \text{ mAh g}^{-1}$) were identified in the nanodomain. Further, meso-scale strain distributions show around 5% of anisotropic contraction with lower crack energy release rates, which cause not only micro-crack generations of secondary particles on the interfaces between the contracted primary particles, but also mechanical instability of primary particles from heterogeneous strain changes.

Figure 6.9.1a and 6.9.1b show the atomic model used for the first-principles calculations projected on the bc and ab planes, respectively. The atomic model was developed based on the rhombohedral layered oxide structure ($R\bar{3}m$) of LiNiO_2 (Inorganic Crystal Structure Database (ICSD) ID: 10499). To represent the stoichiometry of NCM811, supercells of $2 \times 2 \times 1$ with 12 $f.u.$ were used; the exact stoichiometry of the supercell in this study is $\text{LiNi}_{0.8333}\text{Co}_{0.0833}\text{Mn}_{0.0833}\text{O}_2$ ($\text{Li}_{12}\text{Ni}_{10}\text{Co}_1\text{Mn}_1\text{O}_{24}$). The model was developed using high-throughput calculations based on a previously described scheme. As shown in Figure 6.9.1a, Co and Mn are located separately in the Ni-rich environment of the layered oxide structure, which would be thermodynamically related to d -electronic stability of the crystal field.[11, 21]

Figure 6.9.2 presents the partial (projected) density of states (PDOSs) of the Ni, Co, and Mn d -orbitals and the O p -orbitals in $\text{Li}_{1.1}\text{Ni}_{0.8}\text{Co}_{0.1}\text{Mn}_{0.1}\text{O}_2$ and

$\text{Li}_0\text{Ni}_{0.8}\text{Co}_{0.1}\text{Mn}_{0.1}\text{O}_2$. In the fully lithiated state ($\text{Li}_1\text{Ni}_{0.8}\text{Co}_{0.1}\text{Mn}_{0.1}\text{O}_2$), the Ni, Co, and Mn *d*-orbitals are shown as Ni^{3+} -like, Co^{3+} , and Mn^{4+} -like shapes due to the effect of the *d*-electronic donor,[38] in agreement with a previous report.[84] The thermodynamic stability of the Co^{3+} and Mn^{4+} crystal fields could be satisfied by maintaining their separate locations. Based on the electronic structures, further, the redox reactions of NCM811 can be understood. Figure 6.9.2 also present the PDOSs of the fully delithiated state ($\text{Li}_0\text{Ni}_{0.8}\text{Co}_{0.1}\text{Mn}_{0.1}\text{O}_2$). The charts reveal Ni^{4+} , Co^{3+} , and Mn^{4+} -like shapes, which indicate that the cationic redox reaction of Ni^{3+} -like to Ni^{4+} is a major cationic redox process. Additionally, Figure 6.9.2d and 6.9.2h indicate a notable anionic redox reaction contribution from O ions. Therefore, the superior electrochemical performance of the Ni-rich NCM can be attributed to the combination of the anionic redox reactions[85, 86] and the cationic redox reactions of the Ni ions in the stable crystal fields of the Co and Mn *d*-orbitals.

From a structural point of view, NCM811 suffers from severe structural changes with anisotropic distortions. Figure 6.9.3a shows the expansion and contraction of the *a* (blue left axis) and *c* (red right axis) lattice parameters as a function of the inverse Li content *x* in $\text{Li}_{1-x}\text{Ni}_{0.8}\text{Co}_{0.1}\text{Mn}_{0.1}\text{O}_2$. In the *a* direction, the lattice decreases gradually throughout the reaction from *x* = 0 to 1, whereas the lattice in the *c* direction shows non-monotonic behavior, increasing from *x* = 0.0 to 0.75 and decreasing thereafter. In other words, the lattice parameters change in opposite directions from *x* = 0.0 to 0.75, but in the same direction thereafter. However, after *x* = 0.75, structural collapse is observed due to the rapid volume reduction, as shown in Figure 6.9.3b, which is caused by the complete extraction of Li from between the transition metal layers. Therefore, the structural changes of NCM811 during electrochemical reactions are likely to be harmful to the cyclic performance due to the lattice distortions in opposing directions ($0.0 < x < 0.75$) and the volumetric collapse ($0.75 < x < 1.0$).

To understand the thermodynamic phase transformations, the phase behaviors were investigated by calculating the DFT mixing enthalpies $H_{DFT}(x)$ with respect to normalized inverse Li content x , as presented in Figure 6.9.4a. Seven ground states are observed, including the initial ($x = 0$) and final ($x = 1$) states. The CP redox reaction of NCM811 consists of two one-phase reactions ($0.0 < x < 0.1667$; $0.3333 < x < 0.4167$) and three two-phase reactions ($0.1667 < x < 0.3333$; $0.4167 < x < 0.75$; $0.75 < x < 1.0$). To predict the electrochemical behavior, Figure 6.9.4b presents the OCVs based on the ground states in Figure 6.9.4a; the shape of the curve is similar to the experimental OCV values for LiNiO_2 estimated previously by the galvanostatic intermittent titration technique (GITT).[87]

By considering the configurational entropy at a finite temperature (300 K), more general phase behaviors can be understood using the CP free energy $f_{CP}(x)$ and the CP chemical potential μ_{CP} , as shown in Figure 6.9.5. Spinodal regions, where two-phase reactions occur, are indicated as green shaded regions in Figure 6.9.5. Figure 6.9.5a shows that the first and second phase barriers from $x = 0.21$ to 0.30 and from $x = 0.50$ to 0.67 are low, but the third phase barrier from $x = 0.81$ to 0.93 is remarkably steep and higher than the others. This means that phase separations are likely to be impeded due to the low phase barriers and the low slopes of the chemical potentials before $x = 0.75$, such that relatively smooth reactions similar to the one-phase reaction can be generated, rather than the two-phase reaction. In contrast, after $x = 0.75$, rapid phase separation by a two-phase reaction is likely to occur as indicated by the higher phase barrier in Figure 6.9.5a and the sharp slope of the chemical potential in Figure 6.9.5b. More importantly, the strong phase separation after $x = 0.75$ results in a highly Li-deficient phase ($\text{Li}_0\text{Ni}_{0.8}\text{Co}_{0.1}\text{Mn}_{0.1}\text{O}_2$), leading to severe structural transformations to inactive phases such as the NiO rock salt phase previously observed by *ex situ*

transmission electron microscopy in Ni-rich NCM.[88]

To describe the meso-scale phase transformations of $\text{LiNi}_{0.8}\text{Co}_{0.1}\text{Mn}_{0.1}\text{O}_2$ in a nanodomain with dimensions of $31.36 \text{ nm} \times 31.36 \text{ nm}$ at 300 K, a phase-field model analysis was conducted. As simulation parameters, we set D as $10^{-8} \text{ cm}^2 \text{ s}^{-1}$ based on an experimental value,[89] λ as 0.49 nm from the interlayer distance of the atomic model, and the ε_i^f values as $\varepsilon_{0.1667}^{0.3333} = 128.66 \text{ eV}$, $\varepsilon_{0.4167}^{0.75} = 7.85 \text{ eV}$, and $\varepsilon_{0.75}^{1.0} = 169.95 \text{ eV}$. The phase transformation simulations were carried out on the ac plane during relaxation from the solid solution at $x = 0.65$ (Figure 6.9.6a) with a theoretical charge capacity of $\sim 179 \text{ mAh g}^{-1}$ and $x = 0.85$ (Figure 6.9.6e) with a theoretical charge capacity of $\sim 234 \text{ mAh g}^{-1}$. The a , c , and volumetric strains (denoted as ε_1 , ε_3 , and ε_V , respectively) are displayed in Figure 6.9.6b ($x = 0.65$) and 6.9.6f ($x = 0.85$), 6.9.6c ($x = 0.65$) and 6.9.6g ($x = 0.85$), and 6.9.6d ($x = 0.65$) and 6.9.6h ($x = 0.85$), respectively. The strains are defined as $\varepsilon_1 = \Delta a/a_{x=0}$, $\varepsilon_3 = \Delta c/c_{x=0}$, and $\varepsilon_V = \Delta V/V_{x=0}$, where a and c are the lattice parameters and V is the volume, respectively. Finally, 2D diffusion in the a and b directions was applied, and the phase separation was triggered by random noise.

From the distribution of the inverse Li concentration, distinct phase separation is observed in Figure 6.9.6e at $x = 0.85$, correlated with the sharp slope of the chemical potential in Figure 6.9.5b, but only slight phase separation is observed in Figure 6.9.6a at $x = 0.65$. For this reason, smooth electrochemical reactions may be possible until $x = 0.65$ ($\sim 179 \text{ mAh g}^{-1}$), but phase separation to an inactive phase ($\text{Li}_0\text{Ni}_{0.8}\text{Co}_{0.1}\text{Mn}_{0.1}\text{O}_2$) should occur at $x = 0.85$ ($\sim 234 \text{ mAh g}^{-1}$), meaning that the third spinodal region from $x = 0.81$ to 0.93 induces intrinsically irreversible characteristics. Furthermore, from a structural perspective, at $x = 0.65$, not only are contraction strains of ε_1 and

ε_3 observed, but also slight differences occur between ε_1 ($-6 \times 10^{-6} < \varepsilon_1 < -6 \times 10^{-7}$) and ε_3 ($0.027 < \varepsilon_3 < 0.028$), as shown in Figure 6.9.6b and 6.9.6c. Fortunately, the extent of structural change can be considered as reasonably small; e.g., the difference in ε_V is less than 4×10^{-4} , as illustrated in Figure 6.9.6d. Severe structural distortions occur at $x = 0.85$. All the absolute changes in the three strains at $x = 0.85$ are remarkably larger than those at $x = 0.65$: ε_1 changes relatively slightly ($-0.032 < \varepsilon_1 < -0.027$), whereas ε_3 and ε_V vary by as much as 5% ($0.018 < \varepsilon_3 < 0.043$, $-0.047 < \varepsilon_V < -0.018$) (Figure 6.9.6f, 6.9.6g, and 6.9.6h, respectively).

In the meso-scale phase transformation phenomena, the structural distortions are heterogeneously generated in the nanodomain due to the blocking of diffusion in the c direction and the rapid phase separation, which is shown in the apparent red and blue regions of Figure 6.9.6f, 6.9.6g, and 6.9.6h. Therefore, the structural changes in NCM811 occur more severely in the third spinodal region, and, combined with the abrupt phase separation, limit the intrinsic specific capacity to less than 220 mAh g⁻¹ for $x = 0.81$. As shown in Figure 6.9.7, the around 5% of anisotropic contraction and the ~3.9% of average contraction (Figure 6.9.6h) in the nanodomain would cause the contraction of each primary particle, and then the gaps between the primary particles would result in the micro-crack generations in the secondary particles on the interfaces between the primary particles, which could be the origins and mechanism on the experimental observations of the micro-crack propagations.[81-83] Further, the heterogeneous distribution of the anisotropic strain changes causes the severe mechanical instability of the primary particles that could induce the generation of nano-cracks, which could be a crack opening of the micro-cracks.

In addition, critical energy release rates of $\text{Li}_1\text{Ni}_{0.8}\text{Co}_{0.1}\text{Mn}_{0.1}\text{O}_2$ and

$\text{Li}_0\text{Ni}_{0.8}\text{Co}_{0.1}\text{Mn}_{0.1}\text{O}_2$ calculated by DFT, which describe the critical energy for the crack generation and are related to the surface energy γ for brittle materials ($G_c = 2\gamma$) based on Griffith's theory. Though fully-lithiated NCM811 has low G_c (2.4308 J m^{-2}), the delithiated NCM811 has even lower G_c (-0.0064 J m^{-2}), which would result from the increasing repulsions between layers at lower Li concentrations. In other words, not only NCM811 is fragile to crack generation, but also it gets weakened at delithiated states, which means the 5% of anisotropic contraction could be enough to generate crack propagations.

In summary, the intrinsic limitations of a Ni-rich NCM811 cathode material were investigated in terms of its phase transformations and structural distortions using multiscale approaches combining first-principles calculations and the CP phase-field model. The major redox mechanism of NCM811 was determined as a combination of the cationic redox reactions of Ni with the anionic redox reactions of O. The atomic-scale structural analysis showed that opposite lattice changes are generated until $x = 0.75$, followed thereafter by the gradual decrease all of the lattice parameters due to the collapse of the transition metal layers. The CP behaviors represent the three two-phase reaction regions, wherein the third exhibits a higher phase barrier and a sharp rise in the chemical potential. This causes rapid phase separation, forming an inactive and highly Li-deficient phase. In the meso-scale phase transformation, heterogeneous phase separations are observed, and severe phase transformation occurs near the third spinodal region at $x = 0.85$. Further, the $\sim 3.9 \%$ of the average contraction and lower critical energy release rates including the heterogeneous distribution of the anisotropic strain changes observed by the meso-scale strain distributions could induce not only the nano-cracks in the nanodomain of the primary particles from the severe mechanical instability, but also the micro-crack generations on the interfaces between the contracted primary particles. Thus, the combination of the abrupt

transformations to inactive phases with the heterogeneous collapse of the layered structure limits the intrinsic performance of NCM811. These findings may help to predict the maximum performance of Ni-rich NCM cathodes, and the mechanistic insights on the phase transformations and structural distortions could provide clues toward improving cathode materials for battery applications. As for the combined-phase transformation model developed in the work, a calculation domain is limited to the bulk region in the middle of particle as shown in Figure 6.9.7. Therefore, this methodology could be more applicable to investigate entire particles by developing this model for surface and interface regions.

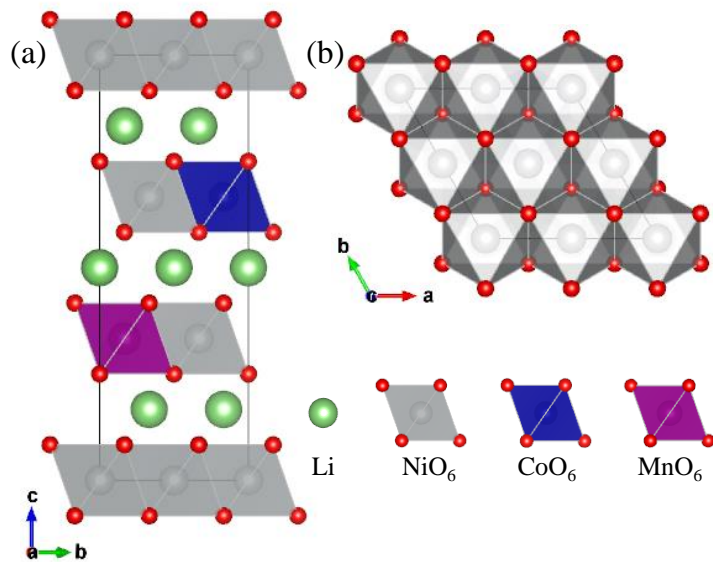


Figure 6.9.1 Atomic models of Ni-rich $\text{LiNi}_{0.8}\text{Co}_{0.1}\text{Mn}_{0.1}\text{O}_2$ (NCM811) layered oxide ($R\text{-}3m$) projected onto the (a) bc and (b) ab planes.

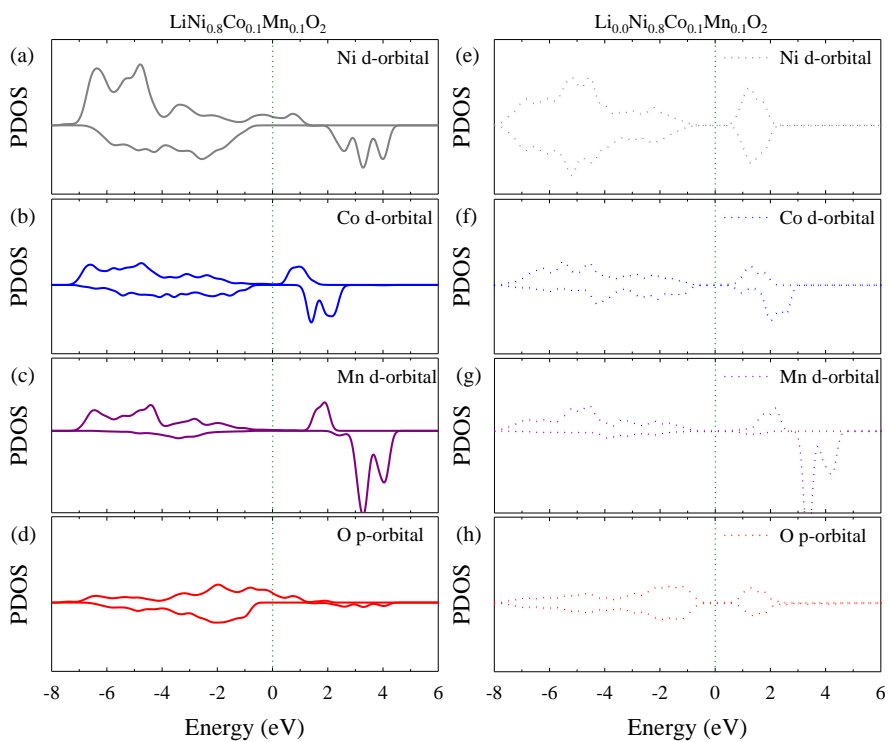


Figure 6.9.2 (a, b, c, d) Partial density of states (PDOSs) of (a) Ni *d*- (gray solid line), (b) Co *d*- (blue solid line), (c) Mn *d*- (purple solid line), and (d) O *p*- (red solid line) orbitals in $\text{LiNi}_{0.8}\text{Co}_{0.1}\text{Mn}_{0.1}\text{O}_2$. (e, f, g, h) PDOSs of (e) Ni *d*- (gray dashed line), (f) Co *d*- (blue dashed line), (g) Mn *d*- (purple dashed line), and (h) O *p*- (red dashed line) orbitals in $\text{Li}_{0.0}\text{Ni}_{0.8}\text{Co}_{0.1}\text{Mn}_{0.1}\text{O}_2$. The Fermi level is 0.0 eV (green dotted line).

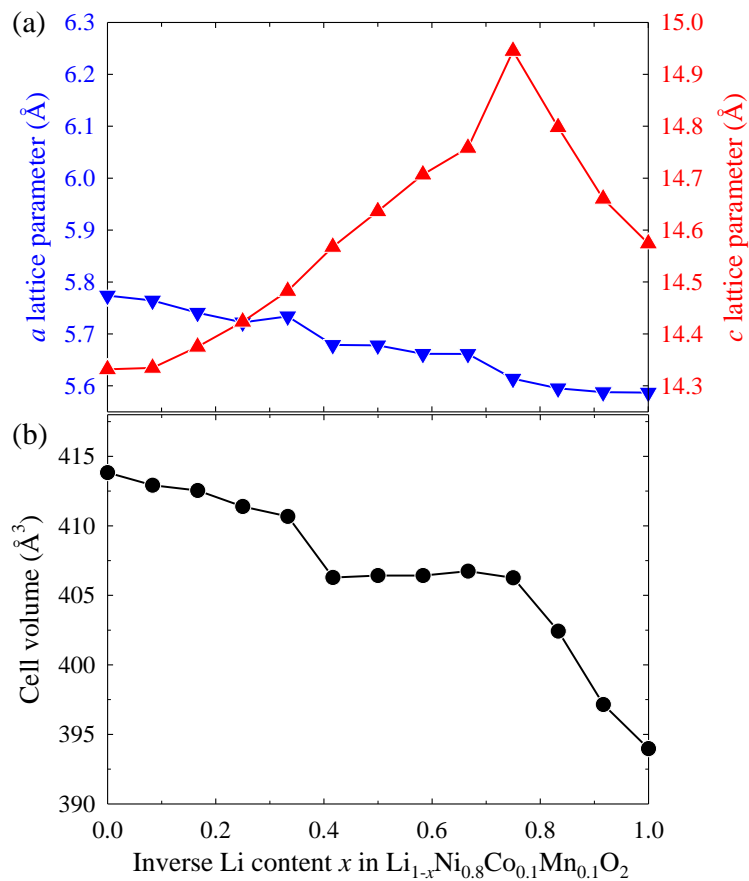


Figure 6.9.3 (a) Calculated a (blue inverse triangles and solid line, left axis) and c lattice parameters (red triangles and solid line, right axis), and (b) volume of cell (black circles and solid line) with respect to the inverse Li content x in $\text{Li}_{1-x}\text{Ni}_{0.8}\text{Co}_{0.1}\text{Mn}_{0.1}\text{O}_2$.

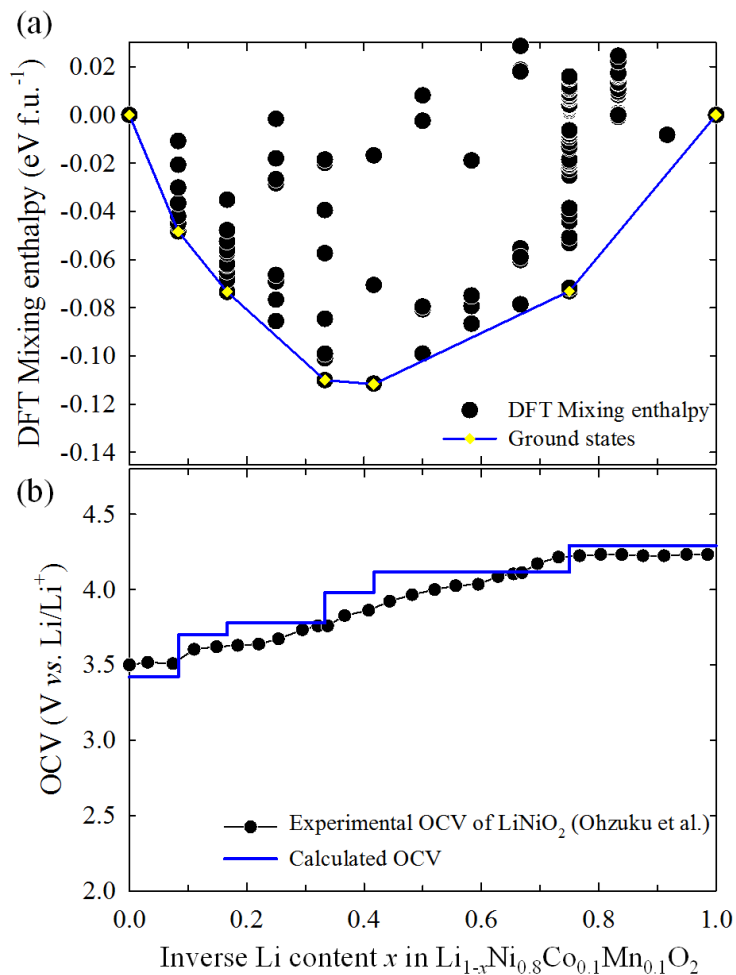


Figure 6.9.4 (a) Mixing enthalpies from density functional theory (DFT) calculations (black circles) with ground states (yellow diamonds and blue line). (b) Open-circuit voltage (OCV) calculated using first principles (blue solid line) and reproduced by experiment (black circles and line) from Ohzuku et al.[87] versus inverse Li content x in $\text{Li}_{1-x}\text{Ni}_{0.8}\text{Co}_{0.1}\text{Mn}_{0.1}\text{O}_2$.

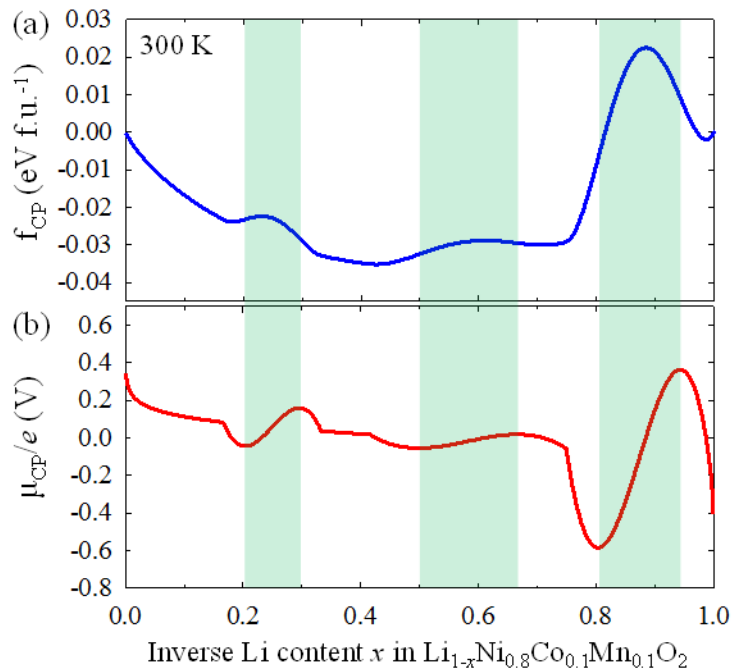


Figure 6.9.5 (a) Combined-phase (CP) free energy (blue solid line) and (b) CP chemical potential (red solid line) at room temperature (300 K) with spinodal regions (green shaded areas) with respect to inverse Li content x in $\text{Li}_{1-x}\text{Ni}_{0.8}\text{Co}_{0.1}\text{Mn}_{0.1}\text{O}_2$.

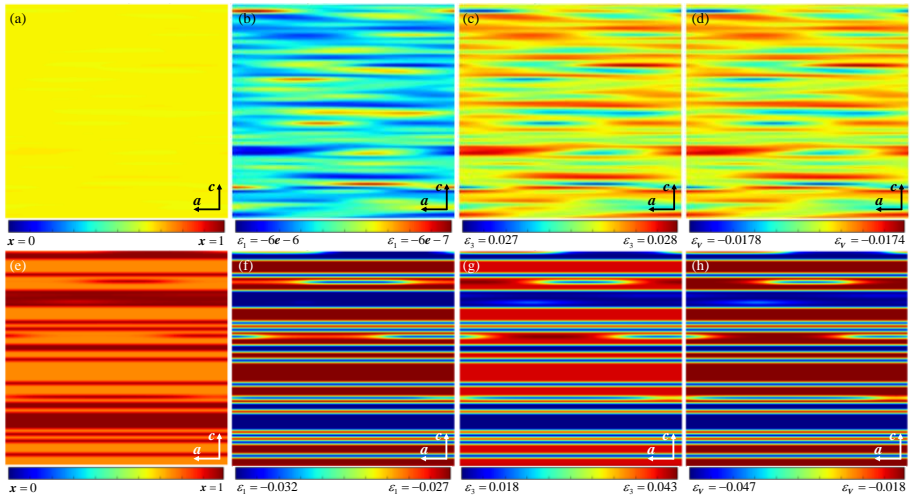


Figure 6.9.6 Meso-scale phase transformations in the nanodomain with dimensions of 31.36×31.36 nm in $\text{Li}_{1-x}\text{Ni}_{0.8}\text{Co}_{0.1}\text{Mn}_{0.1}\text{O}_2$ at room temperature (300 K) from a solid solution of inverse Li concentration $x = 0.65$ (a, b, c, d) and 0.85 (e, f, g, h) at dimensionless time $\hat{t} = 5$. (a, e), (b, f), (c, g), and (d, h) are the distributions on the ac plane of the inverse Li concentration x , strain in a direction ε_1 , strain in c direction ε_3 , and volumetric strain ε_V , respectively.

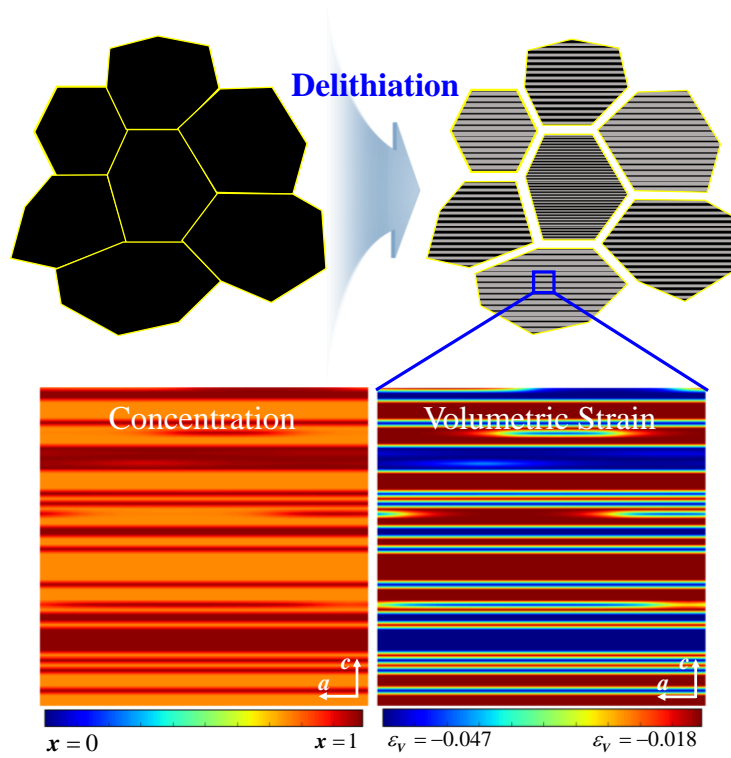


Figure 6.9.7 Schematic illustration of micro-crack generations in secondary particles on the interfaces of the contracted primary particles during delithiation.

6.10 Suppression of Fractures in Ni-rich Layered Oxides

To suppress the crack generation of NCM811, we devised Ti bulk doping to enhance structural stability. Figure 6.10.1 shows atomic models of NCM811 and Ti-doped NCM811 (Ti-NCM811). From the thermodynamic comparison for the position of Ti atom in NCM811 in Figure 6.10.1e. Ti-substitution in Ni layer is most favorable position of Ti atom as shown in Figure 6.10.1b. Furthermore, we developed surface atomic models for NCM811 (Figure 6.10.1f) and Ti-NCM811 (Figure 6.10.1g) for estimating critical energy release rate for crack simulations as shown in Figure 6.10.1f and 6.10.1g, respectively.

To investigate structural distortion of both materials, a and c lattice parameters and volume of atomic cell were described in Figure 6.10.2. Ti-NCM811 has a slightly expanded structure than that of NCM811 in both a and c directions as shown in Figure 6.10.2a and 6.10.2b. From the expansion of both lattice parameters, volume of Ti-NCM811 is also expanded than that of NCM811 as represented in Figure 6.10.2c. More importantly, the change of volume versus fully lithiated ($x = 0$) and fully delithiated ($x = 1$) states is much reduced in Ti-NCM811 than that of NCM811, and structural collapse in the c direction is also mitigated in Ti-NCM811 than that of NCM811. These could be a helpful to the structural stability of Ti-NCM811.

Furthermore, mixing enthalpies calculated by DFT thermodynamic calculations, and CP free energy and chemical potential were evaluated for simulating phase transformation, mechanical stresses, and crack generations as shown in Figure 6.10.3. Figure 6.10.3a and 6.10.3b represent strong phase separation of NCM811 from $x = 0.75$ to 1.0 is much decreased in Ti-NCM811, which is connected to the CP free energy in Figure 6.10.3c. CP free energy of NCM811 has a far higher phase barrier from $x = 0.75$ to 1.0 than that of Ti-NCM811, and CP chemical potential of NCM811 has a much sharp shape than that of Ti-NCM811 as shown in Figure 6.10.3c and 6.10.3d, respectively.

On the basis of these thermodynamic results, phase separation of NCM811 can be much severe than that of Ti-NCM811, which causes larger elastic stresses and generation of fracture.

Through multiscale mechanics simulation for concentration, elastic stresses, and fractures, Figure 6.10.4 shows distributions of concentration of inverse Li content x , elastic stresses in a and c directions, and crack phase field c for both NCM811 and Ti-NCM811 in the nanodomain with dimensions of 31.36×31.36 nm at room temperature (300 K) from a solid solution of inverse Li concentration $x = 0.85$ at dimensionless time $\hat{t} = 3$. As predicted before, strong phase separation of NCM811 and bare phase separation of Ti-NCM811 were observed in Figure 6.10.4a and 6.10.4e. Due to this difference of phase transformation behaviors, elastic stresses are also strongly applied to NCM811 than that of Ti-NCM811 as shown in Figure 6.10.4b, 6.10.4c, 6.10.4f, and 6.10.4g. Finally, although crack generation is observed in NCM811 as described in Figure 6.10.4d, fracture in Ti-NCM811 is suppressed as simulated in Figure 6.10.4h, which is in agreement with the reported experiment of Du et al.[90], who thoroughly studied the generation and suppression mechanisms of fractures.

In summary, Ti doping in Ni-rich NCM811 is effective to suppress structural distortion, stress generation and fracture, which is investigated by multiscale mechanics approaches from first-principles calculation, surface prediction, statistical thermodynamics, phase field model, mechanical equilibrium by finite element method, and phase field crack model. Structural stability can be guaranteed by much lower expansion of lattice parameter and volume of cell in Ti-NCM811 than those of NCM811. Thermodynamic parameters at room temperature shows lower phase barrier of Ti-NCM811 than that of NCM811, which is responsible for suppress phase separations of Ti-NCM811. From the mesoscale continuum simulations, strong phase

separation of NCM811 and bare phase separation of Ti-NCM811 were observed. From this difference of phase transformation behaviors, elastic stresses are strongly applied to NCM811 than that of Ti-NCM811. Finally, although crack generation is observed in NCM811, fracture in Ti-NCM811 is suppressed as simulated. This multiscale mechanics framework for predicting mechanical failure in electrochemical materials could be a strong tool to develop and design the improved and new electrode materials for electrochemical energy storages.

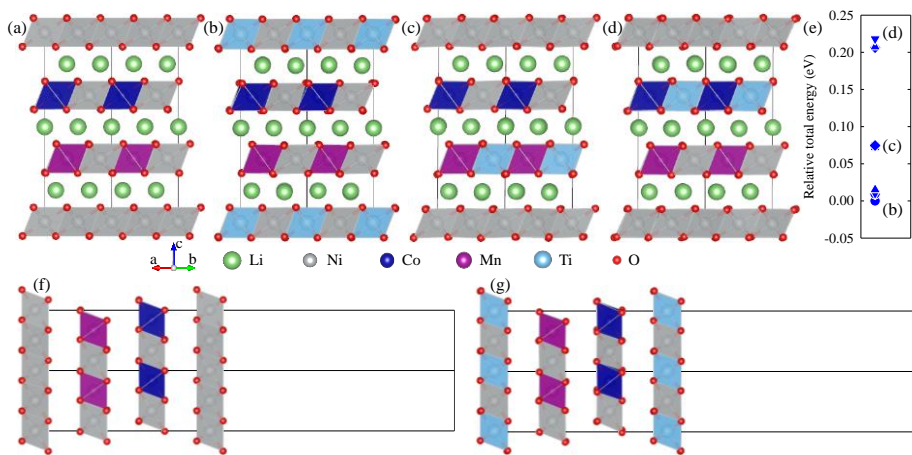


Figure 6.10.1 Atomic models of (a) Ni-rich $\text{LiNi}_{0.833}\text{Co}_{0.083}\text{Mn}_{0.083}\text{O}_2$ (NCM811) and (b-d) Ti-doped NCM811 (Ti-NCM811) with three different Ti positions; (b) Ni layer, (c) Ni-Mn layer, and (d) Ni-Co layer. (e) Relative total energy of the three different Ti-NCM811. Surface atomic models of (f) NCM811 and (g) Ti-NCM811.

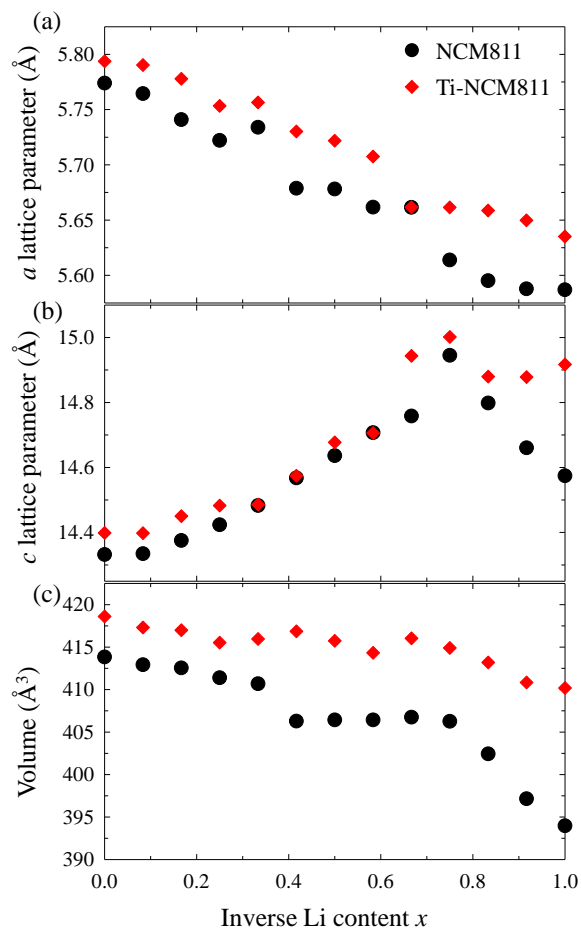


Figure 6.10.2 Calculated (a) a and (b) c lattice parameters, and (c) volume of cell with respect to the inverse Li content x .

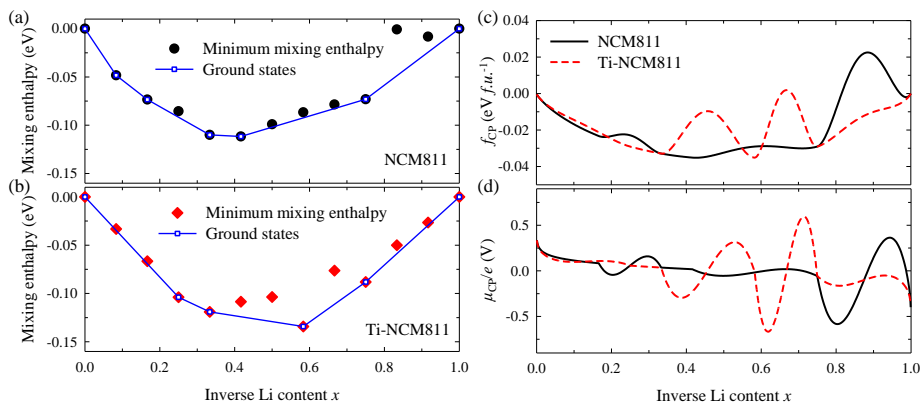


Figure 6.10.3 Mixing enthalpies from density functional theory (DFT) calculations of (a) NCM811 and (b) Ti-NCM811, and (c) combined-phase (CP) free energy and (d) CP chemical potential at room temperature (300 K) with respect to inverse Li content x .

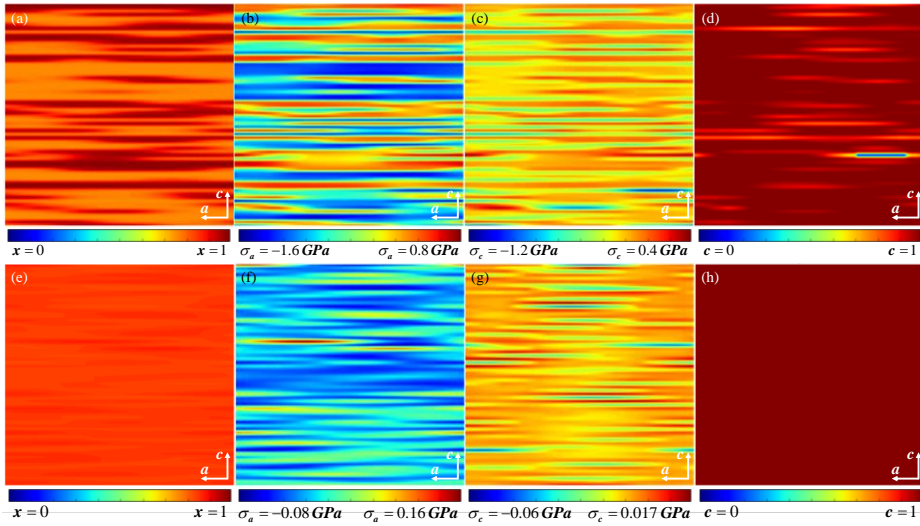


Figure 6.10.4 Distributions of (a, e) concentration of inverse Li content x , elastic stresses in (b, f) a and (c, g) c directions, and (d, h) crack phase field c for both (a, b, c, d) NCM811 and (e, f, g, h) Ti-NCM811 in the nanodomain at room temperature (300 K) from a solid solution of inverse Li concentration $x = 0.85$ at dimensionless time $\hat{t} = 3$.

Chapter 7

Conclusions and Recommendation

This dissertation is mainly focused on the mechanics-based multiscale design and experimental realization of the electrodes for electrochemical energy storages such as Li-ion batteries. By utilizing multiscale approaches from first-principles calculations, statistical thermodynamics, atomic surface dissolution, phase field model, to continuum theory, this combined methodology between multiscale and mechanics approaches deals with the atomic physics and chemistry including electronic structures, nanoscale thermodynamics and kinetics, particle-level phase transformation, stress generation and mechanical deformation, and finally crack generation and propagation. This methodology has a strong advantage for investigating the electrodes for electrochemical energy storages, because the electrochemical performances of the electrodes are closely related to from the physical and chemical properties in atomic-scale, electrochemical phase transformation in mesoscale, mechanical deformation and failure in macroscale. To establish the mechanics-based multiscale framework, we introduced density functional theory calculation for calculating atomic thermodynamics and kinetics, and

electronic structure analysis, phase field model using Cahn-Hilliard equation for describing the concentration distribution, mechanical equilibrium using finite element procedure for evaluating stress distribution, and phase field crack model for development of crack generation and propagation, which are fully coupled in this framework.

More importantly, this methodology was developed to deal with complex phase transformations, which is frequently observed from the electrodes during charge and discharge processes, by defining the total free energy functional for the combined-phase reactions. Many kinds of electrodes involving ionic migrations during operations suffer from complicated phase transformations with the combined-phase reactions. By establishing governing equations for phase transformation, mechanical equilibrium, and crack generation based on this combined-phase free energy functional, diverse derived formulations can appropriately reflect these combined-phase transformations.

Using this mechanics-based multiscale framework, we investigated and designed major cathode materials for Li-ion battery. For high energy materials with large capacity and high operating voltage, Li-rich oxides were fundamentally investigated, and on the basis of this understanding, oxygen-defected and TM-doped Li-rich oxides were theoretically designed and investigated, and experimentally realized and validated. The origins and mechanism of severe phase transformation of Li_2MnO_3 was understood, and, as solutions, oxygen vacancy, and doping of TMs with reduced character such as Ni and Cu. Additionally, Cu doping has a role to generate p-type conductivity, which results in enhanced electronic conductivity and increased specific energy. For high power materials, conventional spinel and high-voltage spinel oxides were fundamentally understood and modified in the both calculation and experiments. Al doping for LiMn_2O_4 spinel cathode is improved cyclic stability by suppressing unfavorable phase transformation to

inactive phases. For the $\text{LiNi}_{0.5}\text{Mn}_{1.5}\text{O}_4$ high voltage spinel, two different doping approaches were applied. First, surface doping of Ti to suppress TM dissolution at surfaces was chosen by first-principles surface calculations and experimentally validated, which reduces the amount of TM dissolution and improve cyclic performance. Second, Ti bulk doping enhances the power characteristics by enhancing structural stability, expanding atomic structure, and soften elastic properties. To unfold the relationship between electrochemical characteristics, and phase transformation, we applied our multiscale method to olivine LiFePO_4 cathode, and figured out different electrochemical states with respect to degrees of phase separation. For high capacity cathodes, Ni-rich layered oxides were investigated in terms of anisotropic structural distortion, heterogeneous phase transformation, and intrinsic crack generation. Further, Ti doping was suggested to suppress the fractures.

Above designed and realized cathode materials have a meaning of not only the effectiveness of as-developed mechanics-based multiscale methodologies, but also affirmative examples of experimental realizations from theoretical design without empirical approaches. As a strength of this methodology, the foundation of this framework lies on the combined-phase free energy functional determined by thermodynamic calculations of first-principles, and this free energy functional governing fundamental physics and chemistry of the system has a diverse applicability to many kinds of computational theories such as the phase field model, electrochemical kinetics, micro-mechanics models, and continuum models for the experimentally undescribed cases attributed to complex phase behaviors. Further, the present model could be applied to various electrode systems such as batteries, capacitors, fuel cells, solar cells, and even catalyst for improving their performances and designing modified and new materials.

Bibliography

- [1] J.M. Lim, K. Cho, M. Cho, Phase transformations with stress generations in electrochemical reactions of electrodes: Multiscale-based mechanics for combined-phase reactions, *Extreme Mechanics Letters*, <http://dx.doi.org/10.1016/j.eml.2016.10.008> (2016).
- [2] M. Armand, J.M. Tarascon, Building better batteries, *Nature*, 451 (2008) 652-657.
- [3] J.M. Tarascon, M. Armand, Issues and challenges facing rechargeable lithium batteries, *Nature*, 414 (2001) 359-367.
- [4] A. Van der Ven, M.K. Aydinol, G. Ceder, G. Kresse, J. Hafner, First-principles investigation of phase stability in Li_xCoO_2 , *Phys Rev B*, 58 (1998) 2975-2987.
- [5] F. Zhou, C.A. Marianetti, M. Cococcioni, D. Morgan, G. Ceder, Phase separation in Li_xFePO_4 induced by correlation effects, *Phys Rev B*, 69 (2004) 201101.
- [6] R. Malik, F. Zhou, G. Ceder, Kinetics of non-equilibrium lithium incorporation in LiFePO_4 , *Nat Mater*, 10 (2011) 587-590.
- [7] R. Malik, F. Zhou, G. Ceder, Phase diagram and electrochemical properties of mixed olivines from first-principles calculations, *Phys Rev B*, 79 (2009) 214201.
- [8] F. Zhou, T. Maxisch, G. Ceder, Configurational electronic entropy and the phase diagram of mixed-valence oxides: The case of Li_xFePO_4 , *Phys Rev Lett*, 97 (2006) 155704.
- [9] G. Ceder, A. Van der Ven, Phase diagrams of lithium transition metal oxides: investigations from first principles, *Electrochim Acta*, 45 (1999) 131-150.
- [10] E. Lee, K.A. Persson, Structural and Chemical Evolution of the Layered Li-Excess Li_xMnO_3 as a Function of Li Content from First-Principles

Calculations, *Adv Energy Mater*, 4 (2014) 1400498.

[11] J.M. Lim, D. Kim, Y.G. Lim, M.S. Park, Y.J. Kim, M. Cho, K. Cho, The origins and mechanism of phase transformation in bulk Li_2MnO_3 : first-principles calculations and experimental studies, *J Mater Chem A*, 3 (2015) 7066-7076.

[12] J. Reed, G. Ceder, A. Van der Ven, Layered-to-spinel phase transition in Li_xMnO_2 , *Electrochem Solid St*, 4 (2001) A78-A81.

[13] P. Bai, D.A. Cogswell, M.Z. Bazant, Suppression of Phase Separation in LiFePO_4 Nanoparticles During Battery Discharge, *Nano Lett*, 11 (2011) 4890-4896.

[14] D. Burch, M.Z. Bazant, Size-Dependent Spinodal and Miscibility Gaps for Intercalation in Nanoparticles, *Nano Lett*, 9 (2009) 3795-3800.

[15] D.A. Cogswell, M.Z. Bazant, Coherency Strain and the Kinetics of Phase Separation in LiFePO_4 Nanoparticles, *Acs Nano*, 6 (2012) 2215-2225.

[16] D.A. Cogswell, M.Z. Bazant, Theory of Coherent Nucleation in Phase-Separating Nanoparticles, *Nano Lett*, 13 (2013) 3036-3041.

[17] M.J. Welland, D. Karpeyev, D.T. O'Connor, O. Heinonen, Miscibility Gap Closure, Interface Morphology, and Phase Microstructure of 3D Li_xFePO_4 Nanoparticles from Surface Wetting and Coherency Strain, *Acs Nano*, 9 (2015) 9757-9771.

[18] G.K. Singh, G. Ceder, M.Z. Bazant, Intercalation dynamics in rechargeable battery materials: General theory and phase-transformation waves in LiFePO_4 , *Electrochim Acta*, 53 (2008) 7599-7613.

[19] P. Zuo, Y.-P. Zhao, Phase field modeling of lithium diffusion, finite deformation, stress evolution and crack propagation in lithium ion battery, *Extreme Mechanics Letters*, 9 (2016) 467-479.

[20] J.M. Lim, D. Kim, Y.G. Lim, M.S. Park, Y.J. Kim, M. Cho, K. Cho, Mechanism of Oxygen Vacancy on Impeded Phase Transformation and Electrochemical Activation in Inactive Li_2MnO_3 , *Chemelectrochem*, 3 (2016)

943-949.

[21] J.M. Lim, D. Kim, M.S. Park, M. Cho, K. Cho, Underlying mechanisms of the synergistic role of Li_2MnO_3 and $\text{LiNi}_{1/3}\text{Co}_{1/3}\text{Mn}_{1/3}\text{O}_2$ in high-Mn, Li-rich oxides, *Phys Chem Chem Phys*, 18 (2016) 11411-11421.

[22] J.M. Lim, T. Hwang, M.S. Park, M. Cho, K. Cho, Design of a p-type Electrode for Enhancing Electronic Conduction in High-Mn, Li-rich Oxides, *Chemistry of Materials*, 28 (2016) 8201-8209.

[23] D. Kim, J.M. Lim, M.S. Park, K. Cho, M. Cho, Phase Separation and d Electronic Orbitals on Cyclic Degradation in Li-Mn-O Compounds: First-Principles Multiscale Modeling and Experimental Observations, *Acs Appl Mater Inter*, 8 (2016) 16631-16639.

[24] J.M. Lim, R.G. Oh, D. Kim, W. Cho, K. Cho, M. Cho, M.S. Park, Design of Surface Doping for Mitigating Transition Metal Dissolution in $\text{LiNi}_{0.5}\text{Mn}_{1.5}\text{O}_4$ Nanoparticles, *Chemsuschem*, 9 (2016) 2967-2973.

[25] J.M. Lim, R.G. Oh, W. Cho, K. Cho, M. Cho, M.S. Park, Power characteristics of spinel cathode correlated with elastic softness and phase transformation for high-power lithium-ion batteries, *J Mater Chem A*, In revision (2016).

[26] J.-M. Lim, T. Hwang, M.-S. Park, M. Cho, K. Cho, Design of a p-type electrode for enhancing electronic conduction in high-Mn, Li-rich oxides, *Chem Mater*, 28 (2016) 8201.

[27] J. Yan, J. Zhang, Y.C. Su, X.G. Zhang, B.J. Xia, A novel perspective on the formation of the solid electrolyte interphase on the graphite electrode for lithium-ion batteries, *Electrochim Acta*, 55 (2010) 1785-1794.

[28] L.L. Luo, J.S. Wu, J.Y. Luo, J.X. Huang, V.P. Dravid, Dynamics of Electrochemical Lithiation/Delithiation of Graphene-Encapsulated Silicon Nanoparticles Studied by In-situ TEM (vol 4, pg 3863, 2014), *Sci Rep-Uk*, 4 (2014) 04322.

[29] B. Song, T. Sui, S.Q. Ying, L. Li, L. Lu, A.M. Korsunsky, *Nano-*

structural changes in Li-ion battery cathodes during cycling revealed by FIB-SEM serial sectioning tomography, *J Mater Chem A*, 3 (2015) 18171-18179.

[30] B. Dunn, H. Kamath, J.M. Tarascon, Electrical Energy Storage for the Grid: A Battery of Choices, *Science*, 334 (2011) 928-935.

[31] P. Hohenberg, W. Kohn, Inhomogeneous Electron Gas, *Phys Rev B*, 136 (1964) B864.

[32] W. Kohn, L.J. Sham, Self-Consistent Equations Including Exchange and Correlation Effects, *Phys Rev*, 140 (1965) 1133.

[33] J.P. Perdew, J.A. Chevary, S.H. Vosko, K.A. Jackson, M.R. Pederson, D.J. Singh, C. Fiolhais, Atoms, Molecules, Solids, and Surfaces - Applications of the Generalized Gradient Approximation for Exchange and Correlation, *Phys Rev B*, 46 (1992) 6671-6687.

[34] J.P. Perdew, K. Burke, M. Ernzerhof, Generalized gradient approximation made simple, *Phys Rev Lett*, 77 (1996) 3865-3868.

[35] G. Kresse, J. Furthmuller, Efficiency of ab-initio total energy calculations for metals and semiconductors using a plane-wave basis set, *Comp Mater Sci*, 6 (1996) 15-50.

[36] J. Hubbard, Electron Correlations in Narrow Energy Bands, *Proc R Soc Lon Ser-A*, 276 (1963) 238-+.

[37] D. Kim, J.M. Lim, Y.G. Lim, M.S. Park, Y.J. Kim, M. Cho, K. Cho, Understanding of Surface Redox Behaviors of Li_2MnO_3 in Li-Ion Batteries: First-Principles Prediction and Experimental Validation, *Chemsuschem*, 8 (2015) 3255-3262.

[38] D. Kim, J.M. Lim, Y.G. Lim, J.S. Yu, M.S. Park, M. Cho, K. Cho, Design of Nickel-rich Layered Oxides Using d Electronic Donor for Redox Reactions, *Chemistry of Materials*, 27 (2015) 6450-6456.

[39] Y.G. Lim, D. Kim, J.M. Lim, J.S. Kim, J.S. Yu, Y.J. Kim, D. Byun, M. Cho, K. Cho, M.S. Park, Anti-fluorite Li_6CoO_4 as an alternative lithium source for lithium ion capacitors: an experimental and first principles study, *J*

Mater Chem A, 3 (2015) 12377-12385.

[40] M.K. Aydinol, A.F. Kohan, G. Ceder, K. Cho, J. Joannopoulos, Ab initio study of lithium intercalation in metal oxides and metal dichalcogenides, Phys Rev B, 56 (1997) 1354-1365.

[41] T. Kawamura, A. Kimura, M. Egashira, S. Okada, J.I. Yamaki, Thermal stability of alkyl carbonate mixed-solvent electrolytes for lithium ion cells, J Power Sources, 104 (2002) 260-264.

[42] G. Henkelman, B.P. Uberuaga, H. Jonsson, A climbing image nudged elastic band method for finding saddle points and minimum energy paths, J Chem Phys, 113 (2000) 9901-9904.

[43] G.L.W. Hart, R.W. Forcade, Algorithm for generating derivative structures, Phys Rev B, 77 (2008) 224115.

[44] H.C. Yu, C. Ling, J. Bhattacharya, J.C. Thomas, K. Thornton, A. Van der Ven, Designing the next generation high capacity battery electrodes, Energ Environ Sci, 7 (2014) 1760-1768.

[45] H. Bethe, Thermal division in crystals, Ann Phys-Berlin, 3 (1929) 133-208.

[46] J.H. Van Vleck, Theory of the variations in paramagnetic anisotropy among different salts of the iron group, Phys Rev, 41 (1932) 208-215.

[47] B.C. Han, A. Van der Ven, D. Morgan, G. Ceder, Electrochemical modeling of intercalation processes with phase field models, Electrochim Acta, 49 (2004) 4691-4699.

[48] L.Q. Chen, Phase-field models for microstructure evolution, Annual Review of Materials Research, 32 (2002) 113-140.

[49] A.J. Bray, Theory of Phase-Ordering Kinetics, Adv Phys, 43 (1994) 357-459.

[50] J. Rana, M. Stan, R. Kloepsch, J. Li, G. Schumacher, E. Welter, I. Zizak, J. Banhart, M. Winter, Structural Changes in Li_2MnO_3 Cathode Material for Li- Ion Batteries, Adv Energy Mater, 4 (2014) 1300998.

- [51] Y.U. Wang, Y.M.M. Jin, A.G. Khachaturyan, Phase field microelasticity theory and simulation of multiple voids and cracks in single crystals and polycrystals under applied stress, *J Appl Phys*, 91 (2002) 6435-6451.
- [52] C. Miehe, M. Hofacker, F. Welschinger, A phase field model for rate-independent crack propagation: Robust algorithmic implementation based on operator splits, *Comput Method Appl M*, 199 (2010) 2765-2778.
- [53] M.J. Borden, C.V. Verhoosel, M.A. Scott, T.J.R. Hughes, C.M. Landis, A phase-field description of dynamic brittle fracture, *Comput Method Appl M*, 217 (2012) 77-95.
- [54] R.J. Xiao, H. Li, L.Q. Chen, Density Functional Investigation on Li_2MnO_3 , *Chemistry of Materials*, 24 (2012) 4242-4251.
- [55] R. Wang, X.Q. He, L.H. He, F.W. Wang, R.J. Xiao, L. Gu, H. Li, L.Q. Chen, Atomic Structure of Li_2MnO_3 after Partial Delithiation and Relithiation, *Adv Energy Mater*, 3 (2013) 1358-1367.
- [56] M. Sathiya, K. Ramesha, G. Rouse, D. Foix, D. Gonbeau, A.S. Prakash, M.L. Doublet, K. Hemalatha, J.M. Tarascon, High Performance $\text{Li}_2\text{Ru}_{1-y}\text{Mn}_y\text{O}_3$ ($0.2 \leq y \leq 0.8$) Cathode Materials for Rechargeable Lithium-Ion Batteries: Their Understanding, *Chemistry of Materials*, 25 (2013) 1121-1131.
- [57] J. Cabana, C.S. Johnson, X.Q. Yang, K.Y. Chung, W.S. Yoon, S.H. Kang, M.M. Thackeray, C.P. Grey, Structural complexity of layered-spinel composite electrodes for Li-ion batteries, *J Mater Res*, 25 (2010) 1601-1616.
- [58] C.S. Johnson, N. Li, J.T. Vaughey, S.A. Hackney, M.M. Thackeray, Lithium-manganese oxide electrodes with layered-spinel composite structures $x\text{Li}_2\text{MnO}_3 \cdot (1-x)\text{Li}_{1+y}\text{Mn}_{2-y}\text{O}_4$ ($0 < x < 1$, $0 \leq y \leq 0.33$) for lithium batteries, *Electrochem Commun*, 7 (2005) 528-536.
- [59] S.F. Amalraj, B. Markovsky, D. Sharon, M. Talianker, E. Zinigrad, R. Persky, O. Haik, J. Grinblat, J. Lampert, M. Schulz-Dobrick, A. Garsuch, L. Burlaka, D. Aurbach, Study of the electrochemical behavior of the "inactive" Li_2MnO_3 , *Electrochim Acta*, 78 (2012) 32-39.

- [60] K.S. Kang, Y.S. Meng, J. Breger, C.P. Grey, G. Ceder, Electrodes with high power and high capacity for rechargeable lithium batteries, *Science*, 311 (2006) 977-980.
- [61] K. Amine, H. Tukamoto, H. Yasuda, Y. Fujita, Preparation and electrochemical investigation of $\text{LiMn}_{2-x}\text{Me}_x\text{O}_4$ (Me : Ni, Fe, and $x=0.5, 1$) cathode materials for secondary lithium batteries, *J Power Sources*, 68 (1997) 604-608.
- [62] Q.M. Zhong, A. Bonakdarpour, M.J. Zhang, Y. Gao, J.R. Dahn, Synthesis and electrochemistry of $\text{LiNi}_x\text{Mn}_{2-x}\text{O}_4$, *J Electrochem Soc*, 144 (1997) 205-213.
- [63] J.H. Kim, N.P.W. Pieczonka, L. Yang, Challenges and Approaches for High-Voltage Spinel Lithium-Ion Batteries, *Chemphyschem*, 15 (2014) 1940-1954.
- [64] A. Manthiram, K. Chemelewski, E.S. Lee, A perspective on the high-voltage $\text{LiMn}_{1.5}\text{Ni}_{0.5}\text{O}_4$ spinel cathode for lithium-ion batteries, *Energ Environ Sci*, 7 (2014) 1339-1350.
- [65] J.H. Kim, N.P.W. Pieczonka, Z.C. Li, Y. Wu, S. Harris, B.R. Powell, Understanding the capacity fading mechanism in $\text{LiNi}_{0.5}\text{Mn}_{1.5}\text{O}_4$ /graphite Li-ion batteries, *Electrochim Acta*, 90 (2013) 556-562.
- [66] N.P.W. Pieczonka, Z.Y. Liu, P. Lu, K.L. Olson, J. Moote, B.R. Powell, J.H. Kim, Understanding Transition-Metal Dissolution Behavior in $\text{LiNi}_{0.5}\text{Mn}_{1.5}\text{O}_4$ High-Voltage Spinel for Lithium Ion Batteries, *J Phys Chem C*, 117 (2013) 15947-15957.
- [67] A. Jarry, S. Gottis, Y.S. Yu, J. Roque-Rosell, C. Kim, J. Cabana, J. Kerr, R. Kostecki, The Formation Mechanism of Fluorescent Metal Complexes at the $\text{Li}_x\text{Ni}_{0.5}\text{Mn}_{1.5}\text{O}_4$ -delta/Carbonate Ester Electrolyte Interface, *J Am Chem Soc*, 137 (2015) 3533-3539.
- [68] J. Lu, C. Zhan, T.P. Wu, J.G. Wen, Y. Lei, A.J. Kropf, H.M. Wu, D.J. Miller, J.W. Elam, Y.K. Sun, X.P. Qiu, K. Amine, Effectively suppressing

dissolution of manganese from spinel lithium manganate via a nanoscale surface-doping approach, *Nat Commun*, 5 (2014) 6693.

[69] R.M. Qiao, L.A. Wray, J.H. Kim, N.P.W. Pieczonka, S.J. Harris, W.L. Yang, Direct Experimental Probe of the Ni(II)/Ni(III)/Ni(IV) Redox Evolution in $\text{LiNi}_{0.5}\text{Mn}_{1.5}\text{O}_4$ Electrodes, *J Phys Chem C*, 119 (2015) 27228-27233.

[70] J.S. Kim, K. Kim, W. Cho, W.H. Shin, R. Kanno, J.W. Choi, A Truncated Manganese Spinel Cathode for Excellent Power and Lifetime in Lithium-Ion Batteries, *Nano Lett*, 12 (2012) 6358-6365.

[71] R.D. Shannon, Revised Effective Ionic-Radii and Systematic Studies of Interatomic Distances in Halides and Chalcogenides, *Acta Crystallogr A*, 32 (1976) 751-767.

[72] J.H. Kim, A. Huq, M.F. Chi, N.P.W. Pieczonka, E. Lee, C.A. Bridges, M.M. Tessema, A. Manthiram, K.A. Persson, B.R. Powell, Integrated Nano-Domains of Disordered and Ordered Spinel Phases in $\text{LiNi}_{0.5}\text{Mn}_{1.5}\text{O}_4$ for Li-Ion Batteries, *Chemistry of Materials*, 26 (2014) 4377-4386.

[73] F.D. Murnaghan, The compressibility of media under extreme pressures, *P Natl Acad Sci USA*, 30 (1944) 244-247.

[74] F. Birch, Finite Elastic Strain of Cubic Crystals, *Phys Rev*, 71 (1947) 809-824.

[75] A. Yamada, H. Koizumi, S.I. Nishimura, N. Sonoyama, R. Kanno, M. Yonemura, T. Nakamura, Y. Kobayashi, Room-temperature miscibility gap in $\text{Li}(x)\text{FePO}_4$, *Nat Mater*, 5 (2006) 357-360.

[76] G. Kobayashi, S.I. Nishimura, M.S. Park, R. Kanno, M. Yashima, T. Ida, A. Yamada, Isolation of Solid Solution Phases in Size-Controlled Li_xFePO_4 at Room Temperature, *Adv Funct Mater*, 19 (2009) 395-403.

[77] W. Liu, P. Oh, X. Liu, M.J. Lee, W. Cho, S. Chae, Y. Kim, J. Cho, Nickel-Rich Layered Lithium Transition-Metal Oxide for High-Energy Lithium-Ion Batteries, *Angew Chem Int Edit*, 54 (2015) 4440-4457.

[78] Y.K. Sun, Z.H. Chen, H.J. Noh, D.J. Lee, H.G. Jung, Y. Ren, S. Wang,

- C.S. Yoon, S.T. Myung, K. Amine, Nanostructured high-energy cathode materials for advanced lithium batteries, *Nat Mater*, 11 (2012) 942-947.
- [79] Y.K. Sun, S.T. Myung, B.C. Park, J. Prakash, I. Belharouak, K. Amine, High-energy cathode material for long-life and safe lithium batteries, *Nat Mater*, 8 (2009) 320-324.
- [80] A. Manthiram, J.C. Knight, S.T. Myung, S.M. Oh, Y.K. Sun, Nickel-Rich and Lithium-Rich Layered Oxide Cathodes: Progress and Perspectives, *Adv Energy Mater*, 6 (2016).
- [81] D.J. Miller, C. Proff, J.G. Wen, D.P. Abraham, J. Baren, Observation of Microstructural Evolution in Li Battery Cathode Oxide Particles by In Situ Electron Microscopy, *Adv Energy Mater*, 3 (2013) 1098-1103.
- [82] S.J. Zheng, R. Huang, Y. Makimura, Y. Ukyo, C.A.J. Fisher, T. Hirayama, Y. Ikuhara, Microstructural Changes in $\text{LiNi}_{0.8}\text{Co}_{0.15}\text{Al}_{0.05}\text{O}_2$ Positive Electrode Material during the First Cycle, *J Electrochem Soc*, 158 (2011) A357-A362.
- [83] K. Meng, Z.X. Wang, H.J. Guo, X.H. Li, D. Wang, Improving the cycling performance of $\text{LiNi}_{0.8}\text{Co}_{0.1}\text{Mn}_{0.1}\text{O}_2$ by surface coating with Li_2TiO_3 , *Electrochim Acta*, 211 (2016) 822-831.
- [84] Z. Chen, J. Wang, D.L. Chao, T. Baikie, L.Y. Bai, S. Chen, Y.L. Zhao, T.C. Sum, J.Y. Lin, Z.X. Shen, Hierarchical Porous $\text{LiNi}_{1/3}\text{Co}_{1/3}\text{Mn}_{1/3}\text{O}_2$ Nano-/Micro Spherical Cathode Material: Minimized Cation Mixing and Improved Li^+ Mobility for Enhanced Electrochemical Performance, *Sci Rep-Uk*, 6 (2016) 25771.
- [85] A. Grimaud, W.T. Hong, Y. Shao-Horn, J.M. Tarascon, Anionic redox processes for electrochemical devices, *Nat Mater*, 15 (2016) 121-126.
- [86] M. Sathiya, G. Rouse, K. Ramesha, C.P. Laisa, H. Vezin, M.T. Sougrati, M.L. Doublet, D. Foix, D. Gonbeau, W. Walker, A.S. Prakash, M. Ben Hassine, L. Dupont, J.M. Tarascon, Reversible anionic redox chemistry in high-capacity layered-oxide electrodes, *Nat Mater*, 12 (2013) 827-835.

- [87] T. Ohzuku, A. Ueda, M. Nagayama, Electrochemistry and Structural Chemistry of LiNiO_2 ($R\bar{3}m$) for 4 Volt Secondary Lithium Cells, *J Electrochem Soc*, 140 (1993) 1862-1870.
- [88] S.K. Jung, H. Gwon, J. Hong, K.Y. Park, D.H. Seo, H. Kim, J. Hyun, W. Yang, K. Kang, Understanding the Degradation Mechanisms of $\text{LiNi}_{0.5}\text{Co}_{0.2}\text{Mn}_{0.3}\text{O}_2$ Cathode Material in Lithium Ion Batteries, *Adv Energy Mater*, 4 (2014).
- [89] J. Barker, R. Koksang, M.Y. Saidi, An electrochemical investigation into the lithium insertion properties of Li_xNiO_2 ($0 \leq x \leq 1$), *Solid State Ionics*, 89 (1996) 25-35.
- [90] R. Du, Y.J. Bi, W.C. Yang, Z. Peng, M. Liu, Y. Liu, B.M. Wu, B.C. Yang, F. Ding, D.Y. Wang, Improved cyclic stability of $\text{LiNi}_{0.8}\text{Co}_{0.1}\text{Mn}_{0.1}\text{O}_2$ via Ti substitution with a cut-off potential of 4.5 V, *Ceramics International*, 41 (2015) 7133-7139.

국문 초록 (Abstract in Korean)

전극 및 전자 재료의 크기가 나노화 되고, 기술의 고도화로 인해 복잡한 물리적·화학적인 현상들이 원자 단위부터 매크로 단위까지 복합적으로 일어나면서 멀티스케일 역학을 이용한 소재 해석 및 설계는 선택이 아닌 필수가 되어가고 있다. 특히 전기화학 반응을 동반하는 에너지 저장 장치의 경우, 나노 입자들로 이루어진 전극 소재와 폴리머, 금속 집전체들과 양극 및 음극을 이루고, 이 양극과 음극이 유기 액체 전해질과 소수성 멤브레인으로 연결되어있다. 이런 이유로 나노 입자의 물리적·화학적 변화가 이온 및 전자의 이동에 영향을 미치고, 이 영향이 전극의 특성에 영향을 미치고 곧 전체 전지의 성능에 영향을 미친다. 특히, 우리 삶에 가장 가까이에 있으면서 폭발에 매우 민감한 전기화학 전지를 해석 및 설계에 있어 멀티스케일 해석은 필수적이다.

특히 본 연구에서는 전극에 집중하여 연구를 수행하였는데 전극의 아주 작은 부분부터 전체 성능 및 안전성에 큰 영향을 미친다. 먼저, 전극 내 전하 운반체(i.e. Li^+ or Na^+)의 함량이 전극의 전체 용량을 나타내며, 이 전하 운반체의 이동 속도 및 전하의 이동 속도가 전지의 출력특성의 주된 결정인자가 된다. 또한 전하 운반체가 삽입 및 탈리되었을 때 전극의 구조적 상 안정성이 전지의 수명에 큰 영향을 미친다. 이와 마찬가지로 전하 운반체의 삽입·탈리 중의 표면 원자들의 분해 및 열화 또한 전지의 수명 및

안전성에 큰 영향을 미치게 된다. 마지막으로 전기화학 반응 중에 상의 변화로 인해 균열이 생겨나고, 전극이 부서지는 일들이 발생하는데, 이 또한 수명 및 안전성에 치명적인 영향을 미치게 된다. 이와 같이 이온, 전자, 원자 단위의 변화가 전극의 전기적, 화학적, 기계적 특성에 영향을 미치고, 이는 전체 전지의 성능, 수명을 결정하는 요인으로 작용함으로써 멀티스케일을 통한 역학적 분석 및 설계를 통한 전극의 개발이 꼭 필요한 실정이다.

이를 위해 본 연구에서는 제일원리계산을 통한 원자 단위 해석부터 통계열역학적 해석, 표면에서의 원자 분해 계산, 상 장 모델을 통한 입자 단위 상전이 해석, 유한요소해석을 통한 기계적 변형 해석, 그리고 상 장 파괴 모델을 통한 파괴 해석까지 총체적인 멀티스케일 역학 해석 기법을 정립하였다. 특히, 전지 전극의 경우 비교적 큰 크기의 전하 운반체가 삽입 및 탈리되면서, 상전이 및 구조적 변화가 극심한 재료로 기존 합금 해석과 관련하여 적용되는 단상 또는 이상 상전이 반응을 고려한 모델을 적용하기에는 무리가 있다. 대부분 단상 반응과 이상 반응이 복합적으로 일어나는 복합 상 반응이 일어나기 때문인데, 이런 이유로 본 연구에서는 제일원리계산을 통해 열역학적 인자를 도출할 때에 복합 상 반응을 고려할 수 있도록 함으로써 전체 시스템을 지배하는 전체 자유 에너지 함수 및 지배 방정식에서부터 복합 상 반응을 모사할 수 있는 방법론을 정립하였다. 그리고 이를 다양한 리튬이온전지의 고성능 양극 소재에 적용함으로써, 역학 기반 멀티스케일 전지 전극 설계 및 실험적 실현에 관하여 연구하였다.

고에너지 양극 소재인 과리튬 산화물 양극에 본 방법론을 적용함으로써 전반적인 상전이 메커니즘을 밝혀 수명 특성을

향상시킬 수 있는 단서를 마련하였다. 이 메커니즘을 역이용하여 과리튬 산화물 양극의 수명 특성을 향상시킬 수 있는 설계를 산소 결합 및 전이금속 도핑을 통해 달성하였으며, 실험을 통해 직접 구현함으로써 향상된 성능을 검증하였다. 또한, 출력특성 향상을 위해 구리 도핑을 수행하였는데, 이는 p 타입의 전도성을 부여하는 기능을 하는 것으로 전자구조 분석을 통해 증명 하였으며, 이 또한 직접 실험을 통해 향상된 전기 전도도 및 출력 밀도를 검증하였다. 고출력·고전압 소재로서 스피넬 소재에 대한 설계로는 벌크 및 표면 도핑을 통합 접근을 수행하였는데, 알루미늄 벌크 도핑을 통해 비활성 상전이를 억제하여 수명을 향상 시켰고, 타이타늄 벌크 도핑을 통해 탄성 완화 및 출력 특성 향상, 그리고 타이타늄 표면 도핑을 통해 전이금속의 표면 용출을 억제함으로써 수명을 향상시키는 설계를 제안하고, 이를 실험을 통해 검증하였다. 전기화학 특성을 고려한 상전이를 해석하기 위해서 올리빈 소재를 대상으로 전기화학이 연계된 상전이 특성을 분석하였고, 마지막으로 구조적 안정성 및 파괴 특성에 관한 연구를 이 부분이 취약하다고 알려져 있는 과니켈 층상계 소재에 적용하여 분석을 수행하였다. 전반적인 구조적 변화 및 파괴 메커니즘을 먼저 해석하였고, 이를 통해 타이타늄이라는 도핑 후보군을 도출하였다. 그리고 타이타늄을 도핑하였을 때, 괄목할 만큼 파괴가 줄어드는 것을 계산을 통해 예측할 수 있었고, 이는 보고된 실험과 일치하는 것을 발견하였다.

결론적으로 위와 같이 본 정립된 방법론을 다양한 특성을 가지는 양극 소재에 적용하여, 전극에 필수적인 성능을 향상시키는 연구를 계산을 통해 이론적으로 예측하고, 실험을 통해 실현 및 검증하는 연구를 성공적으로 수행하였다. 이는 본 멀티스케일 역학

방법론의 효용성을 증명하는 것뿐만 아니라, 기존에 경험적인 반복을 통해 전극 소재를 개발하던 종래의 방향과 더불어 신뢰할만한 이론적 예측을 통한 실현을 이용한 개발 방향에 대한 기초를 제공할 수 있을 것으로 기대한다. 또한 제안된 멀티스케일 방법론은 복합 상 반응을 고려할 수 있는 자유에너지 함수를 제일원리를 통해 계산하는 방법으로 다양한 소재에 광범위하게 적용할 수 있음은 물론이고, 본 자유에너지를 다양한 해석 기법(i.e. 상 장 모델, 전기화학, 미세역학, 연속체 역학 등)에 적용하여 지배 방정식을 자유롭게 유도해낼 수 있다. 다시 말해, 본 멀티스케일 역학 방법론은 기저에 있는 자유 에너지 정립에 그 핵심이 있고, 이를 통해 다양한 소재 및 여러 해석 기법에 적용하여 광범위한 해석 및 설계를 수행할 수 있다. 더 나아가, 전지를 벗어나 커패시터, 연료 전지, 태양 전지, 축매 등 다양한 에너지 관련 소재의 개발에 적용할 수 있을 것으로 기대한다.

Keywords: 멀티스케일 역학, 복합 상 반응, 제일원리계산, 상 장 모델, 유한요소해석, 상 장 파괴 모델

Student Number: 2011-22894